1949

Description of elementary particle collisions with high precision

Doctoral (PhD) dissertation

Zoltán Tulipánt

Supervisor:

Dr. Gábor Somogyi

UNIVERSITY OF DEBRECEN
Doctoral Council of Natural Sciences and Information Technology
Doctoral School of Physics

Debrecen, 2020

Ezen értekezést a Debreceni Egyetem Természettudományi és Informatikai Doktori Tanács Fizikai Tudományok Doktori Iskolájának Részecskefizika programja keretében készítettem a Debreceni Egyetem természettudományi doktori (PhD) fokozatának elnyerése céljából.
Nyilatkozom arról, hogy a tézisekben leírt eredmények nem képezik más PhD disszertáció részét.

Debrecen, 2020. június 22.

Tulipánt Zoltán
doktorjelölt

Tanúsítom, hogy Tulipánt Zoltán doktorjelölt 2016-2020 között a fent megnevezett Doktori Iskola Részecskefizika programjának keretében irányításommal végezte munkáját. Az értekezésben foglalt eredményekhez a jelölt önálló alkotó tevékenységével meghatározóan hozzájárult. Nyilatkozom továbbá arról, hogy a tézisekben leírt eredmények nem képezik más PhD disszertáció részét.
Az értekezés elfogadását javasolom.

Debrecen, 2020. június 22.

Dr. Somogyi Gábor
témavezető

Description of elementary particle collisions with high precision

Értekezés a doktori (Ph.D.) fokozat megszerzése érdekében
a fizika tudományágban

Írta: Tulipánt Zoltán
okleveles fizikus

Készült a Debreceni Egyetem Fizikai Tudományok Doktori Iskolája
Részecskefizika programja keretében

Témavezető: Dr. Somogyi Gábor

A doktori szigorlati bizottság:

elnök: Dr. Kun Ferenc ________________________

tagok: Dr. Horváth Dezső ________________________

Dr. Patkós András ________________________

A doktori szigorlat időpontja: 2018. június 27.

Az értekezés bírálói:

Dr. ________________________ ________________________

Dr. ________________________ ________________________

A bírálóbizottság:

elnök: Dr. ________________________ ________________________

tagok: Dr. ________________________ ________________________

Dr. ________________________ ________________________

Dr. ________________________ ________________________

Dr. ________________________ ________________________

Az értekezés védésének időpontja: ________________________

Acknowledgement

I would like to thank my supervisor, Dr. Gábor Somogyi for his invaluable guidance and support during my studies and in the preparation of my dissertation.

I am grateful to the leader of our research group, Prof. Dr. Zoltán Trócsányi who guided me through my years spent at the university.

I would like to thank my colleagues Giuseppe Bevilacqua, Ádám Kardos and Zoltán Szőr for their help and our fruitful discussions.

Finally, I would like to thank my family for their relentless support.

Contents

Part I

Preliminaries

Chapter 1

Introduction

The standard model of particle physics is the most well-tested and precise theory of the microscopic world constructed thus far. Although this model is believed to be theoretically self-consistent and has been able to predict experimental data with high accuracy, it still does not account for a number of phenomena that are believed to belong in the domain that such a theory should be able to describe. Hence, the construction of a complete theory of elementary particles and their fundamental interactions, of which currently only the electromagnetic, the weak and the strong interactions are incorporated in the standard model, is an ongoing effort. This endeavour benefits much from the search for deviations between the results of our current standard model and measurement data.

In order to acquire more information on what the boundaries of the validity of the standard model are, it is necessary to measure particle-level phenomena with high accuracy. The centerpiece of experimental particle physics is the Large Hadron Collider (LHC) which makes precise tests of current theories possible through the vast amounts of data collected from highly energetic proton-proton collisions. The analysis of these data requires similarly accurate theoretical predictions. Fig. 1.1 shows recent measurements at the LHC along with the corresponding theoretical predictions.

Since LHC processes are initiated by nucleons, the strong interaction plays a crucial role in every event. Furthermore, at energies relevant at the LHC the strength of the strong interaction is nearly ten times greater than the strength of the electromagnetic interaction. As a consequence, the final state of every collision is dominated by strongly interacting matter, making a highly precise description of the strong interaction necessary.

One of the possible methods for computing predictions from our theoretical model is perturbation theory. Since the non-interacting quantum field theory on which our model is based can be solved exactly we look for an approximate solution to the

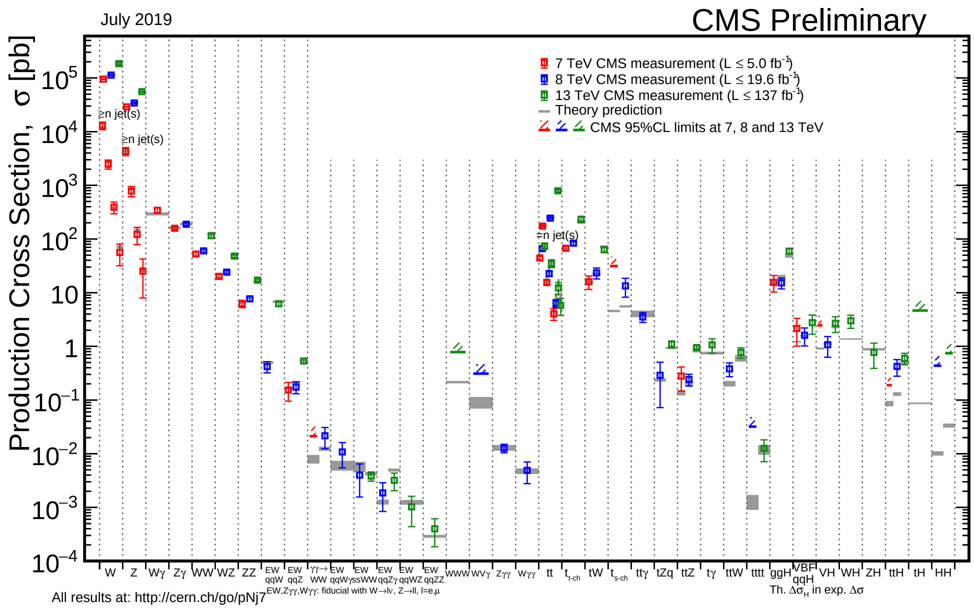

Figure 1.1: Cross sections of standard model processes measured by the CMS collaboration. Highly accurate measurements must be matched with similarly precise theoretical calculations. The figure was taken from the 2019 archived edition of the Review of Particle Physics. (`pdg.lbl.gov`) [1, 2]

interacting theory in the form of a series expansion in terms of some small parameter. Such a solution can be computed order by order and the more terms we obtain in the series expansion the more accurate the approximation will be. The small parameter in our case is a so-called coupling which determines the strength of the interaction. In the case of the strong interaction the first term in the perturbative series provides only a crude quantitative prediction and the computation of the first radiative correction is indispensable if any comparison to measurement data needs to take place. However, these days in many situations, achieving satisfactory precision requires the calculation of the second radiative correction.

In the first part of this dissertation I describe the theoretical background of my results, which is the quantum field theory of the strong interaction. There, I introduce the terminology and notation used in our field and also discuss the computation of cross sections in perturbation theory in detail. I finish by presenting our method for the computation of second radiative corrections for physical observables measured in electron-positron collisions.

In the second part I present my work done to measure the coupling of the strong interaction. I start by describing the calculation of an observable called energy-energy correlation incorporating second radiative corrections for the first time and assess the impact of those corrections on the extraction of the coupling from measurements based on this observable. Next, I discuss the determination of the value of the coupling based on a global analysis of experimental data and our theoretical calculations. Then I proceed by describing a similar procedure where we extracted the value of the coupling from measurements of so-called jet rates. I finish by presenting the values of the coupling obtained using the two procedures.

Finally, in the third part I describe recent developments of our perturbative framework. This scheme has already been worked out for collisions which do not contain strongly interacting particles in the initial state. I have worked on extending this framework to be applicable to LHC processes as well.

The fourth part contains the summary of the work presented in this dissertation.

Chapter 2

Quantum chromodynamics

2.1 $SU(3)_C$ symmetry and the QCD Lagrangian

Quantum chromodynamics (QCD) is the quantum field theory of the strong interaction [3–5] that acts between colored spin-1/2 fermions called quarks and it is mediated by spin-1 bosons called gluons that also possess color charge. These particles are collectively labelled as partons. QCD is characterized by a local $SU(3)_C$ symmetry where the index C stands for color charge. The generators of the symmetry group are denoted as t^a and they satisfy

$$[t^a, t^b] = \mathrm{i} f^{abc} t^c, \tag{2.1}$$

where f^{abc} are the structure constants and the Einstein summation convention is also used for repeated color indices. The quarks transform under the fundamental representation of the group in which the generators are the 3×3 matrices T^a, while the gluons transform under the adjoint representation. The quadratic Casimir invariants in the fundamental and the adjoint representation are given by

$$C_F = T_R \frac{N_C^2 - 1}{N_C} \qquad \text{and} \qquad C_A = 2 T_R N_C \tag{2.2}$$

respectively, where T_R is a normalization constant that we choose to be 1/2 and the number of colors N_C (which is set $N_C = 3$ when performing numerical computations) is kept explicit in every formula for the sake of clarity.

When constructing a field theory, we generally start by determining the action functional which for a field ϕ is the integral of the Lagrangian density $\mathcal{L}$:

$$\mathcal{S}[\phi] = \int \mathrm{d}^D x \; \mathcal{L}(\phi, \partial\phi, x), \tag{2.3}$$

where $D = 4$ is the number of spacetime dimensions. In order to constrain the form of the action, we impose certain symmetries upon it. For example, the action must be invariant under the Poincaré group thus it must be a Lorentz scalar. This condition, through Noether's theorem leads to the emergence of familiar conservation laws, like the conservation of momentum. This type of symmetry is labelled global since it implies an invariance under global transformations that are independent of spacetime coordinates. When considering interacting fields, the conservation of charge can be enforced in a similar manner. In the case of color charge the existence of global $SU(3)_C$ symmetry leads to color charge conservation. However, we also require the action to be invariant under local $SU(3)_C$ transformations, i.e. gauge invariant, which necessitates the introduction of so-called gauge fields and this leads to the emergence of the strong interaction.

The Lagrangian of interacting massive quarks is the $SU(3)_C$ invariant expression

$$\mathcal{L}_{quark} = \sum_{k=1}^{n_f} \bar{q}_{k,i}(\mathrm{i}\not{D}_{ij} - m_k \delta_{ij}) q_{k,j}, \tag{2.4}$$

which contains n_f quark flavors. The Dirac spinor $q_{k,i}$ stands for a quark field of flavor k and color i with mass m_k. The Einstein summation convention is used for both Lorentz and color indices, while summation over flavor is left explicit. In Eq. 2.4

$$D_{ij,\mu} = \delta_{ij}\partial_\mu + \mathrm{i} g_S A^a_\mu T^a_{ij} \tag{2.5}$$

is the $SU(3)_C$ covariant derivative which contains the strong coupling g_S and the $N_C^2 - 1$ vector fields A^a_μ for the gluons.

The complete QCD Lagrangian contains another gauge invariant term that accounts for the dynamics of the gauge fields. This term is

$$\mathcal{L}_{gluon} = -\frac{1}{4} F^a_{\mu\nu} F^{a,\mu\nu} \tag{2.6}$$

where

$$F^a_{\mu\nu} = \partial_\mu A^a_\nu - \partial_\nu A^a_\mu - g_S f^{abc} A^b_\mu A^c_\nu \tag{2.7}$$

is the field strength tensor. We can also include yet another gauge invariant but CP-violating term but since its coefficient is constrained by experiments to be smaller than 10^{-9} and it is outside the scope of my dissertation[1], this term is omitted.

In a classical theory we are looking for field configurations that produce a stationary action, meaning $\delta\mathcal{S} = 0$. This condition gives us the classical equations of motion

[1] This CP violating term is proportional to $\epsilon^{\alpha\beta\gamma\delta} F^a_{\alpha\beta} F^a_{\gamma\delta}$ (with $\epsilon^{\alpha\beta\gamma\delta}$ being the four-dimensional Levi-Civita symbol) which does not give contributions in perturbation theory. However, its presence affects the full non-perturbative QFT.

for the fields. In quantum field theory, however, we need to include such contributions that do not belong to a stationary action. Since we seek to describe the result of particle collisions, we compute cross sections that can ultimately be obtained from time-ordered correlation functions. Thus it is natural to construct our quantum field theory using the *path integral formalism.* In this framework, the correlation functions we seek to compute are obtained from the generating functional which is constructed using the action defined earlier.

2.2 The running coupling

The parameters that appear in the QCD Lagrangian are the bare quark masses and the so-called bare strong coupling g_S. The latter describes the strength of the interaction. First, these parameters appear as constants in the QCD Lagrangian, however, some modification is necessary as the one-particle irreducible (1PI) Green functions obtained using the original action are divergent. These singularities come from high energy contributions and hence they are called ultraviolet (UV) divergences. Since the 1PI Green functions are interpreted as physical quantites we need to introduce counterterms that cancel the singular contributions. One way of doing this is using *multiplicative renormalization* which means that we replace the unphysical bare fields and parameters of the original action with the physical renormalized quantities that are proportional to the bare ones. The proportionality factors can depend on renormalized parameters, like couplings and masses.

Before any calculation can take place, first we must regularize our theory to obtain mathematically sensible expressions. One way of doing so is called *dimensional regularization* which means we set the number of spacetime dimensions to $D = 4-2\epsilon$. This procedure does not violate the symmetries of the action but now the 1PI Green functions become functions of the regularization parameter ϵ and the UV singularities appear as poles at $\epsilon = 0$, i.e. $D = 4$. To keep the coupling a dimensionless parameter, we must also introduce the unphysical parameter μ_0 whith mass dimension and multiply g_S by μ_0^ϵ. In light of this change, multiplicative renormalization of the coupling must be carried out as

$$\mu_0^\epsilon g_S^{(B)} = \mu^\epsilon g_S^{(R)} Z_g, \tag{2.8}$$

where indices (B) and (R) refer to bare and renormalized parameters respectively. After renormalization an unphysical parameter μ still appears in the expressions but now it has a different meaning than the original μ_0. While μ_0 is a dimensional regularization scale introduced to keep the coupling dimensionless in D dimensions, μ is the renormalization scale which gives the energy scale of the coupling. Since μ_0 and μ are unphysical, physical quantities must be independent of them.

In our calculations we use massless QCD which means we neglect quark masses, thus the only parameter is the strong coupling. Performing multiplicative renormalization we find that the renormalized coupling becomes scale dependent and its behaviour is described by the *renormalization group equation (RGE)* which is built on the idea that the bare coupling does not depend on the renormalization scale. Hence the RGE derived from Eq. (2.8) takes the form

$$\mu^2 \frac{\mathrm{d}\alpha_S(\mu^2)}{\mathrm{d}\mu^2} = \beta(\alpha_S(\mu^2)). \tag{2.9}$$

From now on we drop the index (R) from renormalized quantities. Furthermore, instead of g_S that appears in the Lagrangian we use $\alpha_S = g_S^2/(4\pi)$ and refer to it as the strong coupling. We can solve the RGE perturbatively by computing the beta function as a series of the coupling,

$$\beta(\alpha_S(\mu^2)) = -\left(\frac{\alpha_S}{4\pi}\right)^2 \sum_{n=0}^{\infty} \left(\frac{\alpha_S}{4\pi}\right)^n \beta_n. \tag{2.10}$$

The β_n are the $n+1$-loop coefficients of the β function which are given up to three-loop order in the modified minimal subtraction scheme ($\overline{MS}$) as

$$\begin{aligned}
\beta_0 &= \frac{11C_A}{3} - \frac{4n_f T_R}{3}, \\
\beta_1 &= \frac{34}{3}C_A^2 - \frac{20}{3}C_A T_R n_f - 4C_F T_R n_f, \\
\beta_2 &= \frac{2857}{54}C_A^3 - \left(\frac{1415}{27}C_A^2 + \frac{205}{9}C_A C_F - 2C_F^2\right) T_R n_f + \left(\frac{158}{27}C_A + \frac{44}{9}C_F\right) T_R^2 n_f^2.
\end{aligned} \tag{2.11}$$

Using the three-loop running of the strong coupling we can determine the scale dependence iteratively and express $\alpha_S(\mu)$ in terms of the value of α_S at some fixed scale Q,

$$\begin{aligned}
\alpha_S(\mu) &= \alpha_{S1}(\mu) + \alpha_{S2}(\mu) + \alpha_{S3}(\mu), \\
\alpha_{S1}(\mu) &= \frac{\alpha_S(Q)}{(1+\alpha_S(Q)\beta_0 L)}, \\
\alpha_{S2}(\mu) &= -\alpha_{S1}(\mu)^2 \frac{\beta_1}{4\pi\beta_0} \ln(1+\alpha_S(Q)\beta_0 L), \\
\alpha_{S3}(\mu) &= \frac{\alpha_{S1}(\mu)^3}{16\pi^2} \Bigg\{ \frac{\beta_1^2}{\beta_0^2} \ln(1+\alpha_S(Q)\beta_0 L) \Bigg[\ln(1+\alpha_S(Q)\beta_0 L) - 1 \Bigg] \\
&\qquad + \left(\frac{\beta_1^2}{\beta_0^2} - \frac{\beta_2}{\beta_0}\right) \alpha_S(Q)\beta_0 L \Bigg\},
\end{aligned} \tag{2.12}$$

where $L = \ln(\mu/Q)$.

At this point it is apparent that the QCD coupling, i.e. the strength of the interaction decreases as the scale increases and it vanishes as μ tends to infinity[2]. This characteristic of QCD is known as asymptotic freedom and it validates the use of perturbation theory at high energies. Confinement is another property of the strong interaction which means that at low energies partons are not the appropriate degrees of freedom since they are confined into colorless states called hadrons. Although partons at low energies form bound states through a process called *hadronization*, they are still the relevant degrees of freedom in high energy collisions. This allows us to compute cross sections of high energy processes using partonic degrees of freedom even though the final states observed in experiments are made up of hadrons, albeit the partonic cross sections require non-perturbative corrections before any comparison to measurement data can take place.

The strong coupling can also be expressed by introducing the dimensionful constant Λ_{QCD},

$$\alpha_S(\mu) = \frac{4\pi}{\beta_0 t}\left[1 - \frac{\beta_1}{\beta_0^2 t}\ln t + \left(\frac{\beta_1}{\beta_0^2 t}\right)^2 \left(\ln^2 t - \ln t - 1 + \frac{\beta_0 \beta_2}{\beta_1^2}\right)\right], \tag{2.13}$$

where $t = \ln(\mu^2/\Lambda_{QCD}^2)$. The scale $\Lambda_{QCD} \approx 208\,\mathrm{MeV}$ where the running coupling diverges is called the Landau pole and it marks the point where the perturbative approach completely breaks down. As opposed to QED, in QCD the Landau pole can be found at relatively low energy since the value of the coupling decreases at higher energy scales. The strong coupling was measured at multiple energy scales and the experimental results are in good agreement with the theoretical prediction of the α_S running as shown in Fig. 2.1.

It is important to note that although the behavior of the strong coupling is determined through the RGE and the necessary coefficients can be computed from theory, the actual value of α_S is still not determined and must be set at one energy scale by measurement. As of 2019 the so-called world average of the strong coupling in the $\overline{MS}$ scheme at the scale of the Z boson mass ($M_Z = 91.2\,\mathrm{GeV}$) was determined to be $\alpha_S(M_Z) = 0.1179 \pm 0.0010$ [1, 2]. For a summary of results on the value of $\alpha_S(M_Z)$ obtained by multiple measurements see Fig. 2.2.

---

[2] This can be seen by substituting the actual number of colors ($N_C = 3$) and number of light quark flavors (in our case n_f=5) into β_0 which then becomes positive, making the leading contribution α_{S1} monotonically decreasing.

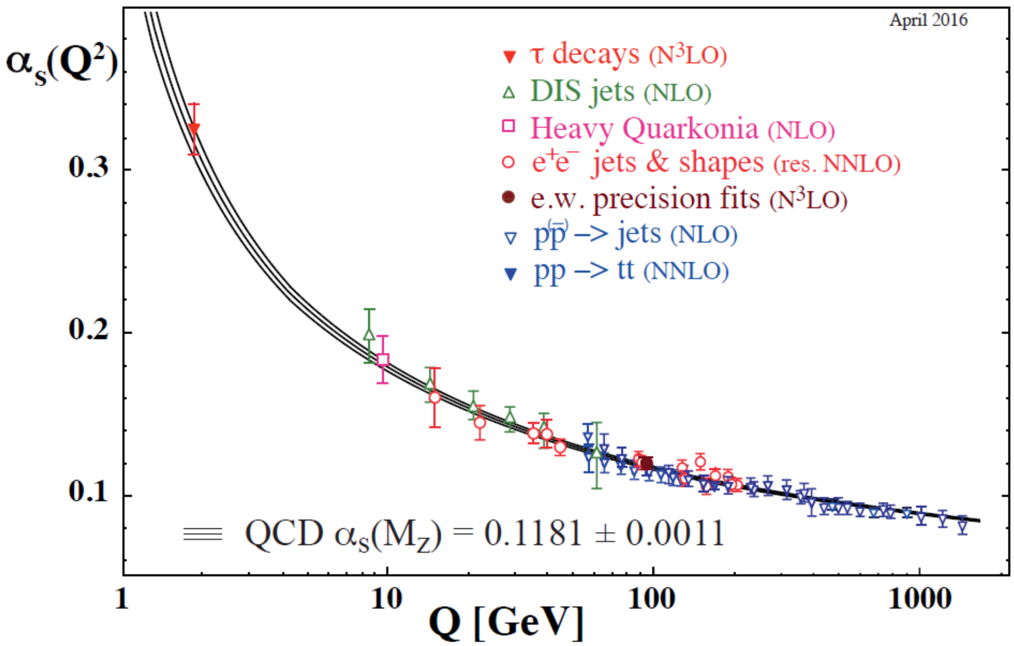

Figure 2.1: Measurements of α_S at different Q energy scales. The figure was taken from [6].

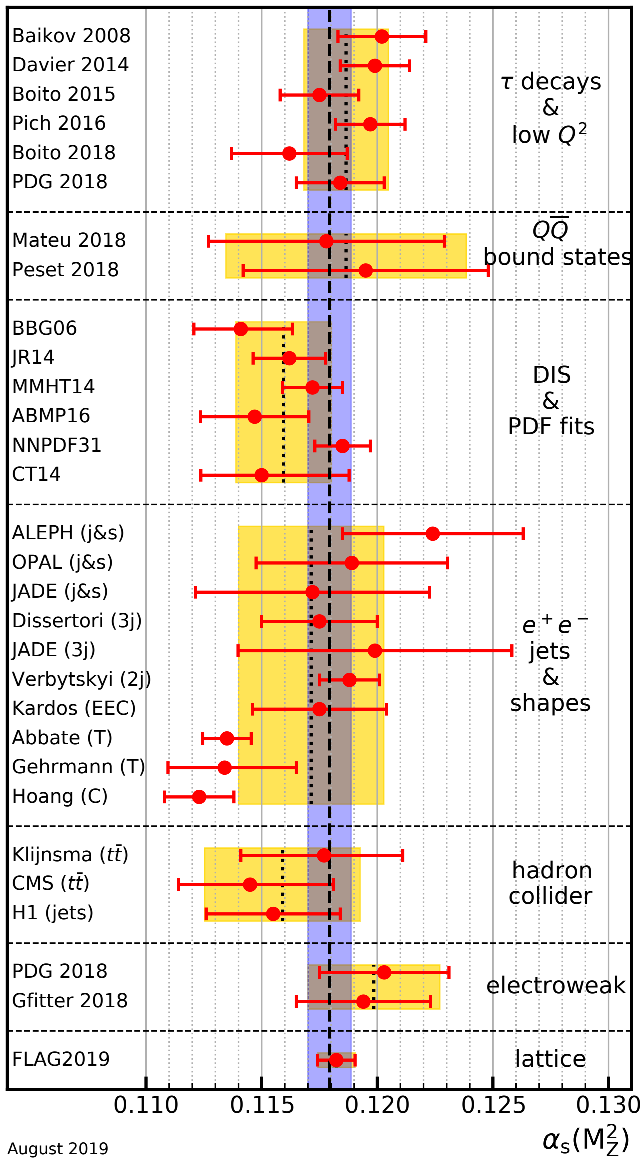

Figure 2.2: Measurements of the value of the strong couling at the scale of the Z boson mass. The blue band shows the world average. The figure was taken from the 2019 archived edition of the Review of Particle Physics. (`pdg.lbl.gov`) [1, 2]

Chapter 3

Cross sections

When computing physical quantities, we must face the problem that the degrees of freedom in QCD are partons, however, we can only detect the bound states of these particles. Thus the question naturally arises; can we use QCD to predict the outcome of high energy collisions in particle physics?

It is the so-called *parton-hadron duality* that bridges the gap between theoretical calculations and experimentally observable quantities. The idea behind this concept, which was first formulated by Poggio, Quinn and Weinberg [7], is that certain inclusive hadronic cross sections at high energies have to coincide (approximately) with the partonic cross sections.

The cross section σ of a proton-proton collision can be computed from the cross sections $\hat{\sigma}_{i,j}$ of parton collisions (often called as hard scattering cross sections) as [8]

$$\sigma(Q^2;\mu_R,\mu_F) = \sum_{i,j} \int \mathrm{d}x_1\, f_i(x_1;\mu_F) \int \mathrm{d}x_2\, f_j(x_2;\mu_F)\; \hat{\sigma}_{i,j}(x_1 x_2 Q^2;\mu_R,\mu_F) + \mathcal{O}(1/Q^p), \tag{3.1}$$

where $\mathcal{O}(1/Q^p)$ stands for final-state non-perturbative corrections that become small at high energies, since $p > 0$. The process-independent $f_i(x,\mu_F)$ functions are called parton density functions (*pdf*s for short) and they provide the probability $f_i(x)\,\mathrm{d}x$ that parton i carries a fraction of the proton momentum that is between x and $x + \mathrm{d}x$. Q stands for the center-of-mass momentum of the protons and μ_F is (like the renormalization scale) an unphysical parameter called *factorization scale*. The fact stated in Eq. 3.1 is referred to as the *factorization theorem* and it means that the long- and short-distance physics, that are represented by the pdfs and the hard scattering cross seciton respectively, are factorized and individual contributions of the partonic processes in hadron collisions must be summed incoherently.

The parton-hadron duality and the factorization theorem together validate the use of partonic cross sections. However, for a complete description of particle collisions with hadronic final states we need to consider non-perturbative corrections that take into account the effects of parton to hadron transition.

3.1 Definition

Let us turn from hadronic collisions to electron-positron annihilation. In this case, the computation of cross sections is simplified, since the initial state of the process of interest does not contain partons.

The total cross section for electron-positron annihilation is obtained from the n-particle quantum mechanical transition probability, also known as the n-particle squared matrix element, $|\mathcal{M}_n|^2$ as

$$\sigma = \frac{1}{2Q^2} \sum_n \int d\Phi_n(\{p\}_n; Q) \frac{1}{S} \sum_{spin} |\mathcal{M}_n|^2, \tag{3.2}$$

where averaging is carried out over the spin of the initial state particles for unpolarized beams and the result is also summed over the final state configurations. Division by the symmetry factor S is needed to handle identical particles. The integration is performed using the Lorentz-invariant phase space measure for n particles

$$d\Phi_n(\{p\}_n; Q) = \prod_{k=1}^{n} \frac{\mathrm{d}^D p_k}{(2\pi)^{D-1}} \, \delta_+(p_k^2 - m_k^2) \, (2\pi)^D \, \delta^{(D)}\Big(\sum_{k=1}^{n} p_k - Q\Big), \tag{3.3}$$

with Q being the total incoming momentum, p_k and m_k are the momentum and mass of the kth particle respectively and D is the number of spacetime dimensions. ($\{p\}_n$ denotes the set of n final-state momenta.) The index of the Dirac-delta-plus function simply stands for an additional Heaviside step function,

$$\delta_+(p^2 - m^2) = \delta(p^2 - m^2)\, \Theta(E - m) \tag{3.4}$$

which provides the constraint that each particle in the final state must have an energy greater than its mass. Finally, $1/(2Q^2)$ is the flux factor for massless initial-state particles.

The hadrons observed in the final state form structures, streams of collimated particles that we call jets. We use so-called observables to describe these structures. The cross section for an observable J is defined as

$$\sigma[J] = \frac{1}{2Q^2} \sum_n \int d\Phi_n(\{p\}_n; Q) \frac{1}{S} \sum_{spin} |\mathcal{M}_n|^2 J_n, \tag{3.5}$$

where J_n is the value of J on an n-particle phase space. The observables typically considered are either event shapes which assign numbers (or functions) to final-state configurations, or jet functions which select final states where particles form a certain number of jets. One example of an event shape is thrust which is defined as

$$T = \max_{\vec{n}} \left(\frac{\sum_i |\vec{n} \cdot \vec{p}_i|}{\sum_j |\vec{p}_j|} \right), \tag{3.6}$$

where $\vec{p}_i$ are the three-momenta of partons and $\vec{n}$ defines the direction of the thrust axis, $\vec{n}_T$, by maximizing the sum. In general, $1/2 \leq T \leq 1$, with $T = 1/2$ for spherically symmetric events and $T \to 1$ in the case of two back-to-back jets.

Another example is the C-parameter,

$$C_{\text{par}} = 3(\lambda_1\lambda_2 + \lambda_2\lambda_3 + \lambda_3\lambda_1), \tag{3.7}$$

where λ_1, λ_2 and λ_3 are the eigenvalues of the momentum tensor

$$\Theta^{\alpha\beta} = \frac{1}{\sum_j |\vec{p}_j|} \sum_i \frac{p_i^\alpha p_i^\beta}{|\vec{p}_i|}, \qquad \alpha, \beta = 1, 2, 3. \tag{3.8}$$

Since Θ is a symmetric non-negative tensor with unit trace, its eigenvalues are real and non-negative with $\sum_i \lambda_i = 1$. Therefore $0 \leq \lambda_i \leq 1$. In the dijet limit, the C-parameter vanishes and for spherical events $C_{\text{par}} = 1$, so $0 \leq C_{\text{par}} \leq 1$.

3.2 Perturbative expansion in α_S

When computing the cross section of n-jet production in high energy collisions we can take a perturbative approach and perform a series expansion in the strong coupling. This is justified by the asymptotic freedom of QCD which means that α_S tends to zero as the energy scale of the collision increases. Hence at sufficiently high energies $\alpha_S \ll 1$.

The first term in this so-called *fixed-order* perturbative expansion, which is lowest order in the coupling, is referred to as the *Leading Order* (LO) contribution. The second term is the *Next-to-Leading Order* (NLO) and the third is the *Next-to-Next -to-Leading Order* (NNLO) correction,

$$\sigma[J] = \sigma^{LO}[J] + \sigma^{NLO}[J] + \sigma^{NNLO}[J] + \ldots. \tag{3.9}$$

Since the cross section is just the integral of the n-particle squared matrix element $|\mathcal{M}_n|^2$ over the phase space of final-state particles (see Eq. (3.2)), the fixed-order expansion can be carried out on the level of the integrand.

The loop expansion of the bare n-particle amplitude[1] in terms of the bare coupling $\alpha_S^{(B)}$ is

$$|\mathcal{A}_n\rangle = \left(4\pi\alpha_S^{(B)}\right)^{\frac{q}{2}} \left[|\mathcal{A}_n^{(0)}\rangle + \left(\frac{\alpha_S^{(B)}\mu_0^{2\epsilon}}{4\pi}\right) |\mathcal{A}_n^{(1)}\rangle + \left(\frac{\alpha_S^{(B)}\mu_0^{2\epsilon}}{4\pi}\right)^2 |\mathcal{A}_n^{(2)}\rangle + \mathcal{O}(\alpha_S^3) \right], \tag{3.10}$$

where q is some non-negative integer that gives the power of g_S in the first non-vanishing term. The superscript of $\mathcal{A}_n$ stands for the loop order of the amplitude. The first term in the expansion is the tree-level[2] contribution, the second is the one-loop correction, the third is the two-loop correction and so on and so forth.

Since quantities obtained from the bare Lagrangian contain UV singularities we need to perform renormalization. Considering that we neglect quark masses, this procedure amounts to replacing the bare coupling with the renormalized one according to Eq. (2.8). Furthermore, if we seek to compute cross sections up to NNLO accuracy in perturbative QCD (pQCD) it is sufficient to use the three-loop running of α_S and make the substitution in the expression for the amplitudes according to the following formula (see e.g. [9]),

$$\alpha_S^{(B)}\mu_0^{2\epsilon}S_\epsilon^{\overline{MS}} = \alpha_S(\mu)\mu^{2\epsilon}\left[1 - \frac{\alpha_S(\mu)}{4\pi}\frac{\beta_0}{\epsilon} + \left(\frac{\alpha_S(\mu)}{4\pi}\right)^2\left(\frac{\beta_0^2}{\epsilon^2} - \frac{\beta_1}{2\epsilon}\right) + \mathcal{O}(\alpha_S^3)\right], \tag{3.11}$$

which can be obtained using Eqs. (2.8) and (2.9). $S_\epsilon^{\overline{MS}}$ is a scheme-dependent factor and it does not affect physical results. It is defined in the $\overline{MS}$ scheme as

$$S_\epsilon^{\overline{MS}} = (4\pi)^\epsilon e^{-\epsilon\gamma_E}, \tag{3.12}$$

where γ_E is the Euler-Mascheroni constant. This scheme-dependent factor is often denoted simply as S_ϵ in the literature but that notation here is reserved for

$$S_\epsilon = \frac{(4\pi)^\epsilon}{\Gamma(1-\epsilon)} \tag{3.13}$$

which comes from the integration of the angular part of the dimensionally regularized phase space.[3]

The renormalized amplitude can be derived by substituting Eq. (3.11) into Eq. (3.10). We write the loop expansion of the renormalized amplitude as

$$|\mathcal{M}_n\rangle = |\mathcal{M}_n^{(0)}\rangle + |\mathcal{M}_n^{(1)}\rangle + |\mathcal{M}_n^{(2)}\rangle + \ldots, \tag{3.14}$$

[1] In our case the loop expansion of an n-particle amplitude is equivalent with its perturbative expansion in the coupling.

[2] There are loop-initiated processes, like the production of a Higgs-boson in gluon fusion, which we do not discuss here.

[3] $\Gamma(x)$ will represent the Gamma function throughout the dissertation, unless otherwise noted.

with

$$
\begin{aligned}
|\mathcal{M}_n^{(0)}\rangle =& C(\mu)|\mathcal{A}_n^{(0)}\rangle, \\
|\mathcal{M}_n^{(1)}\rangle =& C(\mu)\left[\frac{\alpha_S}{4\pi}\left(\frac{\mu^2}{\mu_0^2}\right)^{\epsilon} S_\epsilon^{-1}\right]\left[|\mathcal{A}_n^{(1)}\rangle - \frac{q}{2}\frac{\beta_0}{\epsilon}\left(\frac{\mu^2}{\mu_0^2}\right)^{-\epsilon} S_\epsilon|\mathcal{A}_n^{(0)}\rangle\right], \\
|\mathcal{M}_n^{(2)}\rangle =& C(\mu)\left[\frac{\alpha_S}{4\pi}\left(\frac{\mu^2}{\mu_0^2}\right)^{\epsilon} S_\epsilon^{-1}\right]^2\left[|\mathcal{A}_n^{(2)}\rangle - \frac{q+2}{2}\frac{\beta_0}{\epsilon}\left(\frac{\mu^2}{\mu_0^2}\right)^{-\epsilon} S_\epsilon|\mathcal{A}_n^{(1)}\rangle\right. \\
&\left. + \left(\frac{q(q+2)}{8}\frac{\beta_0^2}{\epsilon^2} - \frac{q}{2}\frac{\beta_1}{2\epsilon}\right)\left(\frac{\mu^2}{\mu_0^2}\right)^{-2\epsilon} S_\epsilon^2|\mathcal{A}_n^{(0)}\rangle\right].
\end{aligned}
\tag{3.15}
$$

The common factor is simply

$$C(\mu) = \left[4\pi\alpha_S\frac{\mu^{2\epsilon}}{\mu_0^{2\epsilon}}S_\epsilon^{-1}\right]^{\frac{q}{2}}. \tag{3.16}$$

Now we can compute the n-particle squared matrix element up to NNLO and we obtain

$$|\mathcal{M}_n|^2 = |\mathcal{M}_n^{(0)}|^2 + 2\mathrm{Re}\langle\mathcal{M}_n^{(0)}|\mathcal{M}_n^{(1)}\rangle + 2\mathrm{Re}\langle\mathcal{M}_n^{(0)}|\mathcal{M}_n^{(2)}\rangle + |\mathcal{M}_n^{(1)}|^2 + \ldots. \tag{3.17}$$

The first term is just the tree-level contribution that appears in what we call the Born cross section,

$$\mathrm{d}\sigma_n^B = \frac{1}{2Q^2}\mathrm{d}\Phi_n|\mathcal{M}_n^{(0)}|^2 \tag{3.18}$$

which is understood as the fully differential LO cross section. For the sake of simplicity, averaging over spin states from now on is kept implicit. The second term contributes to the NLO correction and it is referred to as the virtual term,

$$\mathrm{d}\sigma_n^V = \frac{1}{2Q^2}\mathrm{d}\Phi_n 2\mathrm{Re}\langle\mathcal{M}_n^{(0)}|\mathcal{M}_n^{(1)}\rangle. \tag{3.19}$$

Finally, the remaining parts of Eq. (3.17) comprise the double virtual contribution,

$$\mathrm{d}\sigma_n^{VV} = \frac{1}{2Q^2}\mathrm{d}\Phi_n\left[2\mathrm{Re}\langle\mathcal{M}_n^{(0)}|\mathcal{M}_n^{(2)}\rangle + |\mathcal{M}_n^{(1)}|^2\right]. \tag{3.20}$$

When attempting to compute loop corrections to any process a major difficulty arises. Namely, the loop integrals diverge even after renormalization. Since we have already removed UV singularities at this point, such ill behavior originates from the infrared (IR) regime. To tackle this problem first we need to realize that loop corrections are not the only higher-order contributions we can consider. Remembering that in electrodynamics an accelerated charge gives off electromagnetic radiation we can argue that a similar effect arises in QCD as well. Following such reasoning it seems apparent that we must also include such corrections that contain more than n particles in the final state but are the same order in α_S as the loop corrections discussed before.

Computing the tree-level squared matrix element of an $n+1$-particle process we find that when a particle in the final state becomes soft (that is, its energy goes to zero) or its momentum becomes collinear with that of another particle, the phase space integral of the squared matrix element diverges in such way that it cancels the singularities of the one-loop correction at the level of the cross section. Indeed, the *Kinoshita-Lee-Nauenberg theorem* [10, 11] ensures us that the IR singularities of the loop integrals are cancelled by the divergences of phase space integrals order by order in the α_S expansion for observables that are inclusive enough (IR-safe).

Hence, the complete NLO correction should be understood as

$$\sigma^{NLO}[J] = \int_{n+1} \mathrm{d}\sigma^R_{n+1} J_{n+1} + \int_n \mathrm{d}\sigma^V_n J_n, \tag{3.21}$$

which is finite for IR-safe observables. The first term on the right-hand side is called the real contribution and it is obtained from the tree-level $n+1$-particle squared matrix element,

$$\mathrm{d}\sigma^R_{n+1} = \frac{1}{2Q^2} \mathrm{d}\Phi_{n+1} |\mathcal{M}^{(0)}_{n+1}|^2. \tag{3.22}$$

Following the same reasoning, the complete NNLO correction is

$$\sigma^{NNLO}[J] = \int_{n+2} \mathrm{d}\sigma^{RR}_{n+2} J_{n+2} + \int_{n+1} \mathrm{d}\sigma^{RV}_{n+1} J_{n+1} + \int_n \mathrm{d}\sigma^{VV}_n J_n, \tag{3.23}$$

with the first two terms, called the double real and real-virtual, defined similarly to Eqs. (3.22) and (3.19) but with one more particle in the final state. The double real term accounts for the correction containing two more final-state particles than the Born process,

$$\mathrm{d}\sigma^{RR}_{n+2} = \frac{1}{2Q^2} \mathrm{d}\Phi_{n+2} |\mathcal{M}^{(0)}_{n+2}|^2, \tag{3.24}$$

while the real-virtual contribution is a mixed term containing the one-loop correction to the process with an additional final-state particle,

$$\mathrm{d}\sigma^{RV}_{n+1} = \frac{1}{2Q^2} \mathrm{d}\Phi_{n+1}\ 2\mathrm{Re}\langle \mathcal{M}^{(0)}_{n+1} | \mathcal{M}^{(1)}_{n+1} \rangle. \tag{3.25}$$

As it was stated before, the finiteness of the cross section requires IR-safe observables, i.e. observables which are not sensitive to the emission of additional soft or collinear particles which at NLO means that

$$\begin{aligned} J_n(\{p\}_n) &\to 0 \qquad \text{if} \quad p_i \cdot p_j \to 0 \\ J_{n+1}(\{p\}_{n+1}) &\to 0 \qquad \text{if} \quad p_i \cdot p_j \to 0,\ p_k \cdot p_l \to 0,\ i \neq k. \end{aligned} \tag{3.26}$$

Furthermore

$$\begin{aligned} J_{n+1}(\{p\}_{n+1}) &\to J_n(\{p\}_n) \qquad \text{if} \quad p_i^\mu = \lambda q^\mu \text{ with } \lambda \to 0, \\ J_{n+1}(\{p\}_{n+1}) &\to J_n(\{p\}_n) \qquad \text{if} \quad p_i^\mu \to z p^\mu,\ p_j^\mu \to (1-z) p^\mu, \end{aligned} \tag{3.27}$$

with the vectors q and p fixed. These conditions can be generalized to higher orders but they are not spellt out here since the NLO case illustrates the essence of IR-safe observables perfectly: the observable is insensitive to soft and collinear radiation and vanishes when there are less than n well-separated hard particles present.

3.3 Treating infrared singularities

When computing cross sections to a certain fixed α_S order (hence the name, fixed-order perturbation theory) the singular behavior of the constituents still poses great difficulty, even though the poles are present only in intermediate steps of a physically consistent calculation and cancel each-other in the end. One way of surpassing such difficulty is reorganizing the constituents into well-behaved finite terms and there are a several methods available to do the job. We utilize our own so-called subtraction scheme which bears the name CoLoRFulNNLO (Completely local subtraction for fully differential predictions at NNLO).

Before any subtraction can take place we need to make the singular behavior explicit which, as for UV divergences, we achieve by dimensional regularization which means that we define our integrals in $D = 4-2\epsilon$ dimensions instead of 4. This method has the benefit of leaving Lorentz invariance and gauge invariance intact and the IR singularities of the cross section now emerge as poles in the Laurent-expansion with respect to ϵ.

The CoLoRFulNNLO method [12–14] has been completed for processes that contain partons only in the final state and its capabilities were shown in the computation of the decay of Higgs boson into a pair of b-quarks [15], and three-jet production in electron-positron annihilation [14, 16].

The components of the NLO correction in Eq. (3.21) can be made finite by subtracting a suitably defined approximate cross section from the real contribution and adding its integral over the unresolved particle to the virtual term,

$$\sigma^{NLO}[J] = \int_{n+1} \left[\mathrm{d}\sigma^{R}_{n+1} J_{n+1} - \mathrm{d}\sigma^{R,A_1}_{n+1} J_n \right]_{D=4} + \int_n \left[\mathrm{d}\sigma^{V}_{n} + \int_1 \mathrm{d}\sigma^{R,A_1}_{n+1} \right]_{D=4} J_n . \tag{3.28}$$

There are several prescriptions for constructing the approximate cross section [17–19]. In the CoLoRFulNNLO scheme it is written as

$$\mathrm{d}\sigma^{R,A_1}_{n+1} = \frac{1}{2Q^2} \mathrm{d}\Phi_{n+1}\, \mathcal{A}_1 |\mathcal{M}^{(0)}_{n+1}|^2, \tag{3.29}$$

where the approximate matrix element is given by

$$\mathcal{A}_1|\mathcal{M}_{n+1}^{(0)}|^2 = \sum_{r=1}^{n+1}\left[\mathcal{S}_r^{(0,0)} + \sum_{\substack{s=1\\ s\neq r}}^{n+1}\left(\frac{1}{2}\mathcal{C}_{rs}^{(0,0)} - \mathcal{C}_{rs}\mathcal{S}_r^{(0,0)}\right)\right]. \tag{3.30}$$

The terms $\mathcal{C}_{rs}^{(0,0)}$ and $\mathcal{S}_r^{(0,0)}$ denote subtractions that regularize the $\vec{p}_r||\vec{p}_s$ collinear and the $p_r \to 0$ soft singularities respectively. The $\mathcal{C}_{rs}\mathcal{S}_r^{(0,0)}$ soft-collinear counterterm makes sure that no double subtracting takes place in the overlapping soft-collinear phase space region. The superscript (l_1, l_2) means that the corresponding counterterm involves the product of an l_1-loop subtraction kernel and an l_2-loop squared matrix element.

The approximate squared matrix element takes into account all spin and color correlations in the infrared limits, making the subtraction completely local. This feature is a necessary condition for the regularized real contribution,

$$\int_{n+1}\left[\mathrm{d}\sigma_{n+1}^{R} J_{n+1} - \mathrm{d}\sigma_{n+1}^{R,A_1} J_n\right], \tag{3.31}$$

to be mathematically well-defined in four dimensions.

Similarly to the NLO subtraction method explained before, the CoLoRFulNNLO scheme utilizes completely local counterterms in order to obtain mathematically well-defined regularized contributions. In this scheme we render the terms of Eq. (3.23) finite by the following rearrangement,

$$\sigma^{NNLO}[J] = \int_{n+2}\mathrm{d}\sigma_{n+2}^{NNLO} + \int_{n+1}\mathrm{d}\sigma_{n+1}^{NNLO} + \int_{n}\mathrm{d}\sigma_{n}^{NNLO}, \tag{3.32}$$

where

$$\mathrm{d}\sigma_{n+2}^{NNLO} = \left\{\mathrm{d}\sigma_{n+2}^{RR} J_{n+2} - \mathrm{d}\sigma_{n+2}^{RR,A_2} J_n - \left[\mathrm{d}\sigma_{n+2}^{RR,A_1} J_{n+1} - \mathrm{d}\sigma_{n+2}^{RR,A_{12}} J_n\right]\right\}_{D=4}, \tag{3.33}$$

$$\mathrm{d}\sigma_{n+1}^{NNLO} = \left\{\left(\mathrm{d}\sigma_{n+1}^{RV} + \int_1 \mathrm{d}\sigma_{n+2}^{RR,A_1}\right) J_{n+1} - \left[\mathrm{d}\sigma_{n+1}^{RV,A_1} + \left(\int_1 \mathrm{d}\sigma_{n+2}^{RR,A_1}\right)^{A_1}\right] J_n\right\}_{D=4}, \tag{3.34}$$

$$\mathrm{d}\sigma_{n}^{NNLO} = \left\{\mathrm{d}\sigma_{n}^{VV} + \int_2\left[\mathrm{d}\sigma_{n+2}^{RR,A_2} - \mathrm{d}\sigma_{n+2}^{RR,A_{12}}\right] + \int_1\left[\mathrm{d}\sigma_{n+1}^{RV,A_1} + \left(\mathrm{d}\sigma_{n+2}^{RR,A_1}\right)^{A_1}\right]\right\}_{D=4} J_n. \tag{3.35}$$

Eq. (3.33) contains the double real correction which diverges whenever one or two partons become unresolved. To regularize the two-parton unresolved singularities we subtract

$$\mathrm{d}\sigma_{n+2}^{RR,A_2} = \frac{1}{2Q^2}\mathrm{d}\Phi_{n+2}\mathcal{A}_2|\mathcal{M}_{n+2}^{(0)}|^2, \tag{3.36}$$

where the approximate squared matrix element for processes with $m+2$ partons in the final state is

$$\mathcal{A}_2|\mathcal{M}_{n+2}^{(0)}|^2 = \sum_{\substack{r,s\\ r\neq s}} \Bigg\{ \frac{1}{2}\mathcal{S}_{rs}^{(0,0)} + \sum_{i\neq r,s} \Bigg[\frac{1}{6}\mathcal{C}_{irs}^{(0,0)} + \frac{1}{2}\Bigg(\mathcal{CS}_{ir;s}^{(0,0)} - \mathcal{C}_{irs}\mathcal{CS}_{ir;s}^{(0,0)} \Bigg) + \sum_{j\neq i,r,s} \Bigg(\frac{1}{8}\mathcal{C}_{ir;js}^{(0,0)} - \frac{1}{2}\sum_{j\neq i,r,s} \mathcal{C}_{ir;js}\mathcal{CS}_{ir,s}^{(0,0)} + \frac{1}{2}\mathcal{C}_{ir;js}\mathcal{S}_{rs}^{(0,0)} \Bigg) - \mathcal{CS}_{ir;s}\mathcal{S}_{rs}^{(0,0)} + \mathcal{C}_{irs}\mathcal{S}_{rs}^{(0,0)} + \mathcal{C}_{irs}\mathcal{CS}_{ir;s}\mathcal{S}_{rs}^{(0,0)} \Bigg]\Bigg\} \tag{3.37}$$

The functions $\mathcal{C}_{irs}^{(0,0)}$, $\mathcal{C}_{ir;js}^{(0,0)}$, $\mathcal{CS}_{ir;s}^{(0,0)}$ and $\mathcal{S}_{rs}^{(0,0)}$ regularize the squared matrix element in the $\vec{p}_i||\vec{p}_r||\vec{p}_s$ triple-collinear, the $\vec{p}_i||\vec{p}_r$, $\vec{p}_j||\vec{p}_s$ double-collinear, the $\vec{p}_i||\vec{p}_r$ and $p_s \to 0$ collinear-soft and the $p_r, p_s \to 0$ double soft limits. The rest of the counterterms account for the overlaps between limits.

After subtracting the double unresolved approximate cross section, the remainder is still divergent in the single unresolved regions of phase space, thus we also need to subtract

$$\mathrm{d}\sigma_{n+2}^{RR,A_1} = \frac{1}{2Q^2}\mathrm{d}\Phi_{n+2}\,\mathcal{A}_1|\mathcal{M}_{n+2}^{(0)}|^2, \tag{3.38}$$

where $\mathcal{A}_1$ has been defined in Eq. (3.30). In order to avoid the double subtraction in the overlapping single and double unresolved regions of phase space, we must add the single unresolved limit of the term regularizing the double unresolved singularities

$$\mathrm{d}\sigma_{n+2}^{RR,A_{12}} = \frac{1}{2Q^2}\mathrm{d}\Phi_{n+2}\,\mathcal{A}_{12}|\mathcal{M}_{n+2}^{(0)}|^2, \tag{3.39}$$

which contains the iterated single unresolved approximate squared matrix element with the $\mathcal{A}_{12}$ operator defined as

$$\mathcal{A}_{12}|\mathcal{M}_{n+2}^{(0)}|^2 = \sum_{t=1}^{n+2}\Bigg[\mathcal{S}_t\mathcal{A}_2|\mathcal{M}_{n+2}^{(0)}|^2 + \sum_{\substack{k=1\\ k\neq t}}^{n+2}\Bigg(\frac{1}{2}\mathcal{C}_{kt}\mathcal{A}_2|\mathcal{M}_{n+2}^{(0)}|^2 - \mathcal{C}_{kt}\mathcal{S}_t\mathcal{A}_2|\mathcal{M}_{n+2}^{(0)}|^2 \Bigg)\Bigg]. \tag{3.40}$$

In Eq. (3.34) we have the sum of the real-virtual correction and the integrated single unresolved subtraction from the double real correction,

$$\mathrm{d}\sigma_{n+1}^{RV} + \int_1 \mathrm{d}\sigma_{n+2}^{RR,A_1}, \tag{3.41}$$

which is finite in ϵ, since the poles of the one-loop matrix element are cancelled by the integrated counterterm, however, it still contains kinematic singularities in the single unresolved part of the $n+1$-parton phase space. These singularities are regularized by two suitably defined approximate cross sections, $\mathrm{d}\sigma_{n+1}^{RV,A_1}$ and $\left(\mathrm{d}\sigma_{n+2}^{RR,A_1}\right)^{A_1}$.

Finally, the two-loop correction appears in Eq. (3.35) and its explicit infrared singularities are cancelled by the four remaining integrated counterterms. In the work that was published in Ref. [14] I implemented the two-loop contribution of three-jet production based on Refs. [20, 21]. Furthermore, I also partook in the integration of the subtraction terms from the double real contribution. These integrals were obtained as a Laurent expansion in ϵ. The coefficients of the poles were ultimately obtained analytically and the finite part was computed numerically.

The CoLoRFulNNLO subtraction scheme was implemented for three-jet production in electron-positron annihilation [14]. The performance of the subtraction scheme is shown by comparing theoretical predictions computed through the use of CoLoRFulNNLO and other methods denoted by SW [22] and GGGH [23] to measurement data. Results obtained at LO, NLO and NNLO accuracy on $\tau \equiv 1-T$ thrust and C_{par} are shown in Figs. 3.1 and 3.2. The effect of neglecting higher-order terms was estimated by varying the renormalization scale in the range $\mu_R \in [Q/2, 2Q]$. On the lower panels of each figure the ratio of other predictions to CoLoRFulNNLO results can be seen along with a red band showing the relative scale variation of our NNLO results.

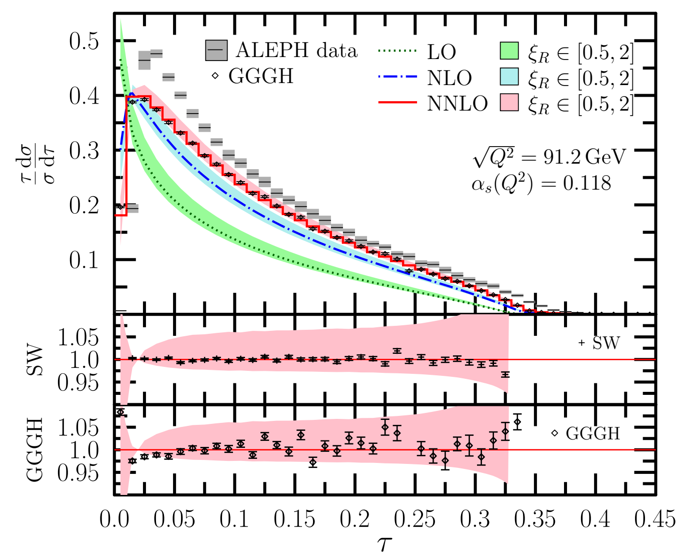

Figure 3.1: Perturbative predictions for thrust distribution ($\tau = 1 - T$) at LO, NLO and NNLO accuracy. The bands were obtained by varying the renormalization scale in the range $\mu_R \in [Q/2, 2Q]$. (In the published paper the dimensionless variable $\xi_R = \mu_R/Q$ was used.) The two lower panels show the ratio of the predictions of [22] (SW) and `EERAD3` [23] (GGGH) to CoLoRFulNNLO.

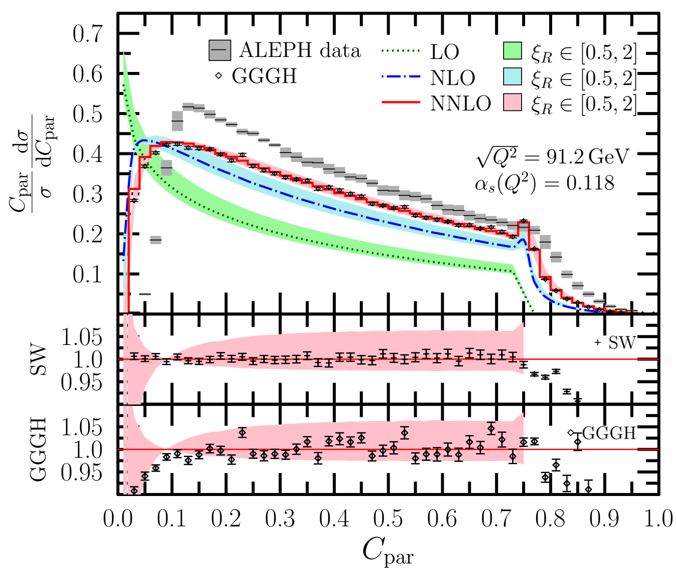

Figure 3.2: Perturbative predictions for C-parameter distribution at LO, NLO and NNLO accuracy. The bands were obtained by varying the renormalization scale in the range $\mu_R \in [Q/2, 2Q]$. (In the published paper the dimensionless variable $\xi_R = \mu_R/Q$ was used.) The two lower panels show the ratio of other predictions of [22] (SW) and `EERAD3` [23] (GGGH) to CoLoRFulNNLO.

Part II

Measurement of the strong coupling

Chapter 4

Motivation

Knowing the precise value of the strong coupling is absolutely essential for the calculation of highly accurate QCD cross sections. As I discussed in the previous part of this work, perturbative QCD predicts only the behavior of the strong coupling at different energy scales but to obtain numerical values we need to measure α_S at a fixed scale. This can be achieved by performing fits to experimental data with the value of the coupling treated as a free parameter. To this end, in the framework of perturbative QCD, event shapes describing global event topology and jet rates have been used extensively in the past.

One of the best sources for the precise extraction of α_S are quantities related to three-jet production in e^+e^- annihilation [24, 25] due to a number of reasons. First of all, the deviation from the simple two-jet configuration is directly proportional to α_S. Furthermore, since the strong interactions occur only in the final state, non-perturbative QCD corrections are restricted to hadronization and power corrections, which may be extracted by comparing measurement data to Monte Carlo simulations or estimated using analytic models. Therefore, the precision of the theoretical computation is limited mostly by the accuracy of the perturbative expansion.

The state of the art for event shape observables currently includes fixed-order NNLO corrections for the six standard three-jet event shapes of thrust, heavy jet mass, total and wide jet broadening, C-parameter and the two-to-three jet transition variable y_{23} [14, 22, 26] as well as jet cone energy fraction [14], oblateness and energy-energy correlation [16]. The three-jet rate in electron-positron annihilation has been computed at NNLO precision [22, 26–28]. Using these results and the total cross section at N^{3}LO accuracy [29] the two-jet rate can be obtained with N^{3}LO precision.

However, fixed-order predictions have a limited kinematical range of applicability. Let us consider a generic event shape y defined such that $y \to 0$ corresponds to the two-jet limit. When the two-jet limit is approached multiple emissions of soft and collinear gluons give rise to large logarithmic corrections in the form of $\alpha_S^n \ln^m y$ where $m \leq 2n-1$ is a natural number. These contributions spoil the convergence of the perturbative series for small values of y and thus invalidate the use of fixed-order perturbation theory in that region. In order to obtain a description appropriate to this limit, the logarithms must be resummed to all orders. Resummation in the highest-order logarithmic correction (the terms containing $\alpha_S^n \ln^{2n-1} y$ in our example) is referred to as *Leading Logarithmic* (LL) while the sub-leading contributions ($\alpha_S^n \ln^{2n-2} y$, $\alpha_S^n \ln^{2n-3} y$, ...) are labelled as *Next-to-Leading Logarithmic* (NLL), *Next-to-Next-to-Leading Logarithmic* (NNLL) and so on. For three-jet event shapes such logarithmically enhanced terms can be resummed at NNLL accuracy [30–36] and even at next-to-next-to-next-to-leading logarithmic ($\mathrm{N^3LL}$) accuracy for thrust [37] and the C-parameter [38]. A prediction incorporating the complete perturbative knowledge about the observable can be derived by matching the fixed-order and resummed calculations [39].

For the standard event shapes of thrust, heavy jet mass, total and wide jet broadening, C-parameter and y_{23}, NNLO predictions matched to NLL resummation were presented in [40]. Predictions at NNLO matched to $\mathrm{N^3LL}$ resummation are also known for thrust [31, 37] and the C-parameter [38].

In this part I will present our results on extracting the value of $\alpha_S(M_Z)$ from measurement data using up-to-date theoretical calculations on hadronic observables in electron-positron annihilation. In Chapter 5 I describe the calculation of energy-energy correlation in perturbation theory using NNLO fixed-order and NNLL resummed results. Furthermore, I present an assessment of the impact of NNLO corrections on the extraction of $\alpha_S(M_Z)$ from experimental data. In Chapter 6 I discuss a more detailed analysis using the results presented in the previous chapter in tandem with hadronization corrections obtained with state-of-the-art Monte Carlo event generators and NLO corrections for b-quark mass. Finally, in Chapter 7 I show a similar analysis based on jet rates.

Chapter 5

Energy-energy correlation in perturbation theory

The completion of the CoLoRFulNNLO scheme for final state radiation allowed us to compute any IR-safe event shape up to NNLO accuracy in electron-positron annihilation. However, this perturbative description in fixed α_S order is, as we will see, insufficient for a full description of physical observables and thus we should consider resummation as well. Previously, the event shape called energy-energy correlation was known only at NLO+NNLL precision. Thus, our aim was to present an upgrade on perturbative results available in the literature by incorporating the NNLO correction and assess its impact on analyses of measurement data. This way we were able to provide the most accurate theoretical prediction on the observable.

5.1 Definition of the observable

Energy-energy correlation (EEC) is the normalized energy-weighted cross section defined in terms of the angle between two particles i and j [41]:

$$\frac{1}{\sigma_t}\frac{\mathrm{d}\Sigma(\chi)}{\mathrm{d}\cos\chi} \equiv \frac{1}{\sigma_t}\int\sum_{i,j}\frac{E_iE_j}{Q^2}\mathrm{d}\sigma_{e^-e^+\to ij+X}\,\delta(\cos\chi-\cos\theta_{ij}), \tag{5.1}$$

where E_i and E_j are the energies of particles i and j, Q^2 is the center-of-mass energy squared, $\theta_{ij}=\chi$ is the angle between the three-momenta of the two particles and σ_t is the total hadronic cross section for $e^+e^-\to hadrons$. The normalization ensures that the integral of the observable between $\chi=0^\circ$ and $\chi=180^\circ$ is one.

The correlation between energies of final-state hadrons is strongest when the particles under consideration are either going in roughly the same or opposite direction.

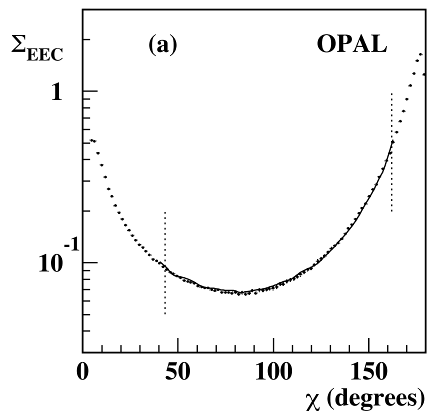

Figure 5.1: Energy-energy correlation in $e^+e^- \to hadrons$ measured by the OPAL Collaboration [42].

Since the production rate of $k > 2$ number of jets is suppressed by a factor of α_S^k relative to the two-jet case, the greatest contribution to EEC comes from two-jet final states. Hence, final-state particles appear mostly with parallel or antiparallel three-momenta and the event shape peaks at low and high values of χ as can be seen on Fig. 5.1. We refer to these regions as the forward and back-to-back region repsectively.

5.2 Fixed-order calculations

The fixed-order expansion of the differential EEC distribution at scale Q up to NNLO can be written as

$$\left[\frac{1}{\sigma_0}\frac{\mathrm{d}\Sigma(\chi,Q)}{d\cos\chi}\right]_{f.o.} = \frac{\alpha_S(Q)}{2\pi}\frac{\mathrm{d}A(\chi)}{\mathrm{d}\cos\chi}+\left(\frac{\alpha_S(Q)}{2\pi}\right)^2\frac{\mathrm{d}B(\chi)}{\mathrm{d}\cos\chi}+\left(\frac{\alpha_S(Q)}{2\pi}\right)^3\frac{\mathrm{d}C(\chi)}{\mathrm{d}\cos\chi}+\mathcal{O}(\alpha_S^4). \tag{5.2}$$

In experiments the measured distribution is normalized to the total hadronic cross section σ_t. Thus to obtain a physical distribution we need to multiply the expansion in Eq. (5.2) by σ_0/σ_t. For massless quarks this ratio is

$$\frac{\sigma_0}{\sigma_t} = 1 - \frac{\alpha_S(Q)}{2\pi}A_t + \left(\frac{\alpha_S(Q)}{2\pi}\right)^2(A_t^2 - B_t) + \mathcal{O}(\alpha_S^3) \tag{5.3}$$

with

$$A_t = \frac{3}{2}C_F, \quad B_t = C_F\left[\left(\frac{123}{8} - 11\zeta_3\right)C_A - \frac{3}{8}C_F - \left(\frac{11}{2} - 4\zeta_3\right)n_f T_R\right]. \tag{5.4}$$

The renormalization scale dependence of the fixed-order distribution can be restored using the renormalization group equation for α_S (see Eq. (2.9)) and we find

$$\begin{aligned}\left[\frac{1}{\sigma_t}\frac{\mathrm{d}\Sigma(\chi,\mu)}{\mathrm{d}\cos\chi}\right]_{f.o.} =& \frac{\alpha_S(\mu)}{2\pi}\frac{\mathrm{d}\bar{A}(\chi,x_R)}{\mathrm{d}\cos\chi} + \left(\frac{\alpha_S(\mu)}{2\pi}\right)^2\frac{\mathrm{d}\bar{B}(\chi,x_R)}{\mathrm{d}\cos\chi} \\ &+ \left(\frac{\alpha_S(\mu)}{2\pi}\right)^3\frac{\mathrm{d}\bar{C}(\chi,x_R)}{\mathrm{d}\cos\chi} + \mathcal{O}(\alpha_S^4)\end{aligned} \tag{5.5}$$

where the expansion coefficients can be expressed in terms of the ones computed at the scale Q as

$$\begin{aligned}\bar{A}(\chi,x_R) =& A(\chi), \\ \bar{B}(\chi,x_R) =& B(\chi) + \left(\frac{1}{2}\beta_0\ln(x_R^2) - A_t\right)A(\chi), \\ \bar{C}(\chi,x_R) =& C(\chi) + (\beta_0\ln(x_R^2) - A_t)B(\chi) \\ &+ \left(\frac{1}{4}\beta_1\ln(x_R^2) + \frac{1}{4}\beta_0\ln^2(x_R^2) - A_t\beta_0\ln(x_R^2) + A_t^2 - B_t\right)A(\chi),\end{aligned} \tag{5.6}$$

with $x_R = \mu/Q$.

The predictions for EEC up to NNLO accuracy are presented in Fig. 5.2 where measured data by the OPAL collaboration [42] is also shown. The bands represent the effect of varying the renormalization scale about its default value of $\mu = Q$ by a factor of two in both directions. Adding higher order corrections reduces the discrepancy between the predictions and data, although considerable differences remain. On one hand, the fixed-order predictions diverge at the edges of the kinematic region but the measured data show no such behavior. On the other hand, there is still some non-negligible difference between the NNLO prediction and the data for medium values of χ.

It should also be noted that in the region of intermediate angles the LO scale variation band does not overlap with the NLO band, while the overlap between the NLO and NNLO bands is marginal down to $\chi \approx 120°$, below which they no longer touch. This indicates that up to at least NLO the customary prescription for scale variation is not a reliable estimate of the size of higher-order corrections and casts some doubt on the reliability of the NNLO band to estimate the uncertainty of the perturbative calculation. This phenomenon is not unique to EEC and in fact very similar comments apply also to other three-jet observables in e^+e^- annihilation [14, 22, 26].

Numerical results for the NNLO fixed-order calculation were obtained using the CoLoRFulNNLO subtraction scheme [12–14]. Computations were performed at the scale $Q = M_Z$ considering $n_f = 5$ light quark flavors.

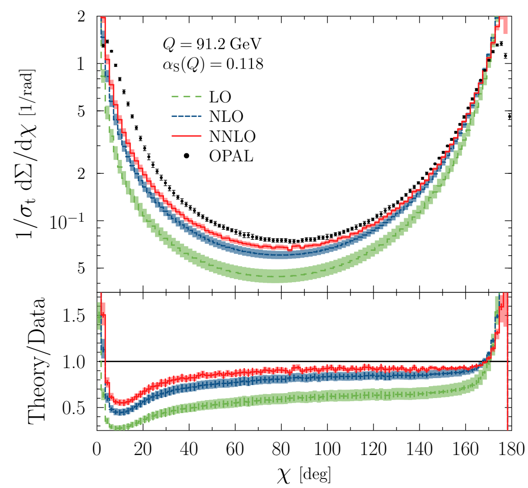

Figure 5.2: Fixed-order predictions for EEC at LO, NLO and NNLO accuracy and OPAL data [42]. The bands are obtained by varying the renormalization scale by a factor of two around the central scale $\mu = Q$.

5.3 Resummation

As we have seen in the previous section, the fixed-order predictions of EEC diverge for both $\chi = 0°$ and $\chi = 180°$ due to large logarithmic contributions of infrared origin. Concentrating on the back-to-back region $\chi \to 180°$, these contributions take the form $\alpha_S^n \ln^{2n-1} y$, where

$$y = \cos^2 \frac{\chi}{2}.$$

As y decreases, the logarithms become large and invalidate the use of the fixed-order perturbative expansion. In order to obtain a proper description of EEC in this limit, the logarithmic contributions must be resummed to all orders.

The resummed prediction has been computed at NNLL accuracy in the back-to-back region in Ref. [30]. At the central scale $\mu = Q$ it can be written as

$$\left[\frac{1}{\sigma_t}\frac{\mathrm{d}\Sigma(\chi, Q)}{\mathrm{d}\cos\chi}\right]_{res.} = \frac{Q^2}{8} H(\alpha_S(Q)) \int_0^\infty \mathrm{d}b\, b J_0(bQ\sqrt{y}) S(Q, b). \tag{5.7}$$

The large logarithmic corrections are exponentiated in the Sudakov form factor

$$S(Q, b) = \exp\left\{ -\int_{b_0^2/b^2}^{Q^2} \frac{\mathrm{d}q^2}{q^2}\left[A(\alpha_S(q^2)) \ln\frac{Q^2}{q^2} + B(\alpha_S(q^2))\right]\right\} \tag{5.8}$$

The zeroth order Bessel function J_0 in Eq. (5.7) and $b_0 = 2e^{-\gamma_E}$ in Eq. (5.8) have a kinematic origin. The functions A, B and H are free of logarithmic corrections and can be computed as perturbative expansions in α_S,

$$A(\alpha_S) = \sum_{n=1}^{\infty} \left(\frac{\alpha_S}{4\pi}\right)^n A^{(n)}, \tag{5.9}$$

$$B(\alpha_S) = \sum_{n=1}^{\infty} \left(\frac{\alpha_S}{4\pi}\right)^n B^{(n)}, \tag{5.10}$$

$$H(\alpha_S) = 1 + \sum_{n=1}^{\infty} \left(\frac{\alpha_S}{4\pi}\right)^n H^{(n)}. \tag{5.11}$$

It is possible to perform the q^2 integration in Eq. (5.8) analytically and the Sudakov form factor can be written as

$$S(Q,b) = \exp[Lg_1(a_S\beta_0 L) + g_2(a_S\beta_0 L) + a_S g_3(a_S\beta_0 L) + \ldots], \tag{5.12}$$

where $a_S = \alpha_S(Q)/(4\pi)$ and $L = \ln(Q^2b^2/b_0^2)$ corresponds to $\ln y$ at large b (the $y \ll 0$ limit corresponds to $Qb \gg 1$ through a Fourier transformation). The functions g_1, g_2 and g_3 correspond to the LL, NLL and NNLL contributions. The explicit forms of the g_i functions are

$$\begin{aligned}
g_1(\lambda, x_R) &= \frac{A^{(1)}}{\beta_0}\frac{\lambda + \ln(1-\lambda)}{\lambda}, \\
g_2(\lambda, x_R) &= \frac{B^{(1)}}{\beta_0}\ln(1-\lambda) + \frac{A^{(1)}\beta_1}{\beta_0^3}\left(\frac{1}{2}\ln^2(1-\lambda) + \frac{\ln(1-\lambda)}{1-\lambda} + \frac{\lambda}{1-\lambda}\right) \\
&\quad - \frac{A^{(2)}}{\beta_0^2}\left(\frac{\lambda}{1-\lambda} + \ln(1-\lambda)\right) - \frac{A^{(1)}}{\beta_0}\left(\frac{\lambda}{1-\lambda} + \ln(1-\lambda)\right)\ln(x_R^2), \\
g_3(\lambda, x_R) &= -\frac{A^{(3)}}{2\beta_0^2}\frac{\lambda^2}{(1-\lambda)^2} - \frac{B^{(2)}}{\beta_0}\frac{\lambda}{1-\lambda} + \frac{A^{(2)}\beta_1}{\beta_0^3}\left(\frac{\lambda(3\lambda-2)}{2(1-\lambda)^2} - \frac{(1-2\lambda)\ln(1-\lambda)}{(1-\lambda)^2}\right) \\
&\quad + \frac{B^{(1)}\beta_1}{\beta_0^2}\left(\frac{\lambda}{1-\lambda} + \frac{\ln(1-\lambda)}{1-\lambda}\right) - \frac{A^{(1)}}{2}\frac{\lambda^2}{(1-\lambda)^2}\ln^2(x_R^2) \\
&\quad - \left[B^{(1)}\frac{\lambda}{1-\lambda} + \frac{A^{(2)}}{\beta_0}\frac{\lambda^2}{(1-\lambda)^2} + A^{(1)}\frac{\beta_1}{\beta_0^2}\left(\frac{\lambda}{1-\lambda} + \frac{1-2\lambda}{(1-\lambda)^2}\ln(1-\lambda)\right)\right]\ln(x_R^2) \\
&\quad + A^{(1)}\left[\frac{\beta_1^2}{2\beta_0^4}\frac{1-2\lambda}{(1-\lambda)^2}\ln^2(1-\lambda) + \ln(1-\lambda)\left(\frac{\beta_0\beta_2 - \beta_1^2}{\beta_0^4} + \frac{\beta_1^2}{\beta_0^4(1-\lambda)}\right)\right. \\
&\quad \left. + \frac{\lambda}{2\beta_0^4(1-\lambda)^2}(\beta_0\beta_2(2-3\lambda) + \beta_1^2\lambda)\right].
\end{aligned} \tag{5.13}$$

These functions diverge as $\lambda \to 1$. This behavior is caused by the Landau pole in the QCD running coupling, thus Eq. (5.7) cannot be treated naively as a real integral. To evaluate it we follow the prescription introuced in Refs. [43–45]. In order to obtain a sensible result we must interpret Eq. (5.8) as a complex contour integral. Due to the presence of the Landau pole, however, the integration contour cannot be simply the real axis. Hence one must write the expression in Eq. (5.7) as the sum of two complex integrals over the contours C_1 and C_2. Parametrizing the contours as

$$C_1:\ b = \begin{cases} t & 0 \le t \le b_c \\ b_c - te^{-\mathrm{i}\phi_b} & 0 \le t \le \infty \end{cases}, \qquad C_2:\ b = \begin{cases} t & 0 \le t \le b_c \\ b_c + te^{\mathrm{i}\phi_b} & 0 \le t \le \infty \end{cases}$$

the singularity caused by the presence of the Landau pole can be avoided by choosing the parameters b_c and ϕ_b appropriately which is visualized in Fig. 5.3. The upper limit of b_c is determined to be $2/Qe^{-\gamma_E}$. This way the expression in Eq. (5.7) can be rewritten as the sum of the two complex integrals over the contours C_1 and C_2. The first segment of these contours is equivalent to taking the original real integral restricted to the region $[0, b_c]$. The imaginary part of the sum of the remaining parts cancels and what remains are just the real parts that are equal. The complexified integral takes the form

$$\begin{aligned}\left[\frac{1}{\sigma_t}\frac{\mathrm{d}\Sigma(\chi,Q)}{\mathrm{d}\cos\chi}\right]_{res.} &= \frac{Q^2}{8}H(\alpha_S(Q)) \int_0^{b_c} \mathrm{d}t\, t\, J_0(tQ\sqrt{y})\, S(Q,t) \\ &+ \frac{Q^2}{8}H(\alpha_S(Q)) \int_0^{\infty} \mathrm{d}t\, 2\mathrm{Re}\left[e^{-\mathrm{i}\phi_b}\, b\, H_0(bQ\sqrt{y})\, S(Q,b)\right]\Big|_{b=b_c-te^{-\mathrm{i}\phi_b}},\end{aligned} \tag{5.14}$$

where H_0 denotes the zeroth order Hankel function of the first kind which arises from extending the Bessel function over the entire complex plane.

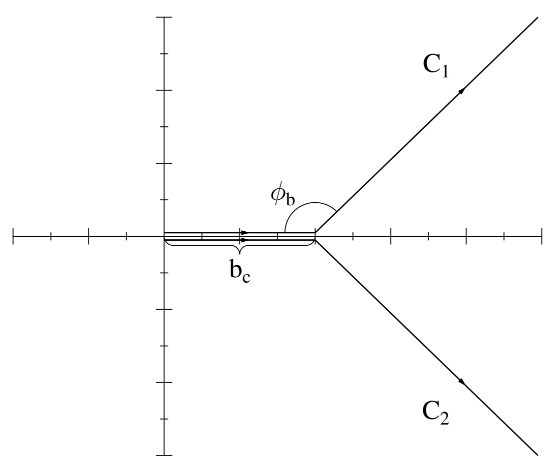

Figure 5.3: Integration contours C_1 and C_2 chosen to avoid the Landau pole.

The constants $A^{(1)}$, $A^{(2)}$ and $A^{(3)}$ [1] that appear in the formulae for the g_i functions

[1] The coefficient $A^{(3)}$ presented in [30] is incomplete. The complete coefficient can be found in [36, 46].

are

$$\begin{aligned}
A^{(1)} &= 4C_F, \\
A^{(2)} &= \left[C_A\left(\frac{67}{9}-\frac{\pi^2}{3}-\frac{20}{9}n_fT_R\right)\right]A^{(1)}, \\
A^{(3)} &= \left[C_A^2\left(\frac{245}{6}-\frac{134\pi^2}{27}+\frac{11\pi^4}{45}+\frac{22}{3}\zeta_3\right)+C_Fn_fT_R\left(-\frac{55}{3}+16\zeta_3\right)\right. \\
&\quad \left.+C_An_fT_R\left(-\frac{418}{27}+\frac{40\pi^2}{27}-\frac{56}{3}\zeta_3\right)-\frac{16}{27}n_f^2T_R^2\right]A^{(1)}+2\beta_0 d_2^q,
\end{aligned} \tag{5.15}$$

where

$$d_2^q = C_AC_F\left(\frac{808}{27}-28\zeta_3\right)-\frac{224}{27}C_Fn_fT_R. \tag{5.16}$$

For $B^{(1)}$ and $B^{(2)}$ we have

$$\begin{aligned}
B^{(1)} &= -6C_F, \\
B^{(2)} &= -2\gamma_q^{(2)}-C_F\beta_0\left(8-\frac{10\pi^2}{3}\right),
\end{aligned} \tag{5.17}$$

with

$$\gamma_q^{(2)} = C_F^2\left(\frac{3}{2}-2\pi^2+24\zeta_3\right)+C_FC_A\left(\frac{17}{6}+\frac{22\pi^2}{9}-12\zeta_3\right)-C_Fn_fT_R\left(\frac{2}{3}+\frac{8\pi^2}{9}\right). \tag{5.18}$$

Finally, $H^{(1)}$ is

$$H^{(1)} = -C_F\left(11+\frac{2\pi^2}{3}\right). \tag{5.19}$$

Fig. 5.4 shows the resummed calculations for EEC up to NNLL accuracy compared to OPAL data. Although these predictions are finite in the back-to-back region and capture the general behavior of data for angles close to 180°, the resummed results become significantly different from the measured data as we move away from the $\chi \to 180°$ limit.

The factorization between the constant and logarithmic terms $H(\alpha_S)$ and $S(Q,b)$ involves some arbitrariness, since the large logarithm L can be modified by a multiplicative constant at order one in the argument of the logarithm. This arbitrariness can be parametrized by introducing the constant x_L as

$$L = \ln(Q^2b^2/b_0^2) = \ln(x_L^2Q^2b^2/b_0^2)-\ln(x_L^2), \tag{5.20}$$

that must satisfy $x_L = \mathcal{O}(1)$ when $Qb \gg 1$. This parameter plays a similar role as the renormalization scale x_R in the fixed-order computations. The rescaling of

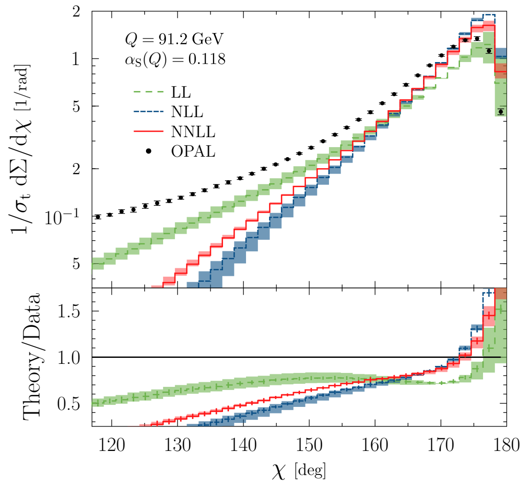

Figure 5.4: Resummed predictions for EEC at LL, NLL and NNLL accuracy and OPAL data. The bands are obtained by varying the renormalization scale by a factor of two around the central scale $\mu = Q$.

the logarithm L modifies the resummation formulae and the expansion coefficients in Eqs. (5.9) – (5.11),

$$\begin{aligned}
\tilde{A}^{(n)}(x_L) &= A^{(n)}, \\
\tilde{B}^{(n)}(x_L) &= B^{(n)} - A^{(n)} \ln(x_L^2), \\
\tilde{H}^{(1)}(x_L) &= H^{(1)} - \beta_0 g_2'(0) \ln(x_L^2) + \beta_0 g_1'(0) \ln^2(x_L^2),
\end{aligned} \tag{5.21}$$

while the Sudakov form factor in Eq. (5.12) also changes as

$$\begin{aligned}
S(Q, b, x_R, x_L) = \exp\Bigg[&\tilde{L} g_1\left(a_S \beta_0 \tilde{L}, \frac{x_R}{x_L}\right) + g_2\left(a_S \beta_0 \tilde{L}, \frac{x_R}{x_L}\right) \\
&+ a_S g_3\left(a_S \beta_0 \tilde{L}, \frac{x_R}{x_L}\right) + \ldots\Bigg],
\end{aligned} \tag{5.22}$$

where $\tilde{L} = \ln(x_L^2 Q^2 b^2 / b_0^2)$. Similarly to the case of the renormalization scale, the resummation scale can be used to assess the impact of neglected higher-order terms in resummation.

5.4 Matching the fixed-order and resummed predictions

At this point two perturbative predictions have been described for EEC that are valid in separate kinematic regions. The fixed-order expansion applies when $\alpha_S \ln^2 y \ll 1$ while the resummation is only reliable for small values of y. They can be understood as series expansions of the same quantity in different ways as shown schematically in Eq. (5.23). The rows correspond to terms in the fixed-order series while the columns represent terms in the resummation expansion.

$$
\begin{array}{llllllllllll}
\frac{1}{\sigma_t}\frac{\mathrm{d}\Sigma}{\mathrm{d}\cos\chi} \sim \frac{1}{y}\Big\{ & \alpha_S \Big[& \log y & + & 1 & & & & & \Big] & & \text{LO} \\
& + \alpha_S^2 \Big[& \log^3 y & + & \log^2 y & + & \log y & + & 1 & \Big] & & \text{NLO} \\
& + \alpha_S^3 \Big[& \log^5 y & + & \log^4 y & + & \log^3 y & + & \log^2 y & \ldots \Big] & \Big\} & \text{NNLO} \\
& & \vdots & & & & & & & & & \\
& & \text{LL} & & \text{NLL} & & \text{NNLL} & & & & &
\end{array}
\tag{5.23}
$$

The two calculations must be matched if we are to obtain a description that is valid over a wide range of y. There are multiple matching procedures worked out and described in the literature (see for example [47]) but they all come down to taking the sum of the two predictions and subtracting the fixed-order expansion of the resummed part to avoid the double counting of the overlap as shown in Eq. (5.24).

$$
\frac{1}{\sigma_t}\frac{\mathrm{d}\Sigma(\chi,\mu)}{\mathrm{d}\cos\chi} = \left[\frac{1}{\sigma_t}\frac{\mathrm{d}\Sigma(\chi,\mu)}{\mathrm{d}\cos\chi}\right]_{\text{res.}} + \left[\frac{1}{\sigma_t}\frac{\mathrm{d}\Sigma(\chi,\mu)}{\mathrm{d}\cos\chi}\right]_{\text{f.o.}} - \left\{\left[\frac{1}{\sigma_t}\frac{\mathrm{d}\Sigma(\chi,\mu)}{\mathrm{d}\cos\chi}\right]_{\text{res.}}\right\}_{\text{f.o.}} \tag{5.24}
$$

However, subtracting the fixed-order expansion of the resummed distribution alone is insufficient to produce a physical prediction. Unless the order of logarithmic approximation is high enough to reproduce all logarithmic singularities of the fixed-order calculation, the last two terms on the right-hand side of Eq. (5.24) will still contain unexponentiated logarithmic contributions that diverge in the forward and back-to-back regions.

In the case of EEC the NNLL approximation is sufficient for the cancellation of singular terms in the LO and NLO fixed-order calculation but that is no longer true at NNLO. Hence, Eq. (5.24) can be used to define a sensible matched prediction at NNLL+NLO precision but not at NNLL+NNLO. For the later case a different matching procedure must be used to obtain a distribution which behaves physically in the back-to-back region. In this work the log-R matching scheme [39] was employed.

In log-R matching one must consider a cumulative event shape distribution denoted here by $R(y,\mu)$ for some event shape y,

$$R(y,\mu) = \frac{1}{\sigma_t}\int_0^y \mathrm{d}y' \, \frac{\mathrm{d}\sigma(y',\mu)}{\mathrm{d}y'} \tag{5.25}$$

which has the following fixed-order expansion

$$\Big[R(y,\mu)\Big]_{\text{f.o.}} = 1 + \frac{\alpha_S}{2\pi}\bar{\mathcal{A}}(y,\mu) + \left(\frac{\alpha_S}{2\pi}\right)^2\bar{\mathcal{B}}(y,\mu) + \left(\frac{\alpha_S}{2\pi}\right)^3\bar{\mathcal{C}}(y,\mu) + \mathcal{O}(\alpha_S^4). \tag{5.26}$$

The specific formulae for log-R matching in the literature [39] apply to event shapes with the cumulative resummed distribution taking a fully exponential form,

$$\begin{aligned}\Big[R(y,\mu)\Big]_{\text{res.}} &= (1 + C_1\alpha_S + C_2\alpha_S^2 + \dots) \\ &\quad\times \exp\Big[Lg_1(\alpha_S L) + g_2(\alpha_S L) + \alpha_S g_3(\alpha_S L) + \dots\Big] + \mathcal{O}(\alpha_S y),\end{aligned} \tag{5.27}$$

where $L = \ln y$ and C_n are known constants and the functions g_n can be expanded in powers of α_S and L as

$$g_n(\alpha_S L) = \sum_{i=1}^{\infty} G_{i,i+2-n}\left(\frac{\alpha_S}{2\pi}\right)^i L^{i+2-n}. \tag{5.28}$$

Performing the log-R matching means expanding the logarithm of Eq. (5.26) as a power series in α_S,

$$\begin{aligned}\ln\Big[R(y,\mu)\Big]_{\text{f.o.}} &= \frac{\alpha_S}{2\pi}\bar{\mathcal{A}}(y,\mu) + \left(\frac{\alpha_S}{2\pi}\right)^2\left(\bar{\mathcal{B}}(y,\mu) - \frac{1}{2}\bar{\mathcal{A}}(y,\mu)^2\right) \\ &\quad + \left(\frac{\alpha_S}{2\pi}\right)^3\left(\bar{\mathcal{C}}(y,\mu) - \bar{\mathcal{A}}(y,\mu)\bar{\mathcal{B}}(y,\mu) + \frac{1}{3}\bar{\mathcal{A}}(y,\mu)^3\right) + \mathcal{O}(\alpha_S^4)\end{aligned} \tag{5.29}$$

and similarly rewriting Eq. (5.27) as

$$\begin{aligned}\ln\Big[R(y,\mu)\Big]_{\text{res.}} &= Lg_1(\alpha_S L) + g_2(\alpha_S L) + \alpha_S g_3(\alpha_S L) \\ &\quad + \alpha_S C_1 + \alpha_S^2\left(C_2 - \frac{1}{2}C_1\right) + \alpha_S^3\left(C_3 - C_1 C_2 + \frac{1}{3}C_1^3\right) + \mathcal{O}(\alpha_S^4).\end{aligned} \tag{5.30}$$

Replacing the terms in Eq. (5.30) up to $\mathcal{O}(\alpha_S^4)$ by the ones in Eq. (5.29) we obtain the final formula for the log-R-matched NNLL+NNLO distribution,

$$\begin{aligned}
\ln\Big[R(y,\mu)\Big] &= Lg_1(\alpha_S L) + g_2(\alpha_S L) + \alpha_S g_3(\alpha_S L) \\
&+ \frac{\alpha_S}{2\pi}\left(\bar{\mathcal{A}}(y,\mu) - G_{11}L - G_{12}L^2\right) \\
&+ \left(\frac{\alpha_S}{2\pi}\right)^2\left(\bar{\mathcal{B}}(y,\mu) - \frac{1}{2}\bar{\mathcal{A}}(y,\mu)^2 - G_{21}L - G_{22}L^2 - G_{23}L^3\right) \\
&+ \left(\frac{\alpha_S}{2\pi}\right)^3\Big(\bar{\mathcal{C}}(y,\mu) - \bar{\mathcal{A}}(y,\mu)\bar{\mathcal{B}}(y,\mu) + \frac{1}{3}\bar{\mathcal{A}}(y,\mu)^3 - G_{32}L^2 - G_{33}L^3 \\
&\qquad - G_{34}L^4\Big).
\end{aligned} \tag{5.31}$$

The constants C_n do not enter Eq. (5.31) as the non-logarithmically enhanced terms containing them must be factorized with respect to the form factor and should not be exponentiated [39].

For EEC two difficulties arise with the application of Eq. (5.31). First, the fixed-order expansion of the event shape diverges at both ends of the kinematic region making the determination of a simple cumulant unfeasible. Second, the resummed distribution is not in a completely exponentiated form. To solve the first issue, we considered a linear combination of moments

$$\frac{1}{\sigma_t}\tilde{\Sigma}(\chi,\mu) \equiv \frac{1}{\sigma_t}\int_0^\chi \mathrm{d}\chi'\,(1-\cos\chi')\frac{\mathrm{d}\Sigma(\chi',\mu)}{\mathrm{d}\chi'}. \tag{5.32}$$

Once the matching procedure is carried out it is straightforward to reproduce the differential EEC distribution from Eq. (5.32) as

$$\frac{1}{\sigma_t}\frac{\mathrm{d}\Sigma(\chi,\mu)}{\mathrm{d}\chi} = \frac{1}{1-\cos\chi}\frac{\mathrm{d}}{\mathrm{d}\chi}\left[\frac{1}{\sigma_t}\tilde{\Sigma}(\chi,\mu)\right]. \tag{5.33}$$

The singularity of the differential distribution in the forward region ($\chi \to 0$) is suppressed by the factor $(1-\cos\chi)$ and in massless QCD

$$\frac{1}{\sigma_t}\tilde{\Sigma}(\pi,\mu) = \frac{1}{\sigma_t}\int\sum_{i,j}\frac{E_iE_j}{Q^2}(1-\cos\theta_{ij})\mathrm{d}\sigma_{e^+e^-\to ij+X} = 1. \tag{5.34}$$

Thus the cumulant can be determined reliably. Now the integration of the fixed-order differential distribution can be carried out and the constraint $\tilde{\Sigma}(\pi,\mu)/\sigma_t = 1$ can be used to set the constants of integration to obtain

$$\left[\frac{1}{\sigma_t}\tilde{\Sigma}(\chi,\mu)\right]_{\text{f.o.}} = 1+\frac{\alpha_S(\mu)}{2\pi}\bar{\mathcal{A}}(\chi,\mu)+\left(\frac{\alpha_S(\mu)}{2\pi}\right)^2\bar{\mathcal{B}}(\chi,\mu)+\left(\frac{\alpha_S(\mu)}{2\pi}\right)^3\bar{\mathcal{C}}(\chi,\mu)+\mathcal{O}(\alpha_S^4). \tag{5.35}$$

For the resummed prediction we can obtain the integral expression for the cumulative distribution using Eq. (5.7) and the definition of $\tilde{\Sigma}$ from Eq. (5.32),

$$\left[\frac{1}{\sigma_t}\tilde{\Sigma}(\chi,\mu)\right]_{\text{res.}} = \frac{H(\alpha_S(\mu))}{2}\int_0^\infty \mathrm{d}b\,\left[Q\sqrt{y}(1-y)J_1(bQ\sqrt{y}) + \frac{2y}{b}J_2(bQ\sqrt{y})\right]\,S(Q,b) \tag{5.36}$$

In order to obtain numerical results, I implemented the numerical integration of the cumulative resummed prediction in a `C++` code based on Gauss quadratures. Due to the Landau-pole, however, a direct computation of Eq. (5.36) as a real integral is impossible. Thus, as it was discussed in the previous chapter for the case of the differential resummed result, I coded the evaluation of the cumulant as a complexified integral.

Although the cumulative resummed prediction is not in a completely exponentiated form, the matching procedure can be performed in the same manner as given before,

$$\begin{aligned}\ln\left[\frac{1}{\sigma_t}\tilde{\Sigma}(\chi,\mu)\right] = \ln\left\{\frac{1}{H(\alpha_S(\mu))}\left[\frac{1}{\sigma_t}\tilde{\Sigma}(\chi,\mu)\right]_{\text{res.}}\right\} - \ln\left\{\frac{1}{H(\alpha_S(\mu))}\left[\frac{1}{\sigma_t}\tilde{\Sigma}(\chi,\mu)\right]_{\text{res.}}\right\}_{\text{f.o.}} \\ + \frac{\alpha_S(\mu)}{2\pi}\bar{\mathcal{A}}(\chi,\mu) + \left(\frac{\alpha_S(\mu)}{2\pi}\right)^2\left[\bar{\mathcal{B}}(\chi,\mu) - \frac{1}{2}\bar{\mathcal{A}}(\chi,\mu)^2\right] \\ + \left(\frac{\alpha_S(\mu)}{2\pi}\right)^3\left[\bar{\mathcal{C}}(\chi,\mu) - \bar{\mathcal{A}}(\chi,\mu)\bar{\mathcal{B}}(\chi,\mu) + \frac{1}{3}\bar{\mathcal{A}}(\chi,\mu)^3\right].\end{aligned} \tag{5.37}$$

Here, the second term on the right hand side of the equation stands for the fixed-order expansion of the resummed prediction,

$$\begin{aligned}\left\{\frac{1}{H(\alpha_S(\mu))}\left[\frac{1}{\sigma_t}\tilde{\Sigma}(\chi,\mu)\right]_{\text{res.}}\right\}_{\text{f.o.}} =& 1 + \frac{\alpha_S(\mu)}{2\pi}\bar{\mathcal{A}}_{\text{res.}}(\chi,\mu) + \left(\frac{\alpha_S(\mu)}{2\pi}\right)^2\bar{\mathcal{B}}_{\text{res.}}(\chi,\mu) \\ &+ \left(\frac{\alpha_S(\mu)}{2\pi}\right)^3\bar{\mathcal{C}}_{\text{res.}}(\chi,\mu) + \mathcal{O}(\alpha_S^4).\end{aligned} \tag{5.38}$$

The exact forms of the coefficients $\bar{\mathcal{A}}_{\text{res.}}$, $\bar{\mathcal{B}}_{\text{res.}}$ and $\bar{\mathcal{C}}_{\text{res.}}$ are given in Appendix A. We must also pay attention to the non-logarithmically enhanced constant terms that come in the form of $H^{(n)}\alpha_S^n$. These contributions must not be exponentiated and thus we need to remove them from the formula of the log-R matched prediction. This is why the resummed prediction is divided by $H(\alpha_S(\mu))$ in Eq. (5.37).

There are other viable matching procedures for NNLL+NNLO calculations in the literature. One can utilize a method similar to Eq. (5.24) which is commonly referred to as R-matching for event shapes and it has been worked out for EEC at NLL+NLO in Refs. [39, 48]. Yet this procedure requires the extraction of certain matching coefficients from the behaviour of the fixed-order prediction deep in the back-to-back limit. Since the computation of the fixed-order distribution in this region is particularly challenging numerically, the necessary coefficients can be obtained only with large numerical uncertainties. This problem becomes more significant at higher orders. Hence, we did not utilize this method. In the case of log-R matching all coefficients can be extracted analitically from the resummed calculation. However, the R-matching in the case of NLO+NNLL can be performed as dictated by Eq. (5.24) without the need for numerically extracted matching coefficients. This allowed us to compare results given by the two matching schemes at NLO+NNLL accuracy which makes for a good check of consistency.

Finally, I note that the unitarity constraint $\tilde{\Sigma}(\pi,\mu)/\sigma_t = 1$ can be satisfied by modifying the resummation formula in Eq. (5.7) such that in the kinematic limit $y = 1$ the Sudakov form factor is unity. There are several methods to achieve this and we chose to modify the coefficients $\tilde{A}^{(n)}$ and $\tilde{B}^{(n)}$ as

$$\begin{aligned}\tilde{A}^{(n)}(x_L) &\to \tilde{A}^{(n)}(x_L)(1-y)^p,\\ \tilde{B}^{(n)}(x_L) &\to \tilde{B}^{(n)}(x_L)(1-y)^p,\end{aligned} \tag{5.39}$$

where p is a positive number. A similar method was employed in Ref. [49], although in a different context. This modification does not alter the logarithmic structure of the result and introduces only power-suppressed terms. The default value is chosen to be $p = 1$.

5.5 Comparison to data

In Ref. [50] we presented the first results on EEC obtained at NNLO+NNLL accuracy and also made comparisons to measurement data. In order to assess the impact of the NNLO contribution we computed the NLO+NNLL predictions as well. At NLO+NNLL accuracy both R and log-R matching can be used to obtain physically sensible results that are valid for medium angles and in the back-to-back region as well. These results are shown in Fig. 5.5 along with the fixed-order NLO prediction. In such comparisons we set the center-of-mass energy to the Z-boson mass, $Q = M_Z = 91.2$ GeV and the strong coupling is fixed to $\alpha_S(M_Z) = 0.118$. The fixed-order calculation diverges to $-\infty$ as $\chi \to 180^\circ$ but the matched results remain well-behaved in both matching schemes. The ratio of the fixed-order NLO and the R-matched calculations to the log-R-matched result is shown in the lower panel of Fig. 5.5. The colored bands were obtained by varying the renormalization scale about its default value in the region $\mu_R \in [Q/2, 2Q]$ using the two-loop running of the strong coupling. It is apparent that the two matching schemes are in good agreement with each other with the relative difference of the R-matched calculation from the log-R-matched one changing from about -2% near $\chi = 180^\circ$ to 0% for $\chi = 60\%$. Around $\chi = 180^\circ$, the difference is about $+0.5\%$.

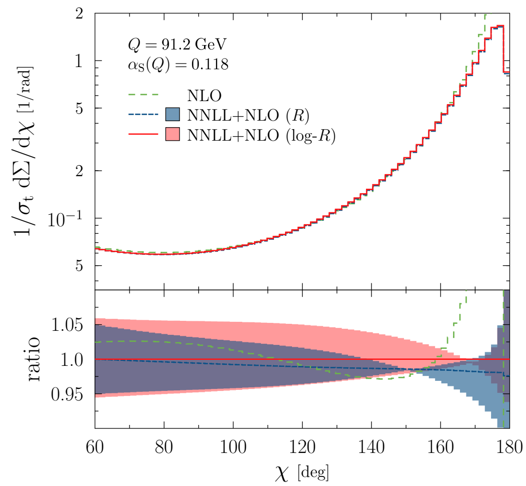

Figure 5.5: Comparison of R-matched and log-R-matched NNLL+NLO predictions for EEC. The bottom panel shows the ratio of fixed-order NLO and R-matched NNLL+NLO predictions to the log-R matched one. The bands were produced by variation of renormalization scale by a factor of two with two-loop running of α_S.

When including the NNLO correction in our discussion we must keep in mind that in order to obtain a result that is physically sensible in the back-to-back region (i.e. for angles close to $\chi = 180°$) we need to use log-R matching. The log-R matched NNLL+NNLO calculation is shown in Fig. 5.6 along with the fixed-order NNLO prediction. Here too, the center-of-mass energy is set to $Q = 91.2$ GeV and we used $\alpha_S(M_Z) = 0.118$. The fixed-order prediction diverges to $+\infty$ as $\chi \to 180°$ (which is not visible on the plot as the NNLO result seems to diverge to $-\infty$). Again, the matched prediction stays well-behaved for angles close to $\chi = 180°$. The ratio of the fixed-order NNLO result to the log-R-matched NNLL+NNLO calculation is shown in the lower panel of Fig. 5.6. The colored bands were obtained by varying the renormalization scale about its default value in the region $\mu_R \in [Q/2, 2Q]$ using the three-loop running of the strong coupling.

In Fig. 5.7 we compare the NNLL+NLO and NNLL+NNLO results in the log-R matching scheme. The ratio of the NNLL+NLO to the NNLL+NNLO result is shown in the lower panel. It can be seen that the inclusion of the NNLO correction lowers the prediction in the region of the peak by -5% to -2% while for medium to low angles we see an increase which is $+7\%$ at $\chi = 120°$ and grows up to $+14\%$ at $\chi = 60°$ and even higher, $20-25\%$ for angles near $0°$. Hence we can deduce that the inclusion of NNLO corrections has a strong impact on the shape of the distribution.

Using the matched prediction described in the previous sections I performed a fit based on the χ^2 method to obtain the value of $\alpha_S(M_z)$ with the goal of assessing the

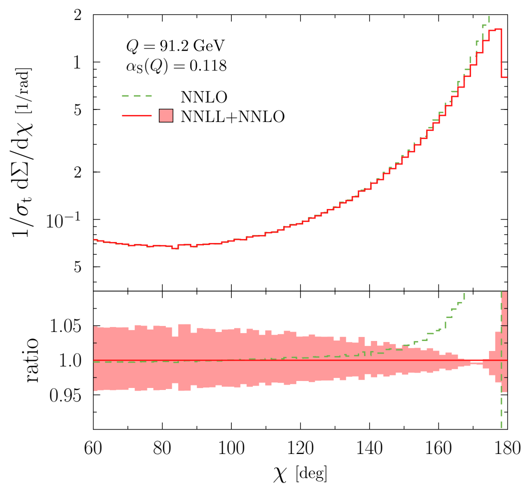

Figure 5.6: NNLL+NNLO matched prediction for EEC compared to the fixed-order NNLO result. The bottom panel shows the ratio of the fixed-order NNLO prediction to the NNLL+NNLO result. The band represents renormalization scale variation of the matched result by a factor of two with three-loop running of α_S.

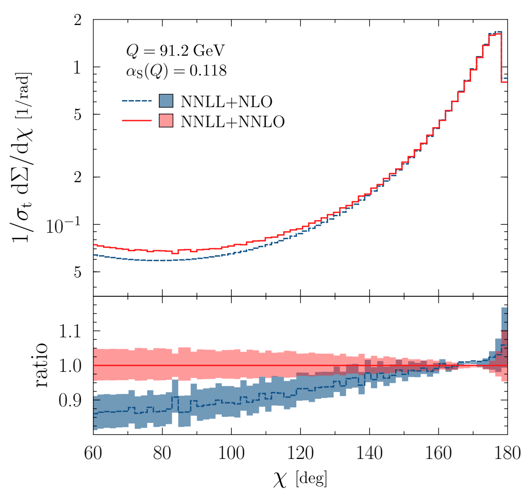

Figure 5.7: Comparison of NNLL+NLO and NNLL+NNLO matched prediction for EEC computed using the log-R scheme. The bottom panel shows the ratio of the NNLL+NLO result to the NNLL+NNLO prediction. The bands were produced by variation of renormalization scale by a factor of two.

impact of the NNLO correction on the final result. I implemented the fit procedure in the same `C++` code as the integration of the resummed prediction and the matching of perturbative results. In order to find the optimal value of $\alpha_S(M_Z)$, I used the `MINUIT2` program [51, 52] to minimize

$$\chi^2(\alpha_S) = \sum_i \frac{(D_i - P_i(\alpha_S))^2}{\sigma_i^2}, \tag{5.40}$$

with the `MIGRAD` method, where the D_i, $P_i(\alpha_S)$ and σ_i stand for the data points, the calculated predictions and the variance respectively. More specifically, the fit was performed by comparing R-matched NNLL+NLO and log-R-matched NNLL+NLO and NNLL+NNLO calculations to precise OPAL [42] and SLD [53] data. In general, both statistical and systematic errors are correlated between bins but the experimental publications provide no information on the matter. Thus, we treat statistical and systematic errors as uncorrelated between data points and add them in quadrature.

In our first fit we neglected hadronization corrections. In order to make the comparison of our results to previous work presented in Ref. [30] straightforward we choose our fit ranges accordingly. Note that our definition of χ differs from the one used in Ref. [30] which can be obtained by simply changing χ to $180° - \chi$. The output of the one-parameter fits is shown in Tab. 5.1. The uncertainties are computed by adding the fit uncertainty and the theoretical uncertainty from missing higher-order contributions in quadrature. The latter is obtained by repeating the fit with several values of the renormalization scale μ_R in the range $\mu_R \in [Q/2, 2Q]$ and taking the envelope of the results. This renormalization scale variation gives the dominant contribution in the total uncertainty.

Fit range	NNLL+NLO (R)		NNLL+NLO (log-R)		NNLL+NNLO (log-R)	
	$\alpha_S(M_Z)$	χ^2/d.o.f.	$\alpha_S(M_Z)$	χ^2/d.o.f.	$\alpha_S(M_Z)$	χ^2/d.o.f.
$117° < \chi < 180°$	0.133 ± 0.001	1.96	0.131 ± 0.003	1.21	0.129 ± 0.003	4.13
$117° < \chi < 165°$	0.132 ± 0.001	0.59	0.131 ± 0.003	0.54	0.128 ± 0.003	1.58
$60° < \chi < 165°$	0.135 ± 0.002	3.96	0.134 ± 0.004	5.12	0.127 ± 0.003	1.12

Table 5.1: Results of the fits of the matched predictions at NNLL+NLO and NNLL+NNLO accuracy to OPAL and SLD data. The number of degrees of freedom of the fits are d.o.f. = 50 for $117° < \chi < 180°$, d.o.f. = 38 for $117° < \chi < 165°$ and d.o.f. = 86 for $60° < \chi < 165°$, where d.o.f. stands for degrees of freedom obtained as #(data points) − #(parameters) − 1.

Our obtained values of $\alpha_S(M_Z)$ based on the R-matched NNLL+NLO calculations are quite close to the results presented in Ref. [30]. The marginal differences are due to the fact that the fits in Ref. [30] were computed using the incomplete $A^{(3)}$ NNLL resummation coefficient.

We observed that by taking the NNLO correction into account the extracted value of $\alpha_S(M_Z)$ was reduced. This decrease is $2-3\%$ for fits performed in the $[117°, 180°]$ range, $2-4\%$ for $[117°, 165°]$ and $5-7\%$ for $[60°, 165°]$, depending on the matching scheme used in the NNLL+NLO calculations. Therefore, it is apparent that the NNLO correction must be included in a precise determination of $\alpha_S(M_Z)$.

So far we have omitted hadronization corrections in our analysis, although we can expect that non-perturbative effects would be relevant, especially at angles close to $\chi = 180°$ [41,54–57]. The OPAL analysis of Ref. [42] also found hadron-parton correction factors ranging from 1.5 in the back-to-back region to 0.9 in the forward region. Thus we must also consider such corrections when aiming for a precise extraction of $\alpha_S(M_Z)$. These non-perturbative corrections can be estimated either by comparison to the output of Monte Carlo event generators or by analytic calculations. Here, we follow the latter option and apply the model presented by Dokshitzer, Marchesini and Weber (hence the label *DMW*) in Ref. [48], which incorporates non-perturbative corrections by multiplying the Sudakov form factor of Eq. (5.8) by

$$S_{NP} = e^{-\frac{1}{2}a_1 b^2}(1 - 2a_2 b), \tag{5.41}$$

where the two parameters a_1 and a_2 as well must be fitted to data.

After complementing our calculations with the analytic non-perturbative model we have performed three-parameter fits to the OPAL and SLD data in the range $[117°, 180°]$ using our NNLL+NNLO prediction as well as the NNLL+NLO predictions obtained in both matching schemes. At NNLL+NLO accuracy in the R matching scheme we obtain the following values:

$$\alpha_S(M_Z) = 0.134^{+0.001}_{-0.009}\,, \quad a_1 = 1.55^{+4.26}_{-1.54}\ \mathrm{GeV}^2\,, \quad a_2 = -0.13^{+0.50}_{-0.05}\ \mathrm{GeV}\,, \tag{5.42}$$

with $\chi^2/\mathrm{d.o.f.} = 38.7/48 = 0.81$. Once again, all uncertainties are computed by adding the fit uncertainties and theoretical uncertainties in quadrature. The theoretical uncertainties were computed by changing the renormalization scale μ_R about its default value $\mu_R = Q$ in the range $[Q/2, 2Q]$ and repeating the fit. The overall uncertainties are dominated by the theoretical contribution with the exception of the upper limit for the strong coupling. The correlation matrix of the fit for the central values is

$$\mathrm{corr}(\alpha_S, a_1, a_2) = \begin{pmatrix} 1 & 0.04 & -0.70 \\ 0.04 & 1 & -0.03 \\ -0.70 & -0.03 & 1 \end{pmatrix}. \tag{5.43}$$

The obtained values of the strong coupling and the parameter a_2, evidently, are strongly anti-correlated.

The analysis presented in [30] gave $|a_2| < 0.002$ GeV and hence they set $a_2 = 0$ and performed a two-parameter fit producing the best fit values of $\alpha_S(M_Z) = 0.130^{+0.002}_{-0.004}$ and $a_1 = 1.5^{+3.2}_{-0.5}$ GeV^2 with χ^2/d.o.f. $= 0.99$. Our result of Eq. (5.42) is in agreement with these values. Nevertheless, we have verified that the source of the discrepancy between the two analyses is, once again, the fact that in Ref. [30] the incomplete $A^{(3)}$ coefficient was used.

Repeating the same fit of NNLL+NLO calculations, this time using the log-R scheme we get

$$\alpha_S(M_Z) = 0.128^{+0.002}_{-0.006}\,, \quad a_1 = 1.17^{+1.46}_{-0.29}\,\mathrm{GeV}^2\,, \quad a_2 = 0.13^{+0.14}_{-0.09}\,\mathrm{GeV}\,, \tag{5.44}$$

with χ^2/d.o.f. $= 40.8/48 = 0.85$ for the central values with a correlation matrix of

$$\mathrm{corr}(\alpha_S, a_1, a_2) = \begin{pmatrix} 1 & -0.17 & -0.98 \\ -0.17 & 1 & 0.08 \\ -0.98 & 0.08 & 1 \end{pmatrix}\,. \tag{5.45}$$

We observed that the quality of the fits for the NNLL+NLO is very similar, as indicated by the reduced χ^2 values, although the strong coupling and the parameter a_2 are even more strongly anti-correlated in the latter case. The fit results are also compatible within uncertainties. The extracted value of $\alpha_S(M_Z)$ is 5% lower for the log-R-matched NNLL+NLO fit but it still remains higher than the world average [1, 2, 58]. Comparison of the NNLL+NLO fits and data is presented in Fig. 5.8 which shows a nice overall agreement with the experimental data. However, there is a slight systematic deviation for intermediate angles. This deviation becomes evident when we consider the ratio of data to log-R-matched calculation as shown in the lower panel of Fig. 5.8. Clearly the shape of the measured EEC distribution is not entirely reproduced by the NNLL+NLO calculation.

Next we repeated the three-parameter fit in the same region using the log-R-matched NNLL+NNLO prediction and extracted the following values:

$$\alpha_S(M_Z) = 0.121^{+0.001}_{-0.003}\,, \quad a_1 = 2.47^{+0.48}_{-2.38}\,\mathrm{GeV}^2\,, \quad a_2 = 0.31^{+0.27}_{-0.05}\,\mathrm{GeV}\,, \tag{5.46}$$

with χ^2/d.o.f. $= 56.7/48 = 1.18$ indicating an improvement of the fit quality compared to the NNLL+NLO results. Yet again, the values obtained for $\alpha_S(M_Z)$ and a_2 are strongly anti-correlated as evidenced by the correlation matrix

$$\mathrm{corr}(\alpha_S, a_1, a_2) = \begin{pmatrix} 1 & 0.05 & -0.97 \\ 0.05 & 1 & -0.07 \\ -0.97 & -0.07 & 1 \end{pmatrix}\,. \tag{5.47}$$

The extracted value of the strong coupling is greatly reduced and it is compatible with the world average within uncertainties [1, 2, 58].

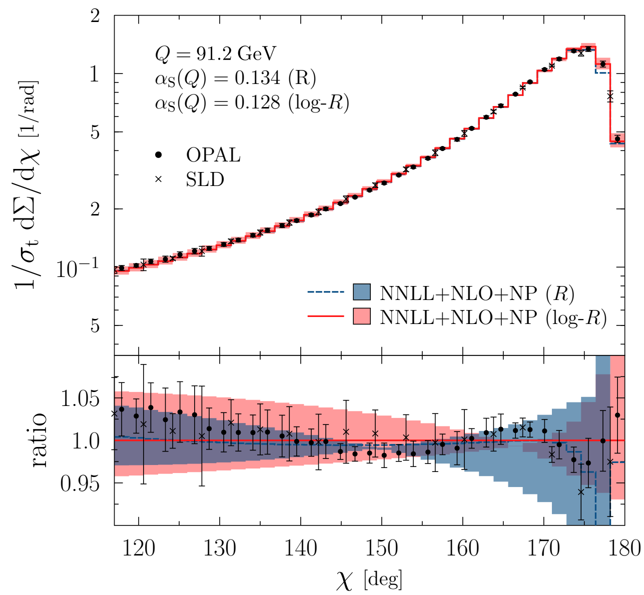

Figure 5.8: NNLL+NLO matched predictions for EEC in the R and log-R matching schemes. The analytic model of Eq. (5.41) is used to account for hadronization corrections (NP). The bottom panel shows the ratio of the data and the R matched prediction to the log-R matched result. The bands represent the effect of varying the renormalization scale μ_R in the range $[Q/2, 2Q]$ with two-loop running of the strong coupling.

In Fig. 5.9 we compare the NNLL+NNLO fit, supplemented with the analytic non-perturbative correction, to the experimental data. Altogether we see that the shape of the EEC distribution is better modelled by the NNLL+NNLO prediction since the systematic deviation present in the NNLL+NLO case is now completely erased. We can also see a narrower renormalization scale band on the NNLL+NNLO results that indicates smaller theoretical uncertainties. However, the strong anti-corrlation between the value of $\alpha_S(M_Z)$ and one of the parameters of Eq. (5.41) suggests that the effect of hadronization was partially taken into account by an adjustment of the value of the coupling. We concluded that the inclusion of the NNLO correction is essential for a precise determination of the strong coupling from EEC but the corrections from the analytic hadronization model are unable to fully describe the data.

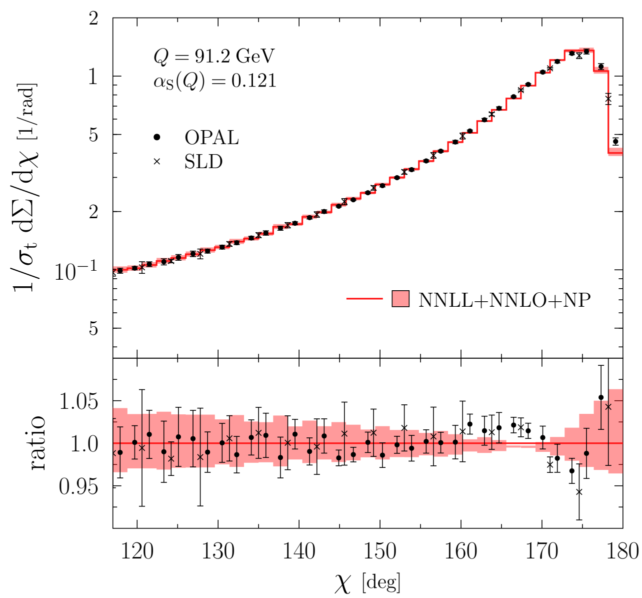

Figure 5.9: NNLL+NNLO matched prediction for EEC. The analytic model of Eq. (5.41) is used to account for hadronization corrections (NP). The bottom panel shows the ratio of the data to the matched result. The band represents the variation of the renormalization scale μ_R in the range $[Q/2, 2Q]$ with three-loop running of the strong coupling.

Chapter 6

Precise determination of $\alpha_S(M_Z)$ from EEC

In the previous chapter we have seen that the NNLO correction to energy-energy correlation has a significant impact on extracting the precise value of the strong coupling from this event shape. Hadronization corrections were taken into account by applying an analytic model. This approach, however, proved to be insufficient for handling non-perturbative effects.

The estimation of hadronization corrections is an integral part of comparing the parton-level pQCD predictions to data measured at hadron level. Despite the fact that under certain conditions the local parton-hadron duality leads to close values of qunatities at parton and hadron level, the difference between them is not negligible.

Building on the results of the previous chapter, here I present a more extensive analysis of energy-energy correlation which utilizes modern Monte Carlo event generators for obtaining non-perturbative corrections with the goal of extracting the precise value of the strong coupling at the M_Z scale.

6.1 Data and non-perturbative corrections

In order to extract the strong coupling the theoretical predictions described in chapter 5 were fit to the available measurement data obtained in the SLD [53], L3 [59], DELPHI [60], OPAL [42, 61], JADE [62], MAC [63], MARKII [64], TASSO [65], CELLO [66], PLUTO [67] and TOPAZ [68] experiments. Information on datasets is detailed in Tab. 6.1. The criteria to include data were high precision of differential distributions with charged and neutral final-state particles in the full kinematic range, presence of corrections for detector effects, correction for initial state photon radiation and sufficient amount of supplementary information.

Experimental datasets selected for the extraction of the strong coupling have high precision and the measurements from different experiments performed at close energies are consistent which justified their use in a wide center-of-mass energy interval.

Experiment	$\sqrt{s}$, GeV, data	$\sqrt{s}$, GeV, MC	Events
SLD [53]	91.2(91.2)	91.2	60000
OPAL [42]	91.2(91.2)	91.2	336247
OPAL [61]	91.2(91.2)	91.2	128032
L3 [59]	91.2(91.2)	91.2	169700
DELPHI [60]	91.2(91.2)	91.2	120600
TOPAZ [68]	59.0 – 60.0(59.5)	59.5	540
TOPAZ [68]	52.0 – 55.0(53.3)	53.3	745
TASSO [65]	38.4 – 46.8(43.5)	43.5	6434
TASSO [65]	32.0 – 35.2(34.0)	34.0	52118
PLUTO [67]	34.6(34.6)	34.0	6964
JADE [62]	29.0 – 36.0(34.0)	34.0	12719
CELLO [66]	34.0(34.0)	34.0	2600
MARKII [64]	29.0(29.0)	29.0	5024
MARKII [64]	29.0(29.0)	29.0	13829
MAC [63]	29.0(29.0)	29.0	65000
TASSO [65]	21.0 – 23.0(22.0)	22.0	1913
JADE [62]	22.0(22.0)	22.0	1399
CELLO [66]	22.0(22.0)	22.0	2000
TASSO [65]	12.4 – 14.4(14.0)	14.0	2704
JADE [62]	14.0(14.0)	14.0	2112

Table 6.1: Data used in the extraction procedure. The average of $\sqrt{s}$ (used for MC generation) is given in the brackets.

In this analysis, non-perturbative effects in $e^+e^- \to$ hadrons process were modelled by using state-of-the-art particle-level Monte Carlo (MC) generators. The non-perturbative corrections of EEC were extracted as ratios of EEC distributions at hadron and parton level in the simulated samples. To tame statistical fluctuations, hadronization corrections were parametrized by smooth functions that are valid only in the fit range. These corrections were then applied as multiplicative factors to the perturbative prediction. In this study the Monte Carlo generators `SHERPA2.2.4` [69] and `Herwig7.1.1` [70] were utilized. For information on generator settings used in our study, see [71].

In order to test the hadronization model dependence, the events generated with `SHERPA2.2.4` were hadronized using the Lund string model [72] and the cluster model [73]. Results obtained with the two setups are labelled S^L and S^C respectively. For the cross-check of `SHERPA2.2.4` samples, the `Herwig7.1.1` generator was used with the default implementation of the cluster model. This setup is labelled H^M.

Predictions obtained with each setup describe the data well for all ranges of χ with the exception of regions near $\chi = 0°$ and $\chi = 180°$, for all $\sqrt{s}$ energy scales. For $\sqrt{s} < 29$ GeV the H^M setup is sensitive to the value of b-quark mass and the corresponding predictions are not reliable.

Since the `SHERPA2.2.4` setups give the most stable and physically reliable predictions, they were used in the analysis for reference hadronization corrections (S^L) and systematic studies (S^C). Samples of the corresponding non-perturbative corrections together with parametrizations are shown in Fig. 6.1. As expected, the size of hadronization correcitons decreases as Q increases.

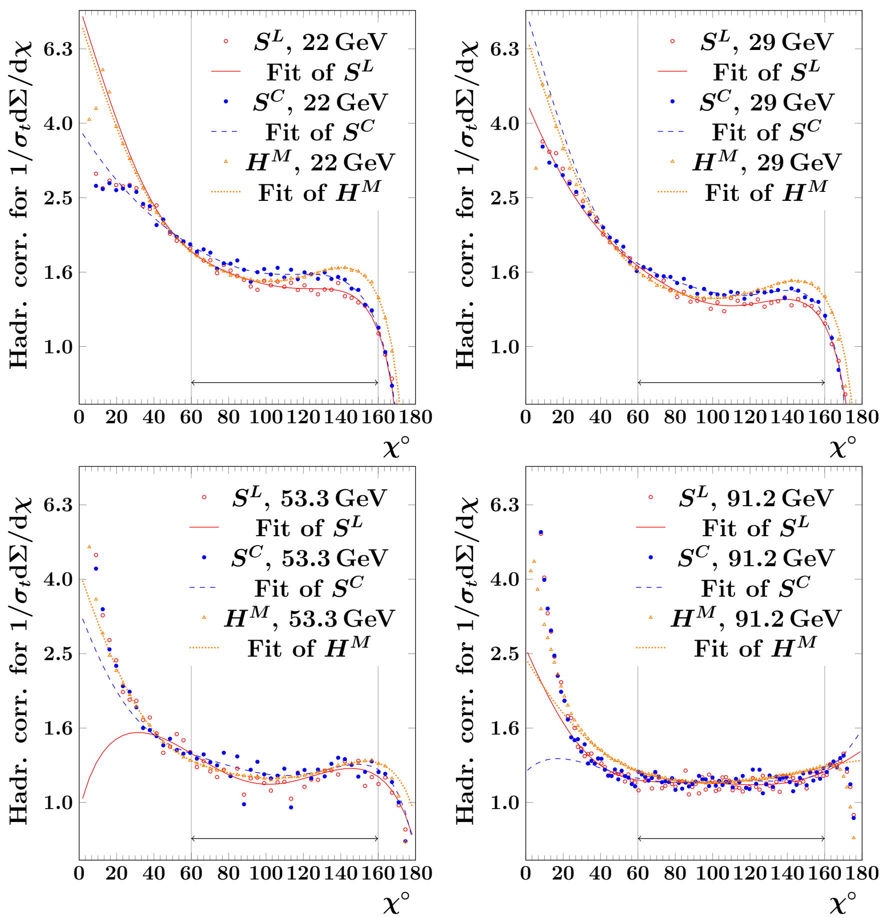

Figure 6.1: Hadronization corrections obtained with different setups of Monte Carlo event simulations and corresponding parametrizations. The used fit range is indicated with a thick line.

Furthermore, the analytic DMW model presented in Chapter 5 was also implemented in this analysis as a cross-check.

6.2 Finite b-quark mass corrections

The perturbative description presented in Chapter 5 assumes that all quark masses are negligible. However, as we have included experimental data with energy scales as low as $\sqrt{s} = 14$ GeV this assumption is no longer fully justified as the mass of the b-quark can no longer be neglected. Mass effects were included directly at the level of matched distributions

$$\frac{1}{\sigma_t}\frac{\mathrm{d}\Sigma(\chi,Q)}{\mathrm{d}\cos\chi} = (1-r_b(Q))\frac{1}{\sigma_t}\left[\frac{\mathrm{d}\Sigma(\chi,Q)}{\mathrm{d}\cos\chi}\right]_{\text{massless}} + r_b(Q)\frac{1}{\sigma_t}\left[\frac{\mathrm{d}\Sigma(\chi,Q)}{\mathrm{d}\cos\chi}\right]^{NNLO*}_{\text{massive}}, \tag{6.1}$$

where the first term on the right hand side is the NNLO+NNLL matched distribution computed in massless pQCD with the log-R scheme and the second term is the massive fixed-order prediction. Since the full NNLO correction to this distribution was unknown at the time this dissertation was written, we modelled it by combining the massive NLO prediction of the parton-level Monte Carlo generator `Zbb4` [74] with the NNLO contribution of the massless distribution.

The fraction of b-quark event that appears in Eq. (6.4) is defined as the ratio of the total b-quark production cross section to the total hadronic cross section, both computed in the framework of massive QCD, to NNLO with exact mass depedence at $\mathcal{O}(\alpha_S)$ and to leading order in m_b^2/Q^2 at $\mathcal{O}(\alpha_S^2)$ [75]

$$r_b(Q) = \frac{\sigma_{\text{massive}}(e^+e^- \to b\bar{b})}{\sigma_{\text{massive}}(e^+e^- \to \text{hadrons})}. \tag{6.2}$$

Distributions for the massive differential cross section were generated at every considered energy scale with a pole b-quark mass of $m_b = 4.75$ GeV, which is consistent with the world average estimations of pole mass 4.78 ± 0.06 GeV [58].

In order to estimate the uncertainty of the b-quark mass corrections, we have investigated two alterntive approaches for including them in our calculations. In approach A Eq. (6.4) is modified as

$$\begin{aligned}\frac{1}{\sigma_t}\frac{\mathrm{d}\Sigma(\chi,Q)}{\mathrm{d}\cos\chi} = \frac{1}{\sigma_t}\left[\frac{\mathrm{d}\Sigma(\chi,Q)}{\mathrm{d}\cos\chi}\right]_{\text{massless}} &+ r_b(Q)\frac{1}{\sigma_t}\left[\frac{\mathrm{d}\Sigma(\chi,Q)}{\mathrm{d}\cos\chi}\right]^{NLO*}_{\text{massive}} \\ &- r_b(Q)\frac{1}{\sigma_t}\left[\frac{\mathrm{d}\Sigma(\chi,Q)}{\mathrm{d}\cos\chi}\right]^{NLO*}_{\text{massless}},\end{aligned} \tag{6.3}$$

where we just subtract the massless fixed-order NLO prediction weighted by $r_b(Q)$ and add the corresponding massive NLO distribution. In approach B we consider mass effects similarly to Eq. (6.4) but we do not include any NNLO corrections to the massive distribution,

$$\frac{1}{\sigma_t}\frac{\mathrm{d}\Sigma(\chi,Q)}{\mathrm{d}\cos\chi} = (1-r_b(Q))\frac{1}{\sigma_t}\left[\frac{\mathrm{d}\Sigma(\chi,Q)}{\mathrm{d}\cos\chi}\right]_{\text{massless}} + r_b(Q)\frac{1}{\sigma_t}\left[\frac{\mathrm{d}\Sigma(\chi,Q)}{\mathrm{d}\cos\chi}\right]^{NLO}_{\text{massive}}. \tag{6.4}$$

6.3 Fit procedure and estimation of uncertainties

In order to obtain an $\alpha_S(M_Z)$ value that best describes the experimental data considered, the `MINUIT2` program was used to minimize

$$\chi^2(\alpha_S) = \sum_{\text{data sets}} \chi^2(\alpha_S)_{\text{data set}} \tag{6.5}$$

with the $\chi^2(\alpha_S)$ values calculated for each data set as

$$\chi^2(\alpha_S) = (\vec{D} - \vec{P}(\alpha_S))V^{-1}(\vec{D} - \vec{P}(\alpha_S))^T, \tag{6.6}$$

where $\vec{D}$ stands for the vector of data points, $\vec{P}(\alpha_S)$ for the vector of calculated predictions and V for the covariance matrix. The default scale was set to $\mu = Q$. The measurements in the original publications were provided without correlations. The correlation matrix was estimated from the Monte-Carlo-simulated samples and together with the statistical uncertainties it was used to build the statistical covariance matrix. The systematic covariance matrix was constructed from the systematic uncertainties provided in the original publications with the assumption that these are correlated with correlation coefficient 0.5 between closest points. The covariance matrix used in the fit for every data set was the sum of the statistical and systematic covariance matrices.

Fits were performed in the ranges $117° - 165°$, $60° - 165°$and $60° - 160°$that were chosen such as to avoid regions where either the perturbative calculations break down or non-perturbative corrections become unreliable. The fit uncertainty was computed according to the χ^2+1 criterion as it was implemented in `MINUIT2`. Fit results for each range are presented in Tab. 6.2 for both NLO+NNLL and NNLO+NNLL perturbative predictions with the aim of estimating the effect of the NNLO correction. The value of the reduced χ^2 indicates an overall better fit quality for the NNLO+NNLL and the predictions also show an increased stability to the variation of the fit range in the case of S^L, S^C and H^M but not for the DMW analytic hadronization model.

The uncertainty of the fit results was estimated by considering the effect of neglecting higher-order terms in the perturbative expansion, the bias of hadronization model selection and the uncertainty of the fit procedure. Since the perturbative results were obtained by combining fixed-order and resummed predictions, the estimation of their uncertainties was two-fold. The effect of missing higher-order contributions on the NNLO+NNLL distribution was assessed by repeating the fits at different renormalization and resummation scales, separately varying them in the ranges $x_R \in [1/2, 2]$ and $x_L \in [1/2, 2]$ respectively.

Furthermore, to estimate the bias arising from the ambiguity of the prescription for implementing the unitarity constraint in the resummed calculation, fits were per-

Fit range, Hadronization	NLO+NNLL $\chi^2/d.o.f.$	NNLO+NNLL $\chi^2/d.o.f.$
$117^\circ - 165^\circ$ S^L	0.12042 ± 0.00025 $765.39/298 = 2.57$	0.11760 ± 0.00020 $513.39/298 = 1.72$
$60^\circ - 165^\circ$ S^L	0.12134 ± 0.00023 $1720.22/664 = 2.59$	0.11746 ± 0.00018 $1211.37/664 = 1.82$
$60^\circ - 160^\circ$ S^L	0.12200 ± 0.00023 $1417.21/623 = 2.27$	0.11750 ± 0.00018 $1021.80/623 = 1.64$
$117^\circ - 165^\circ$ S^C	0.11796 ± 0.00022 $630.96/298 = 2.12$	0.11521 ± 0.00017 $394.75/298 = 1.32$
$60^\circ - 165^\circ$ S^C	0.11900 ± 0.00021 $1556.64/664 = 2.34$	0.11530 ± 0.00015 $950.54/664 = 1.43$
$60^\circ - 160^\circ$ S^C	0.11973 ± 0.00022 $1320.86/623 = 2.12$	0.11545 ± 0.00016 $844.94/623 = 1.36$
$117^\circ - 165^\circ$ H^M	0.11272 ± 0.00037 $1841.85/298 = 6.18$	0.11044 ± 0.00029 $1201.25/298 = 4.03$
$60^\circ - 165^\circ$ H^M	0.11472 ± 0.00033 $3845.09/664 = 5.79$	0.11180 ± 0.00023 $2203.31/664 = 3.32$
$60^\circ - 160^\circ$ H^M	0.11634 ± 0.00033 $3091.25/623 = 4.96$	0.11281 ± 0.00023 $1738.38/623 = 2.79$
$117^\circ - 165^\circ$ $An.^{DMW}$	0.12154 ± 0.00045 $730.15/295 = 2.48$	0.11781 ± 0.00034 $557.60/295 = 1.89$
$60^\circ - 165^\circ$ $An.^{DMW}$	0.13555 ± 0.00053 $7525.37/661 = 11.38$	0.12937 ± 0.00041 $4896.26/661 = 7.41$
$60^\circ - 160^\circ$ $An.^{DMW}$	0.13933 ± 0.00017 $5325.52/620 = 8.59$	0.12950 ± 0.00043 $4826.57/620 = 7.78$

Table 6.2: Fit results for the matched predictions at NLO+NNLL and NNLO+NNLL accuracy. The given uncertainty is the fit uncertainty scaled by $\sqrt{\chi^2/d.o.f.}$, where $d.o.f.$ stands for degrees of freedom obtained as #(data points) − #(parameters) − 1.

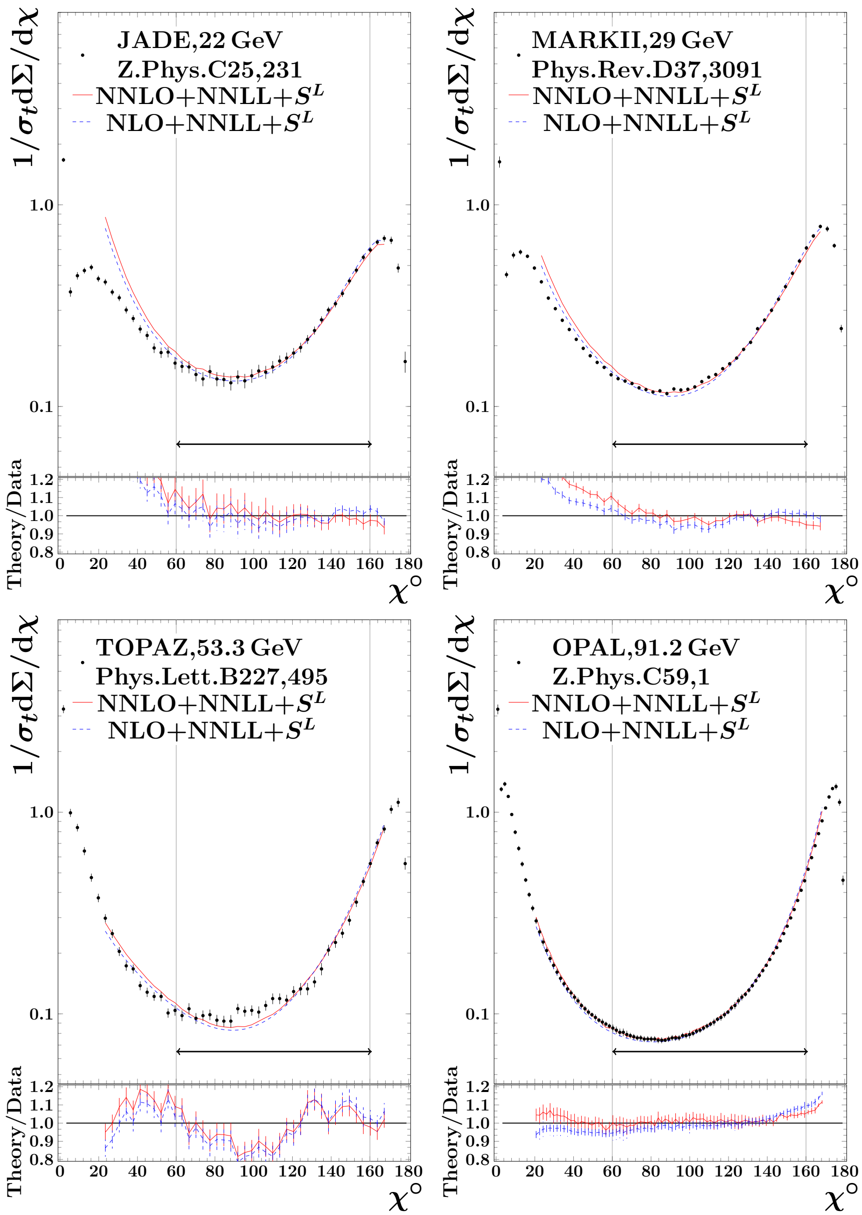

Figure 6.2: Fits of theoretical predictions to data at different center-of-mass energies. The used fit range is indicated on each plot.

formed at $p = 1$ and $p = 2$. (See Eq. (5.39).) The difference of the obtained results is miniscule and as such it was neglected in the estimation of the total uncertainty.

In order to estimate the uncertainty caused by neglecting the b-quark mass, fits were performed using the default massless setup along with the massive setup and approaches A and B as discussed in Section 6.2.

In all cases detailed above, the numerical value of the uncertainties was computed as half of the difference between the maximal and minimal α_S value obtained in the corresponding set of fits. The bias caused by the choice of hadronization model and parton shower model was assessed by performing fits using all previously described setups. The numerical value of the uncertainty was computed as half of the difference between the α_S values obtained using non-perturbative corrections from Lund and cluster hadronization models implemented in `SHERPA2.2.4`. The size of the biases discussed here is shown on Fig. 6.3. Since the estimated uncertainties are mostly independent they are combined as a sum of quadratures in the final result.

Besides the estimation of uncertainties, we performed several cross checks on the results. The data sets were sorted according to energy and were fitted separately at each energy scale. The obtained $\alpha_S(M_Z)$ values are shown on Fig. 6.4. The fit results do not show any visible trend in the case of S_L and S_C. For H_M the results are unreliable below 29 GeV which is caused by the sensitivity of the setup to the b quark mass.

Additionally, the extraction of $\alpha_S(M_Z)$ was also performed using the DMW analytic hadronization model instead of the Monte Carlo setups. The parameters a_1 and a_2 that appear in Eq. 5.41 can be related to certain moments $\bar{\alpha}_{p,q}$ of the coupling α_S [48]. These moments are the fit parameters of the analytic hadronization model in our second analysis. The results obtained with this setup show a strong dependence on the selected fit range, however, the extracted value of $\alpha_S(M_Z)$ is close to the ones obtained using the Monte Carlo setups in the fit range $117° - 165°$. This suggests that the analytic model cannot fully describe non-perturbative effects away from the back-to-back region.

6.4 Phenomenological results

In Ref. [71] we presented the first combined analysis and extraction of the strong coupling α_S at NNLO+NNLL accuracy from energy-energy correlation in electron-positron annihilation using Monte Carlo generators for estimating non-perturbative effects. Furthermore, ours is the first extraction of the strong coupling based on Monte Carlo hadronization corrections obtained from NLO Monte Carlo setups at

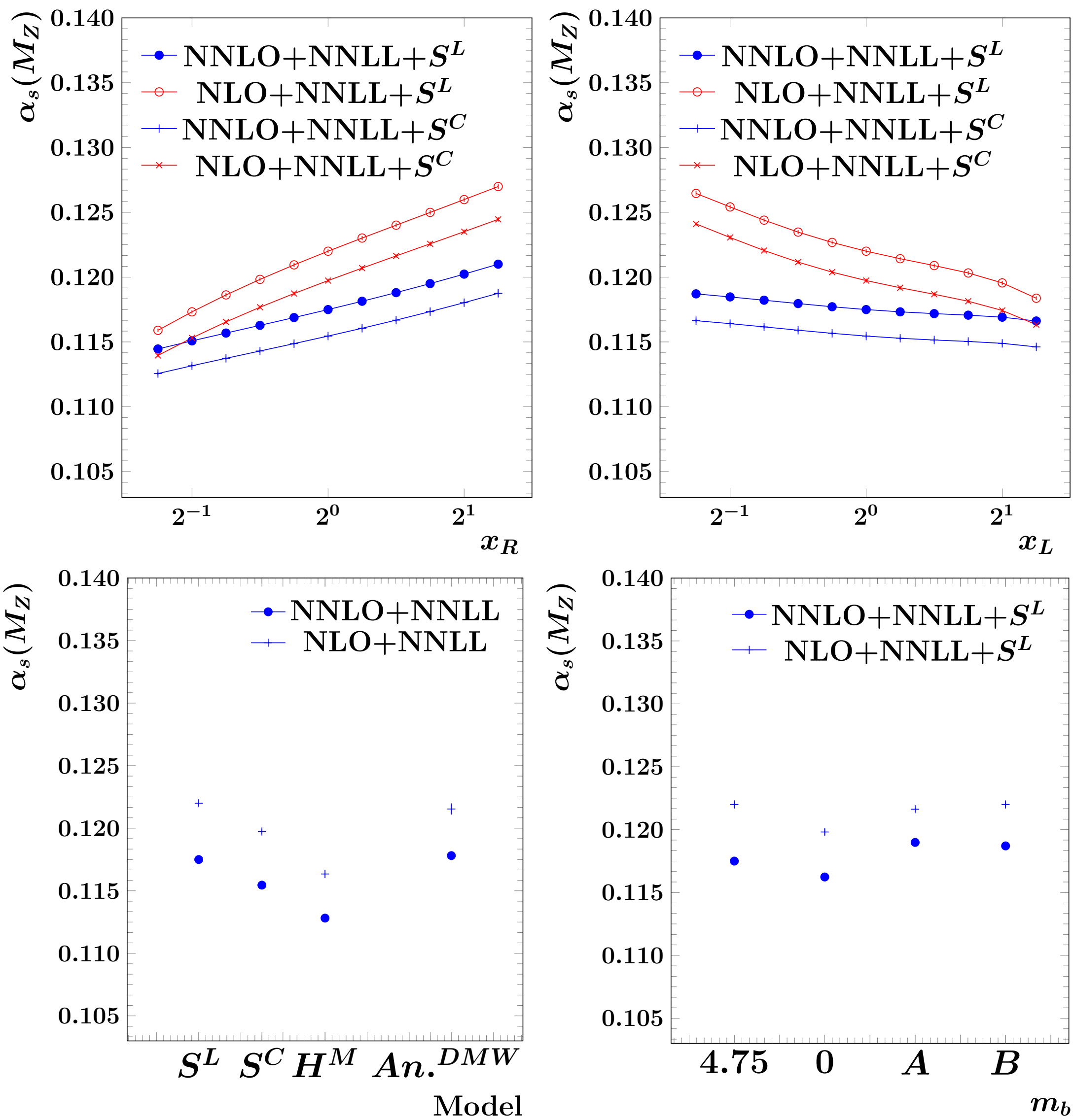

Figure 6.3: Dependence of fit results of renormalization scale (upper left), resummation scale (upper right), hadronization model (bottom left) and b mass corrections (bottom right).

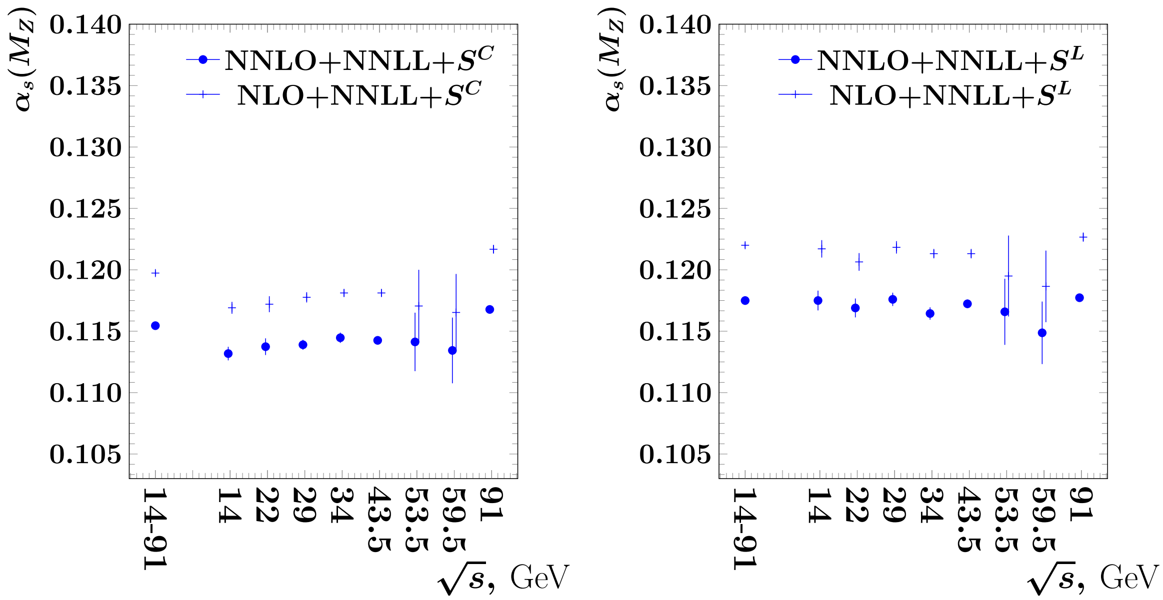

Figure 6.4: Dependence of the fit results on the used data sets. The fit range for every shown setup is $60° - 160°$

NNLO+NNLL precision. For the central value of the final result I quote the results obtained with the S_L hadronization model in the fit range $60° - 160°$.

A global fit at NNLO+NNLL accuracy yielded the best fit value of

$$\alpha_S(M_Z) = 0.11750 \pm 0.00018(exp.) \pm 0.00102(hadr.) \pm 0.00257(ren.) \pm 0.00078(res.). \tag{6.7}$$

In order to assess the effect of the NNLO correction on the extracted value of the strong coupling I also quote the fit result obtained with NLO+NNLL precision,

$$\alpha_S(M_Z) = 0.12200 \pm 0.00023(exp.) \pm 0.00113(hadr.) \pm 0.00433(ren.) \pm 0.00293(res.). \tag{6.8}$$

There are no correlations between the estimated biases, therefore, we can combine the uncertainties in quadrature. Thus for the NNLO+NNLL we get,

$$\alpha_S(M_Z) = 0.11750 \pm 0.00287, \tag{6.9}$$

while the combined value of the result of the NLO+NNLL precision fit is

$$\alpha_S(M_Z) = 0.12200 \pm 0.00535. \tag{6.10}$$

The effect of the NNLO correction on the central value is moderate but not negligible, hwever, the overall uncertainty decreased roughly by a factor of two. This improvement of precision comes from the decrease in the perturbative uncertainties, which is roughly a factor of two for renormalization scale variation and a factor of three for resummation scale variation. However, the total estimated bias is still dominated by the perturbative uncertainties. The value produced by the analysis using NNLO+NNLL calculations is in agreement with the 2017 world average of $\alpha_S(M_Z) = 0.1181 \pm 0.0011$ [6, 58] and the current world average $\alpha_S(M_Z) = 0.1179 \pm 0.0010$ [1, 2] as well.

Chapter 7

Extraction of $\alpha_S(M_Z)$ from jet rates

Jet rates are known to be less affected by hadronization than event shapes [76], hence they allow for a more precise determination of the strong coupling. In addition, fully differential predictions for three-jet production in e^+e^- annihilation are available at NNLO accuracy and using the predictions for the three-jet rate at NNLO and the total cross section at N^{3}LO, the two-jet rate can be obtained at N^{3}LO accuracy.

The fixed-order calculations for jet rates break down in those parts of the phase space which are dominated by soft and collinear QCD radiation. In these regions the resolution parameter y_{cut} (defined in the following section) approaches 0 and the perturbative prediction contains logarithmic divergences in the form of $\alpha_S^n \ln^m y_{\text{cut}}$ where $m \leq 2n$. Once again, resummation of such logarithmic divergences is required to obtain physical predictions that are also valid for small values of y_{cut}. Resummation for two-jet rate is known up to NNLL accuracy.

In this chapter I present the extraction of $\alpha_S(M_Z)$ from two-jet rate at N^{3}LO+NNLL accuracy. Hadronization corrections were modelled once again using Monte Carlo event generators.

7.1 Definition of the observable

In order to classify final-state events according to jet multiplicities we need to use a so-called jet finding algorithm. In this work we used the Durham clustering algorithm [77], which sequentially combines final-state momenta. The algorithm assigns a distance in phase space to every (ij) pair of momenta according to the formula

$$y_{ij} = 2\frac{\min(E_i^2, E_j^2)}{E_{\text{vis}}^2}(1 - \cos\theta_{ij}), \tag{7.1}$$

where θ_{ij} is the angle between the spatial components of the corresponding momenta and E_{vis} is the visible energy in the event. If the smallest of these y_{ij} distances y_{min} is below a predefined limit y_{cut}, the corresponding pair is combined into a single momentum. We adopted the E-scheme [77], which means that the momenta are combined by simple addition. The algorithm proceeds with the combination until all remaining distances become larger than y_{cut}.

The n-jet rate is then defined as

$$R_n(y_{\text{cut}}) = \frac{\sigma_{\text{n-jet}}(y_{\text{cut}})}{\sigma_t}, \tag{7.2}$$

with $\sigma_{\text{n-jet}}(y_{\text{cut}})$ being the cross section for n-jet production in hadronic final states obtained using Durham clustering and σ_t is the total hadronic cross section. It is easy to see from Eq. (7.2) that

$$\sum_n R_n = 1. \tag{7.3}$$

Fig. 7.1 shows n-jet rates for $n = 1, 2, 3, 4, 5$ and $n \geq 6$ as functions of y_{cut} measured by the ALEPH Collaboration [78]. For large values of y_{cut}, the two-jet rate dominates but as we decrease the resolution parameter, hadrons will be clustered into more jets, making three-, four- and eventually five-jet rates more significant. At the finest resolution, the n-jet rate for $n \geq 6$ becomes dominant.

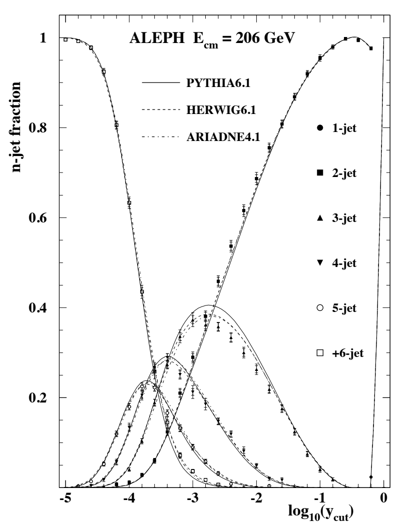

Figure 7.1: Jet rates measured by the ALEPH Collaboration [78] and the prediction of Monte Carlo models.

7.2 Perturbative calculations

Fixed-order predictions for jet rates were obtained, once again, using the CoLoRFulNNLO method. The expansion of the n-jet rate R_n in α_S as a function of y_{cut} at the default scale Q is

$$R_n(y_{\text{cut}}) = \delta_{2,n} + \frac{\alpha_S(Q)}{2\pi} A_n(y_{\text{cut}}) + \left(\frac{\alpha_S(Q)}{2\pi}\right)^2 B_n(y_{\text{cut}}) + \left(\frac{\alpha_S(Q)}{2\pi}\right)^3 C_n(y_{\text{cut}}) + \mathcal{O}(\alpha_S^4), \tag{7.4}$$

where A, B and C are the perturbative coefficients. For massless quarks, these coefficients are independent of Q. The renormalization scale dependence of the fixed-order distribution can be restored using the renormalization group equation for α_S (see Eq. (2.9)) and we find

$$\begin{aligned} R_n(y_{\text{cut}}, \mu_R) =& \delta_{2,n} + \frac{\alpha_S(\mu_R)}{2\pi} A_n(y_{\text{cut}}, x_R) + \left(\frac{\alpha_S(\mu_R)}{2\pi}\right)^2 B_n(y_{\text{cut}}, x_R) \\ &+ \left(\frac{\alpha_S(Q)}{2\pi}\right)^3 C_n(y_{\text{cut}}, x_R) + \mathcal{O}(\alpha_S^4), \end{aligned} \tag{7.5}$$

where

$$\begin{aligned} A_n(y_{\text{cut}}, x_R) =& A_n(y_{\text{cut}}), \\ B_n(y_{\text{cut}}, x_R) =& B_n(y_{\text{cut}}) + \frac{1}{2}\beta_0 \ln(x_R^2)\, A_n(y_{\text{cut}}), \\ C_n(y_{\text{cut}}, x_R) =& C_n(y_{\text{cut}}) + \beta_0 \ln(x_R^2)\, B_n(y_{\text{cut}}) + \left(\frac{1}{4}\beta_1 \ln(x_R^2) + \frac{1}{4}\beta_0^2 \ln^2(x_R^2)\right) A_n(y_{\text{cut}}). \end{aligned} \tag{7.6}$$

Fixed-order predictions of n-jet rates for $n = 2, 3, 4, 5$ can be seen in Fig. 7.2 along with renormalization scale variation in the range of $x_R \in [1/2, 2]$.

For the two-jet rate R_2 resummation was performed with the `ARES` program [79] and the matching to the fixed-order prediction was done according to the log-R scheme [80]. The resummation technique used here was formulated in [36, 79, 81].

The resummation of the three-jet rate R_3 is much more involved than in the two-jet case due to the extra number of emitting particles. Accordingly, the state-of-the-art resummed predictions have a much lower logarithmic accuracy. While R_3 is more sensitive to α_S than R_2, the low precision cannot provide a good theoretical control in the region where the logarithms of the resolution parameter y become large. Thus, for this analysis, resummation was not performed for R_3 and the fit was limited to a range where the fixed-order result is reliable.

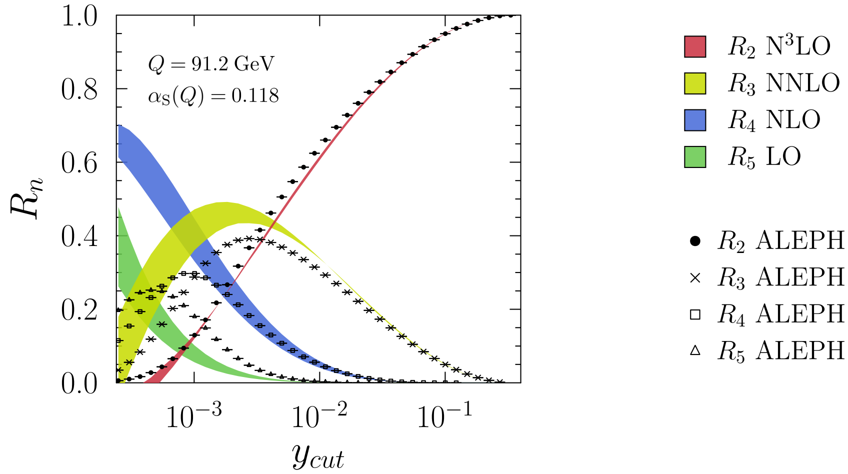

Figure 7.2: Fixed-order calculations for two-, three-, four- and five-jet rates compared to ALEPH data [78]. The bands were obtained by varying the renormalization scale x_R between 1/2 and 2.

The perturbative prediction described in this section was complemented with b-quark mass corrections. Mass effects were included according to the formule,

$$R_2(y_{\rm cut}) = (1 - r_b(Q))R_2^{N^3LO+NNLL}(y_{\rm cut})_{massless} + r_b(Q)R_2^{NNLO}(y_{\rm cut})_{massive},$$
$$R_3(y_{\rm cut}) = (1 - r_b(Q))R_3^{NNLO+NNLL}(y_{\rm cut})_{massless} + r_b(Q)R_3^{NLO}(y_{\rm cut})_{massive}. \quad (7.7)$$

The massive contributions were obtained by combining the total cross section at NNLO including mass corrections as obtained from Ref. [75] and the $\mathcal{O}(\alpha_S^2)$ three- and four-jet rate predictions as computed with the `Zbb4` program.

The fraction of b-quark events $r_b(Q)$ was computed as it is described by Eq. (6.2) in Chapter 6. For the b-quark mass we used $m_b = 4.78\,\text{GeV}$ which is consistent with the corresponding world average [1].

7.3 Hadronization corrections and extraction of α_S

In order to extract the value of the strong coupling the complete perturbative predictions described in the previous sections were compared to experimental data, taking non-perturbative effects into account using Monte Carlo models. Information on the data sets selected for extraction is summarized in Tab. 7.1.

Similarly to the analysis performed on energy-energy correlation, non-perturbative effects were modelled by state-of-the-art particle-level Monte Carlo event genera-

Experiment	Data $\sqrt{s}$, GeV	MC $\sqrt{s}$, GeV	Events
OPAL [82]	91.2(91.2)	91.2	1508031
OPAL [82]	189.0(189.0)	189	3300
OPAL [82]	183.0(183.0)	183	1082
OPAL [82]	172.0(172.0)	172	224
OPAL [82]	161.0(161.0)	161	281
OPAL [82]	130.0 – 136.0(133.0)	133	630
L3 [83]	201.5 – 209.1(206.2)	206	4146
L3 [83]	199.2 – 203.8(200.2)	200	2456
L3 [83]	191.4 – 196.0(194.4)	194	2403
L3 [83]	188.4 – 189.9(188.6)	189	4479
L3 [83]	180.8 – 184.2(182.8)	183	1500
L3 [83]	161.2 – 164.7(161.3)	161	424
L3 [83]	135.9 – 140.1(136.1)	136	414
L3 [83]	129.9 – 130.4(130.1)	130	556
JADE [82]	43.4 – 44.3(43.7)	44	4110
JADE [82]	34.5 – 35.5(34.9)	35	29514
ALEPH [78]	91.2(91.2)	91.2	3600000
ALEPH [78]	206.0(206.0)	206	3578
ALEPH [78]	189.0(189.0)	189	3578
ALEPH [78]	183.0(183.0)	183	1319
ALEPH [78]	172.0(172.0)	172	257
ALEPH [78]	161.0(161.0)	161	319
ALEPH [78]	133.0(133.0)	133	806

Table 7.1: Data used for the extraction of α_S from jet rates. The ranges of collision energies, their weighted average value (in brackets) and the number of events for each experiment are given as quoted in the original publications.

tors. As before, the hadronization corrections were estimated by comparing jet rate distributions at parton and hadron level in the simulated samples. We used the `Herwig7.1.4` event generator [70] to obtain our final results and the `Sherpa2.2.6` [69] event generator for cross-checks. In order to test hadronization model dependence, the events generated by `Herwig7.1.4` were hadronized using either the cluster model or the Lund string model. These setups are denoted by H^C and H^L respectively.

Monte Carlo generators have already been used to take hadronization effects into account in previous analyses of e^+e^- annihilation [71, 84]. Typically, hadron-level predictions were obtained by multiplying perturbative calculations by factors derived from the analysis of Monte-Carlo-generated samples described previously in Chapter 6. In this analysis, this procedure was modified to take into account constraints on R_n, specificaly that jet rates are positive and their sum is unity. These constraints were implemented by the introduction of variables ξ_1 and ξ_2 such that at parton level

$$R_2^{(p)} = \cos^2\xi_1, \qquad R_3^{(p)} = \sin^2\xi_1\,\cos^2\xi_2, \qquad R_{\geq 4}^{(p)} = \sin^2\xi_1\,\sin^2\xi_2 \tag{7.8}$$

which satisfies the constraint

$$R_2^{(p)} + R_3^{(p)} + R_{\geq 4}^{(p)} = 1. \tag{7.9}$$

The corresponding relations at hadron level are

$$\begin{aligned} &R_2^{(h)} = \cos^2(\xi_1+\delta\xi_1), \qquad R_3^{(h)} = \sin^2(\xi_1+\delta\xi_1)\,\cos^2(\xi_2+\delta\xi_2),\\ &R_{\geq 4}^{(h)} = \sin^2(\xi_1+\delta\xi_1)\,\sin^2(\xi_2+\delta\xi_2). \end{aligned} \tag{7.10}$$

The functions $\delta\xi_1(y)$ and $\delta\xi_2(y)$ account for non-perturbative effects and were obtained numerically using the Monte-Carlo-simulated samples. For a given y bin $\xi_1(y)$ and $\xi_2(y)$ were extracted from the parton-level two-jet and three-jet rates and the shifts $\delta\xi_1(y)$ and $\delta\xi_2(y)$ were obtained the same way from the hadron-level results. Samples of the obtained hadronization corrections are shown in Fig. 7.3. Plots showing the distributions of $\delta\xi_1$ and $\delta\xi_2$ that were used to produce hadronization corrections according to Eqs. (7.8) and (7.10) can be found in Appendix B. We observed that hadronization corrections increase at small values of the two- and three-jet rates, as expected, and the corrections become less significant at higher center-of-mass energies.

7.4 Phenomenological results

In Ref. [85] we presented the extraction of α_S from jet rates. Our primary result is based on the N^{3}LO+NNLL accurate predictions for two-jet rate. To find the optimal

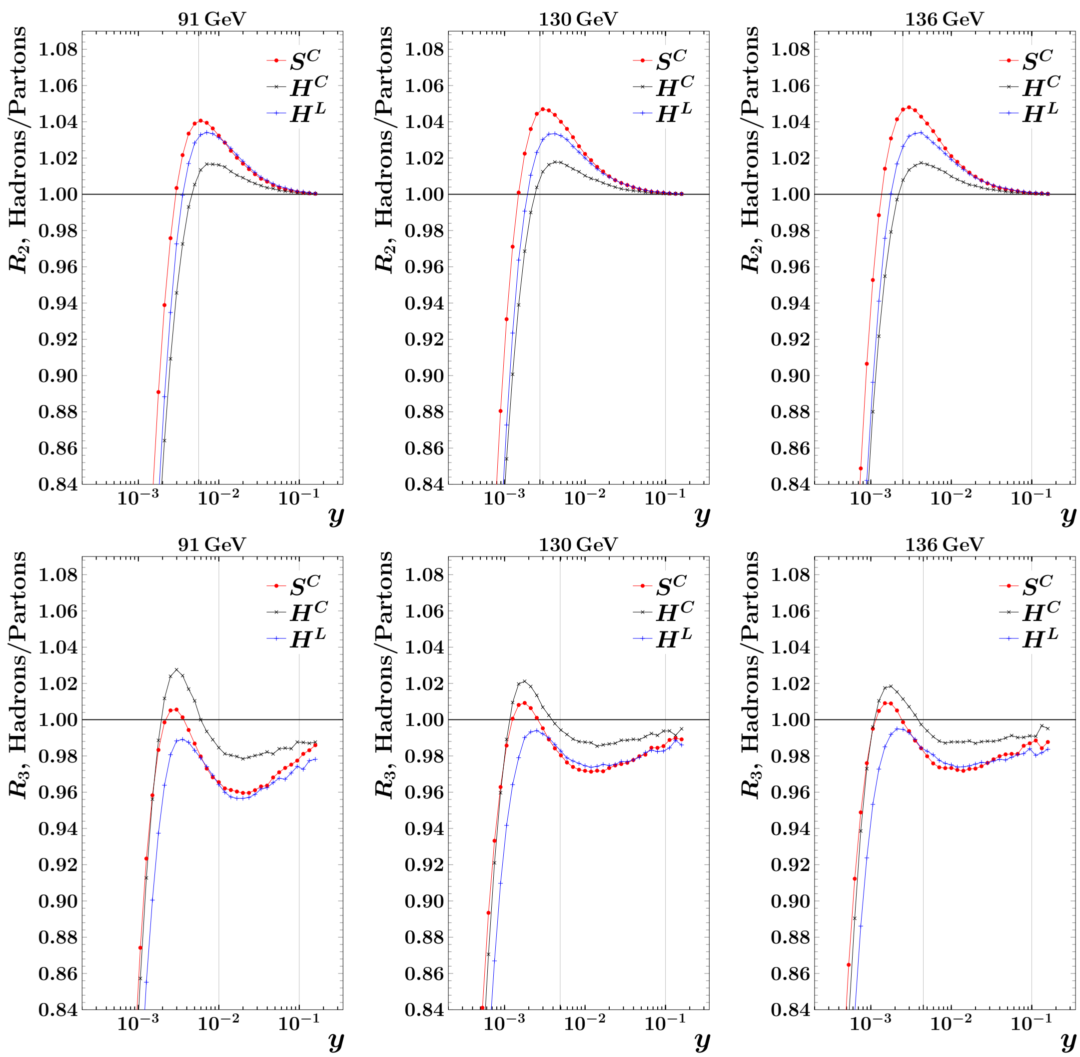

Figure 7.3: Hadronization corrections for R_2 and R_3 obtained with different Monte Carlo event simulations. The used fit range is indicated with vertical lines.

value of $\alpha_S(M_Z)$, we performed a fit based on the χ^2 method as described in section 6.3, using the `MINUIT2` program.

In order to assure that the implementation of hadronization corrections satisfies the constraint in Eq. (7.9) we set the upper bound of the fit range below the kinematical limit for four-jet production $\log_{10}(y) = \log_{10}(1/6) \approx -0.8$. Therefore, we chose $\log_{10}(y) = -1$ as the upper bound. Moreover, we adapt the lower bound to the center-of-mass energy in order to take into account that hadronization corrections become more prominent at low energies. Accordingly, we fix the lower bound $\log_{10}(y_{\min}(Q))$ of the fit range as $\log_{10}(y_{\min}(Q)) = \log_{10}(y_{\min}(M_Z)) + \mathcal{L}$ with $\mathcal{L} = \log_{10}(M_Z^2/Q^2)$.

The results of the fit at N^{3}LO and N^{3}LO+NNLL are shown in Tab. 7.2 with different hadronization schemes. As our reference fit we chose the result obtained with the H_L hadronization model in the range $[-2.25 + \mathcal{L}, -1]$,

$$\alpha_S(M_Z) = 0.11881 \pm 0.00063(\text{exp.}) \pm 0.00101(\text{hadr.}) \pm 0.00045(\text{ren.}) \pm 0.00034(\text{res.})\,. \tag{7.11}$$

Comparison of data at different energies with theoretical predictions using $\alpha_S(M_Z)$ obtained from our global fit as written in Eq. (7.11) is shown in Fig. 7.5.

Uncertainties were estimated similarly to the case of the analysis based on energy-energy correlation; they come from the χ^2+1 criterion as computed by `MINUIT2` (*exp.*), variation of renormalization scale (*ren.*), variation of resummation scale (*res.*) and choice of hadronization model (*hadr.*). The bias due to the choice of hadronization model is analysed based on the difference between the H^L and H^C setups. The dependence of the fit results on the renormalization and resummation scales for the various Monte Carlo setups is shown in Fig. 7.4. In particular, the systematic uncertainty was computed as half of the difference between the $\alpha_S(M_Z)$ results obtained with the H^L and H^C setups.

The value of $\alpha_S(M_Z)$ extracted using N^{3}LO+NNLL predictions for $\mathcal{R}_2$ with combined uncertainties is

$$\alpha_S(M_Z) = 0.11881 \pm 0.00131 \tag{7.12}$$

which is in agreement with the world average as of 2019 ($\alpha_S(M_Z) = 0.1179 \pm 0.0010$ [1, 2]), although it is noticeably lower than the results from other measurements performed for e^+e^- observables using NNLO fixed-order calculations and Monte Carlo hadronization models. The uncertainties are approximately of the same sizes.

Fit ranges, $\log_{10}(y)$ Hadronization	N^{3}LO $\chi^2/d.o.f.$	N^{3}LO+NNLL $\chi^2/d.o.f.$
$[-1.75+\mathcal{L},-1]$ S^C	0.12121 ± 0.00095 $20/86 = 0.24$	0.11849 ± 0.00092 $20/86 = 0.24$
$[-2+\mathcal{L},-1]$ S^C	0.12114 ± 0.00081 $26/100 = 0.26$	0.11864 ± 0.00075 $26/100 = 0.26$
$[-2.25+\mathcal{L},-1]$ S^C	0.12119 ± 0.00060 $44/150 = 0.29$	0.11916 ± 0.00063 $44/150 = 0.29$
$[-2.5+\mathcal{L},-1]$ S^C	0.12217 ± 0.00052 $89/180 = 0.50$	0.12075 ± 0.00055 $107/180 = 0.59$
$[-1.75+\mathcal{L},-1]$ H^C	0.11957 ± 0.00098 $22/86 = 0.26$	0.11698 ± 0.00093 $22/86 = 0.25$
$[-2+\mathcal{L},-1]$ H^C	0.11923 ± 0.00079 $29/100 = 0.29$	0.11687 ± 0.00076 $28/100 = 0.28$
$[-2.25+\mathcal{L},-1]$ H^C	0.11868 ± 0.00068 $43/150 = 0.28$	0.11679 ± 0.00064 $40/150 = 0.27$
$[-2.5+\mathcal{L},-1]$ H^C	0.11849 ± 0.00050 $58/180 = 0.32$	0.11723 ± 0.00053 $58/180 = 0.32$
$[-1.75+\mathcal{L},-1]$ H^L	0.12171 ± 0.00109 $21/86 = 0.25$	0.11897 ± 0.00092 $21/86 = 0.24$
$[-2+\mathcal{L},-1]$ H^L	0.12144 ± 0.00078 $28/100 = 0.28$	0.11893 ± 0.00075 $26/100 = 0.26$
$[-2.25+\mathcal{L},-1]$ H^L	0.12080 ± 0.00069 $43/150 = 0.28$	0.11881 ± 0.00063 $39/150 = 0.26$
$[-2.5+\mathcal{L},-1]$ H^L	0.12024 ± 0.00051 $57/180 = 0.32$	0.11897 ± 0.00053 $52/180 = 0.29$

Table 7.2: Fit of $\alpha_s(M_Z)$ from experimental data for R_2 obtained using N^{3}LO and N^{3}LO+NNLL predictions, three different hadronization models and four different choices of the fit range, as given in the brackets, with $\mathcal{L} = \log_{10}(M_Z^2/Q^2)$. The reported uncertainty is the fit uncertainty as given by `MINUIT2`. Once again, $d.o.f.$ stands for degrees of freedom obtained as #(data points) − #(parameters) − 1.

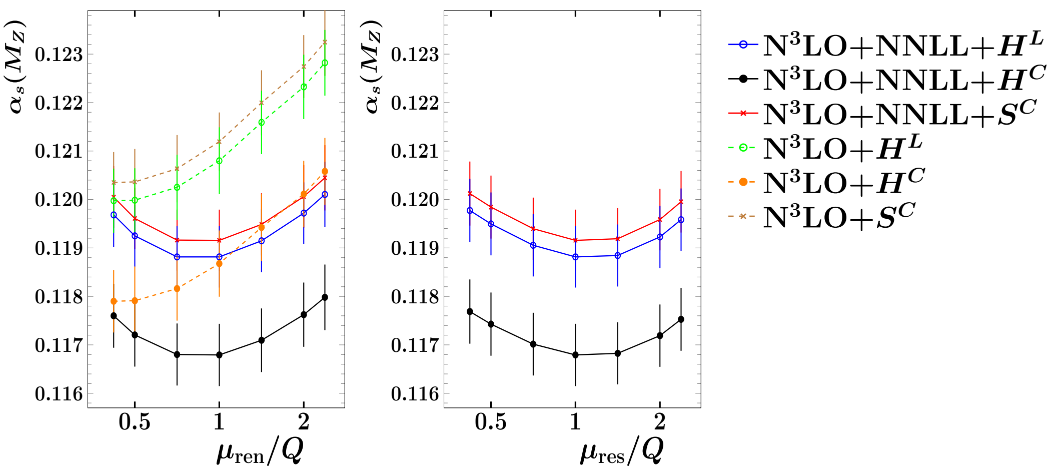

Figure 7.4: Dependence of (R_2) fit results on the renormalization and resummation scales. The fit range for S^C, H^C and H^L setups is $[-2.25 + \mathcal{L}, -1]$ with $\mathcal{L} = \log_{10}(M_Z^2/Q^2)$.

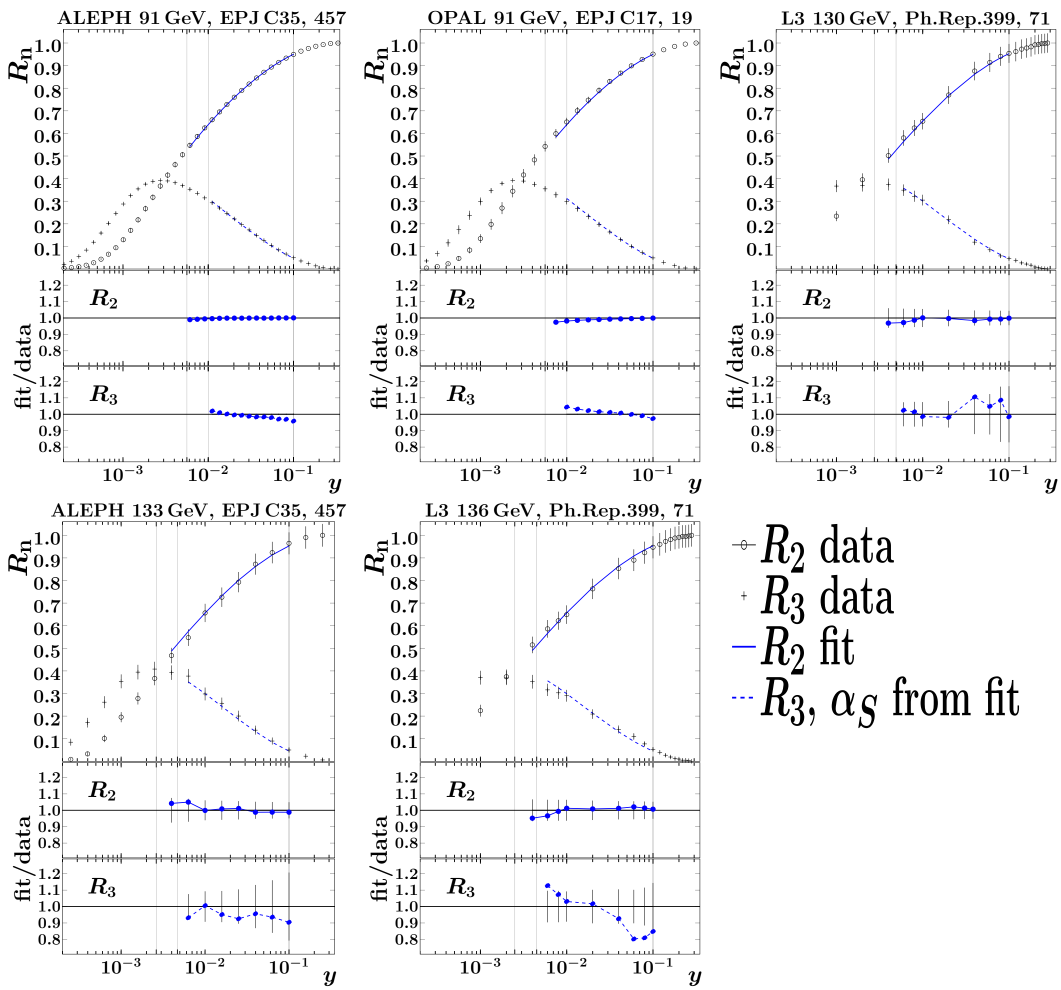

Figure 7.5: Comparison of data and perturbative predictions supplemented by hadronization corrections in the H^L model using for the strong coupling the value obtained from our global fit, eq. (7.11).

Part III

Subtractions with hadronic initial states

Chapter 8

Extending the CoLoRFulNNLO scheme

In the following sections, the extension of the CoLoRFulNNLO subtraciton scheme will be presented on the example of the double real contribution of the Drell-Yan process, that is, vector boson production in proton-proton collisions. I define the necessary counterterms with suitable parametrization to cancel all kinematic singularities of the $n+2$-particle squared matrix element and show that the regularized expression is free of non-integrable divergences. I also briefly discuss the analytic integration of the obtained counterterms which is needed to regularize the loop corrections.

8.1 Structure of the regularized double real emissions

The construction of subtractions follows along the lines of Section 3.3 with the definitions of the approximate cross sections in Eqs. (3.36), (3.38) and (3.39) left unchanged. The definition of operators $\mathcal{A}_1$, $\mathcal{A}_2$ and $\mathcal{A}_{12}$, however, need to be extended to take into account the singularities related to partons emitted by the colored initial-state particles. Furthermore, the NNLO correction contains additional singular terms $\mathrm{d}\sigma_{n+1}^{C_1}$ and $\mathrm{d}\sigma_n^{C_2}$ that are needed for *pdf* renormalization, see Eq. 3.1. With this modification the NNLO cross section becomes

$$\sigma^{NNLO}[J] = \int_{n+2} \mathrm{d}\sigma_{n+2}^{RR} J_{n+2} + \int_{n+1} \mathrm{d}\sigma_{n+1}^{RV} J_{n+1} + \int_n \mathrm{d}\sigma_n^{VV} J_n + \int_{n+1} \mathrm{d}\sigma_{n+1}^{C_1} J_{n+1} + \int_n \mathrm{d}\sigma_n^{C_2} J_n. \tag{8.1}$$

This expression must be rearranged following the method outlined in Section 3.3 and it will be cast in the form

$$\sigma^{NNLO}[J] = \int_{n+2} \mathrm{d}\sigma^{NNLO}_{n+2} + \int_{n+1} \mathrm{d}\sigma^{NNLO}_{n+1} + \int_{n} \mathrm{d}\sigma^{NNLO}_{n}, \tag{8.2}$$

where

$$\begin{aligned}
\mathrm{d}\sigma^{NNLO}_{n+2} &= \left\{ \mathrm{d}\sigma^{RR}_{n+2} J_{n+2} - \mathrm{d}\sigma^{RR,A_2}_{n+2} J_n - \left[\mathrm{d}\sigma^{RR,A_1}_{n+2} J_{n+1} - \mathrm{d}\sigma^{RR,A_{12}}_{n+2} J_n \right] \right\}_{D=4}, \\
\mathrm{d}\sigma^{NNLO}_{n+1} &= \left\{ \left[\mathrm{d}\sigma^{RV}_{n+1} + \mathrm{d}\sigma^{C_1}_{n+1} + \int_1 \mathrm{d}\sigma^{RR,A_1}_{n+2} \right] J_{n+1} \right. \\
&\quad \left. - \left[\mathrm{d}\sigma^{RV,A_1}_{n+1} + \mathrm{d}\sigma^{C_1,A_1}_{n+1} + \left(\int_1 \mathrm{d}\sigma^{RR,A_1}_{n+2} \right)^{A_1} \right] J_n \right\}_{D=4}, \\
\mathrm{d}\sigma^{NNLO}_{n} &= \left\{ \mathrm{d}\sigma^{VV}_{n} + \mathrm{d}\sigma^{C_2}_{n} + \int_2 \left[\mathrm{d}\sigma^{RR,A_2}_{n+2} - \mathrm{d}\sigma^{RR,A_{12}}_{n+2} \right] \right. \\
&\quad \left. + \int_1 \left[\mathrm{d}\sigma^{RV,A_1}_{n+1} + \mathrm{d}\sigma^{C_1,A_1}_{n+1} + \left(\mathrm{d}\sigma^{RR,A_1}_{n+2} \right)^{A_1} \right] \right\}_{D=4} J_n.
\end{aligned} \tag{8.3}$$

In this part of the dissertation I focus on the double real contribution $\mathrm{d}\sigma^{RR}_{n+2}$ which must be regularized by subtraction as shown in section 3.3. The approximate squared matrix element defined in Eq. (3.38) is extended as

$$\mathcal{A}_1 |\mathcal{M}^{(0)}_{n+2}|^2 = \sum_{r\in F} \left[\mathcal{S}^{(0)}_r + \sum_{i\in F} \left(\frac{1}{2}\mathcal{C}^{(0),FF}_{ir} - \mathcal{C}^{FF}_{ir}\mathcal{S}^{(0)}_r \right) + \sum_{a\in I} \left(\mathcal{C}^{(0),IF}_{ar} - \mathcal{C}^{IF}_{ar}\mathcal{S}^{(0)}_r \right) \right]. \tag{8.4}$$

We have modified the notation that was used previously in order to clarify whether an index stands for an initial- (I) or a final-state (F) parton. In the case of soft counterterms such indices are not added since only final-state partons can become soft.

The approximate squared matrix element in Eq. (3.36) is extended as

$$\begin{aligned}
\mathcal{A}_2 |\mathcal{M}^{(0)}_{n+2}|^2 = \sum_{r\in F} \sum_{\substack{s\in F \\ r\neq s}} \Bigg\{ & \frac{1}{2}\mathcal{S}^{(0)}_{rs} \\
+ \sum_{\substack{i\in F \\ i\neq r,s}} \Bigg[& \frac{1}{6}\mathcal{C}^{(0),FFF}_{irs} + \frac{1}{2}\mathcal{CS}^{(0),FF}_{ir,s} - \frac{1}{2}\mathcal{C}^{FFF}_{irs}\mathcal{CS}^{(0),FF}_{ir,s} - \frac{1}{2}\mathcal{C}^{FFF}_{irs}\mathcal{S}^{(0)}_{rs} - \mathcal{CS}^{FF}_{ir,s}\mathcal{S}^{(0)}_{rs}
\end{aligned}$$

$$
\begin{aligned}
&+ \mathcal{C}_{irs}^{FFF} \mathcal{CS}_{ir,s}^{FF} \mathcal{S}_{rs}^{(0)} + \sum_{\substack{j\in F\\ j\neq i,r,s}} \left(\frac{1}{8}\mathcal{C}_{ir,js}^{(0),FF,FF} - \frac{1}{2}\mathcal{C}_{ir,js}^{FF,FF} \mathcal{CS}_{ir,s}^{(0),FF} + \frac{1}{2}\mathcal{C}_{ir,js}^{FF,FF} \mathcal{S}_{rs}^{(0)} \right) \Bigg] \\
+ \sum_{a\in I} \Bigg[&\frac{1}{2}\mathcal{C}_{ars}^{(0),IFF} + \mathcal{CS}_{ar,s}^{(0),IF} - \mathcal{C}_{ars}^{IFF} \mathcal{CS}_{ar,s}^{(0),IF} - \frac{1}{2}\mathcal{C}_{ars}^{IFF} \mathcal{S}_{rs}^{(0)} - \mathcal{CS}_{ar,s}^{IF} \mathcal{S}_{rs}^{(0)} \\
&+ \mathcal{C}_{ars}^{IFF} \mathcal{CS}_{ar,s}^{IF} \mathcal{S}_{rs}^{(0)} \\
&+ \sum_{\substack{j\in F\\ j\neq r,s}} \left(\frac{1}{2}\mathcal{C}_{ar,js}^{(0),IF,FF} - \frac{1}{2}\mathcal{C}_{ar,js}^{IF,FF} \mathcal{CS}_{js,r}^{(0),FF} - \frac{1}{2}\mathcal{C}_{ar,js}^{IF,FF} \mathcal{CS}_{js,r}^{(0),FF} + \mathcal{C}_{ar,js}^{IF,FF} \mathcal{S}_{rs}^{(0)} \right) \\
&+ \sum_{\substack{b\in I\\ b\neq a}} \left(\frac{1}{2}\mathcal{C}_{ar,bs}^{(0),IF,IF} - \mathcal{C}_{ar,bs}^{IF,IF} \mathcal{CS}_{ar,s}^{(0),IF} + \frac{1}{2}\mathcal{C}_{ar,bs}^{IF,IF} \mathcal{S}_{rs}^{(0)} \right) \Bigg] \Bigg\}. \qquad (8.5)
\end{aligned}
$$

The formula above was obtained by utilizing the fact that for any combination of initial- or final-state particles n and m,

$$
\mathcal{C}_{nr,ms} \mathcal{CS}_{nr,s} \mathcal{S}_{rs} = \mathcal{C}_{nr,ms} \mathcal{S}_{rs}. \qquad (8.6)
$$

Finally, the term in Eq. (3.39) necessary for avoiding double subtraction becomes

$$
\begin{aligned}
\mathcal{A}_{12} |\mathcal{M}_{n+2}^{(0)}|^2 = \sum_{t\in F} \Bigg[&\mathcal{S}_t \mathcal{A}_2 |\mathcal{M}_{n+2}^{(0)}|^2 + \sum_{\substack{k\in F\\ k\neq t}} \left(\frac{1}{2}\mathcal{C}_{kt} \mathcal{A}_2 |\mathcal{M}_{n+2}^{(0)}|^2 - \mathcal{C}_{kt} \mathcal{S}_t \mathcal{A}_2 |\mathcal{M}_{n+2}^{(0)}|^2 \right) \\
&+ \sum_{a\in I} \left(\mathcal{C}_{at} \mathcal{A}_2 |\mathcal{M}_{n+2}^{(0)}|^2 - \mathcal{C}_{at} \mathcal{S}_t \mathcal{A}_2 |\mathcal{M}_{n+2}^{(0)}|^2 \right) \Bigg], \qquad (8.7)
\end{aligned}
$$

where each element represents a sum of several terms.

8.2 Constructing the counterterms

I will illustrate the concepts behind the construction of the subtraction terms on the example of the single collinear $\mathcal{C}_{ir}^{(0),FF}$ and $\mathcal{C}_{ar}^{(0),IF}$ counterterms entering $\mathrm{d}\sigma_{n+2}^{RR,A_1}$. The final-state single collinear subtraction term for massless final-state partons i and r is

$$
\begin{aligned}
\mathcal{C}_{ir}^{(0),FF}(\{p\}_{n+2}) =& 8\pi\alpha_S \mu_R^{2\epsilon} \frac{1}{s_{ir}} \\
&\times \langle \mathcal{M}_{n+1}^{(0)}(\{\hat{p}\}_{n+1}; \hat{p}_{(ab)}) | \hat{P}_{f_i f_r}^{(0)}(z_{i,r}, z_{r,i}, k_{\perp;ir}) | \mathcal{M}_{n+1}^{(0)}(\{\hat{p}\}_{n+1}; \hat{p}_{(ab)}) \rangle, \qquad (8.8)
\end{aligned}
$$

where $s_{ir} = 2p_i \cdot p_r$. In the case of massless partons, this Lorentz-invariant quantity is just the squared sum of momenta, $s_{ir} = (p_i + p_r)^2$. The $\{\hat{p}\}_{n+1}$ set of momenta that appear in the factorized matrix elements is constructed from the original $\{p\}_{n+2}$ set using the following phase space mapping

$$\begin{aligned}
\hat{p}_a^\mu &= (1-\alpha_{ir})p_a^\mu, \\
\hat{p}_b^\mu &= (1-\alpha_{ir})p_b^\mu, \\
\hat{p}_{ir}^\mu &= (p_i^\mu + p_r^\mu) - \alpha_{ir}(p_a^\mu + p_b^\mu), \\
\hat{p}_k^\mu &= p_k^\mu, \quad k \neq i, r.
\end{aligned} \tag{8.9}$$

The value of α_{ir} is fixed by requiring the so-called parent momentum $\hat{p}_{ir}^\mu$ to be massless, $\hat{p}_{ir}^2 = 0$ and we get

$$\alpha_{ir} = \frac{1}{2}\left[\frac{s_{(ir)(ab)}}{s_{ab}} - \sqrt{\frac{s_{(ir)(ab)}^2}{s_{ab}^2} - \frac{4s_{ir}}{s_{ab}}}\right], \tag{8.10}$$

where $s_{(ir)(ab)} = 2(p_i + p_r)\cdot(p_a + p_b)$.

The momenta of the daughter partons in the $(ir) \to i{+}r$ splitting can be expressed as

$$p_i^\mu = z_{i,r}\hat{p}_{ir}^\mu + k_{\perp,ir}^\mu - \frac{k_{\perp,ir}^2}{z_{i,r}}\frac{n^\mu}{2\hat{p}_{ir}\cdot n}, \qquad p_r^\mu = z_{r,i}\hat{p}_{ir}^\mu - k_{\perp,ir}^\mu - \frac{k_{\perp,ir}^2}{z_{r,i}}\frac{n^\mu}{2\hat{p}_{ir}\cdot n}, \tag{8.11}$$

which is called the Sudakov parametrization. The momentum $\hat{p}_{ir}^\mu$ defines the collinear direction and the transverse momentum $k_{\perp,ir}^\mu$ is perpendicular to it and the gauge vector n^μ

$$k_{\perp,ir}\cdot\hat{p}_{ir} = k_{\perp,ir}\cdot n = 0. \tag{8.12}$$

The $z_{i,r}$ and $z_{r,i}$ coefficients are called momentum fractions and they satisfy the constraint

$$z_{i,r} + z_{r,i} = 1 \tag{8.13}$$

In the collinear limit $k_{\perp,ir}^\mu \to 0$ while

$$p_i^\mu \to z_{i,r}\hat{p}_{ir}^\mu, \quad p_r^\mu \to z_{r,i}\hat{p}_{ir}^\mu, \quad \text{and} \quad s_{ir} = -\frac{k_{\perp,ir}^2}{z_{i,r}z_{r,i}}, \tag{8.14}$$

but the explicit form of the transverse momentum and the momentum fractions is otherwise left unspecified by the requirement of cancellation of single collinear divergences. In order to construct a self-consistent subtraction scheme, however, the counterterms must be defined throughout the entire phase space and not just in the unresolved limit. In the CoLoRFulNNLO scheme, the momentum fractions are

$$z_{i,r} = \frac{s_{i(ab)}}{s_{(ir)(ab)}}, \qquad z_{r,i} = \frac{s_{r(ab)}}{s_{(ir)(ab)}}, \tag{8.15}$$

where $s_{i(ab)} = 2p_i \cdot (p_a + p_b)$, $s_{r(ab)} = 2p_r \cdot (p_a + p_b)$, and the transverse momentum is defined as

$$k^\mu_{\perp;ir} = \zeta_{i,r} p^\mu_r - \zeta_{r,i} p^\mu_i + Z_{ir} \hat{p}^\mu_{ir}, \tag{8.16}$$

where the newly introduced quantities are

$$\zeta_{i,r} = z_{i,r} - \frac{s_{ir}}{\alpha_{ir}\, s_{(ir)(ab)}}, \quad \zeta_{r,i} = z_{r,i} - \frac{s_{ir}}{\alpha_{ir}\, s_{(ir)(ab)}}, \quad Z_{ir} = \frac{s_{ir}}{\alpha_{ir}\, s_{\widehat{ir}(ab)}}(z_{r,i} - z_{i,r}). \tag{8.17}$$

The object $\hat{P}^{(0)}_{f_i\, f_r}(z_{i,r}, z_{r,i}, k_{\perp;ir})$ is a so-called Altarelli-Parisi splitting function which is an operator defined on the vectorspace of the spin states of the parent parton in the $(ir) \to i + r$ splitting. The lower indices f_i and f_r denote the flavors of the daughter partons, so $f_{i/r} = q, \bar{q}, g$. The function itself is parametrized by the transverse momentum $k_{\perp;ir}$ and the momentum fractions $z_{i,r}$ and $z_{r,i}$ which satisfy the constaint Eq. (8.13). Hence, the Altarelli-Parisi functions depend only on one momentum fraction,

$$\hat{P}^{(0)}_{f_i\, f_r}(z_{i,r}, z_{r,i}, k_\perp) = \hat{P}^{(0)}_{f_i\, f_r}(z_{i,r}, k_\perp) \tag{8.18}$$

In order to evaluate $\mathcal{C}^{(0),FF}_{ir}$ in Eq. (8.8) we should compute the coefficients of the abstract vector $|\mathcal{M}^{(0)}_{n+1}(\{\hat{p}\}_{n+1}; \hat{p}_{(ab)})\rangle$ in a certain basis. Since the vector is defined on the vectorspace of color and spin states, the basis of our choice (following Ref. [17]) consists of vectors of the form

$$|c_1, \ldots, c_{n+1}\rangle \otimes |s_1, \ldots, s_{n+1}\rangle, \tag{8.19}$$

where $|c_1, \ldots, c_{n+1}\rangle$ is a vector in the space of $n+1$ particle color states and $|s_1, \ldots, s_{n+1}\rangle$ is a vector in the space of $n+1$ particle spin states. The final-state splitting functions expressed in spinor basis for a quark parent and Lorentz basis for a gluon parent are

$$\begin{aligned}
\langle s|\hat{P}^{(0)}_{q\,g}(z, k_\perp)|s'\rangle &= C_F \left(\frac{1+z^2}{1-z} - \epsilon(1-z) \right) \delta_{ss'}, \\
\langle s|\hat{P}^{(0)}_{g\,q}(z, k_\perp)|s'\rangle &= C_F \left(\frac{1+(1-z)^2}{z} - \epsilon z \right) \delta_{ss'}, \\
\langle \mu|\hat{P}^{(0)}_{q\,\bar{q}}(z, k_\perp)|\nu\rangle &= T_R \left(-g^{\mu\nu} + 4z(1-z) \frac{k^\mu_\perp k^\nu_\perp}{k^2_\perp} \right), \\
\langle \mu|\hat{P}^{(0)}_{g\,g}(z, k_\perp)|\nu\rangle &= 2C_A \left[-g^{\mu\nu} \left(\frac{z}{1-z} + \frac{1-z}{z} \right) - 2(1-\epsilon) z(1-z) \frac{k^\mu_\perp k^\nu_\perp}{k^2_\perp} \right].
\end{aligned} \tag{8.20}$$

Once the final-state subtraction is specified, the initial-state subtraction can be constructed as follows. The counterterm itself for an initial-state parton a and a final-state parton r becoming collinear is

$$\begin{aligned}\mathcal{C}_{ar}^{(0),IF}(\{p\}_{n+2}) =&8\pi\alpha_S\mu_R^{2\epsilon}\frac{1}{x_{a,r}}\frac{1}{s_{ar}}\\ &\times\langle\mathcal{M}_{n+1}^{(0)}(\{\hat{p}\}_{n+1};\hat{p}_{(ab)})|\hat{P}_{f_{ar}\,f_r}^{(0)}(x_{a,r},x_{r,a},k_{\perp;r})|\mathcal{M}_{n+1}^{(0)}(\{\hat{p}\}_{n+1};\hat{p}_{(ab)})\rangle.\end{aligned} \tag{8.21}$$

The phase space mapping is defined as

$$\begin{aligned}\hat{p}_a^\mu &= \xi_a p_a^\mu,\\ \hat{p}_b^\mu &= p_b^\mu,\\ \hat{p}_k^\mu &= \Lambda(Q,\hat{Q})^\mu_\nu p_k^\nu, \quad k\neq r,\end{aligned} \tag{8.22}$$

where $\Lambda(Q,\hat{Q})$ is a proper Lorentz transformation that takes the massive momentum Q^μ into a momentum $\hat{Q}^\mu$ of the same mass. We have

$$Q^\mu = p_a^\mu + p_b^\mu - p_r^\mu \qquad \text{and} \qquad \hat{Q}^\mu = \hat{p}_a^\mu + \hat{p}_b^\mu = \xi_a p_a^\mu + p_b^\mu. \tag{8.23}$$

The value of ξ_a can be obtained by requiring $Q^2 = \hat{Q}^2$ and we get

$$\xi_a = 1 - \frac{s_{r(ab)}}{s_{a(ab)}}. \tag{8.24}$$

The Altarelli-Parisi splitting function in Eq. (8.21) can be computed from the final-state splitting function as

$$\hat{P}_{f_{ar}\,f_r}^{(0)}(x_{a,r},x_{r,a},k_\perp) = (-1)^{F(f_a)+F(f_{ar})+1}x_{a,r}\hat{P}_{f_a\,\bar{f}_r}^{(0)}(1/x_{a,r},-x_{r,a}/x_{a,r},k_\perp), \tag{8.25}$$

where $F(q) = F(\bar{q}) = 1$, $F(g) = 0$. Once again, $x_{a,r}$, $x_{r,a}$, which must satisfy the constraint $x_{a,r}+x_{r,a} = 1$, and $k_{\perp,r}$ must be specified in order to define the counterterm over the entire phase space. In the CoLoRFulNNLO scheme we use

$$x_{a,r} = \xi_a, \qquad x_{r,a} = 1-\xi_a, \qquad k_{\perp,r}^\mu = p_r^\mu - \left(\frac{s_{a(ab)}}{s_{ab}} - \frac{2s_{ar}}{s_{ab}}\right)p_a^\mu - \frac{s_{ar}}{s_{ab}}(p_a^\mu + p_b^\mu). \tag{8.26}$$

By this definition the transverse momentum is the component of p_r perpendicular to p_a and (p_a+p_b). Due to the contraint on $x_{a,r}$ and $x_{r,a}$, the initial-state splitting functions depend only on $x_{a,r}$ and the transverse momentum,

$$\hat{P}_{f_{ar}\,f_r}^{(0)}(x_{a,r},x_{r,a},k_\perp) = \hat{P}_{f_{ar}\,f_r}^{(0)}(x_{a,r},k_\perp) \tag{8.27}$$

and their explicit forms are

$$\begin{aligned}\langle s|\hat{P}_{q\,g}^{(0)}(x,k_\perp)|s'\rangle &= C_F\left(\frac{1+x^2}{1-x} - \epsilon(1-x)\right)\delta_{ss'},\\ \langle \mu|\hat{P}_{g\,q}^{(0)}(z,k_\perp)|\nu\rangle &= T_R\left(-g^{\mu\nu}x - 4\frac{1-x}{x}\frac{k_\perp^\mu k_\perp^\nu}{k_\perp^2}\right),\\ \langle s|\hat{P}_{q\,g}^{(0)}(x,k_\perp)|s'\rangle &= C_F\left(1-\epsilon-2x(1-x)\right)\delta_{ss'},\\ \langle \mu|\hat{P}_{q\,\bar{q}}^{(0)}(z,k_\perp)|\nu\rangle &= 2C_A\left[-g^{\mu\nu}\left(x(1-x)+\frac{x}{1-x}\right) - 2(1-\epsilon)\frac{1-x}{x}\frac{k_\perp^\mu k_\perp^\nu}{k_\perp^2}\right].\end{aligned} \tag{8.28}$$

Similarly to the demonstrated example, initially all counterterms are defined in their appropriate limit and these definitions must be extended over the entirety of the phase space in a way that they do not spoil the cancellation of singularities in other limits. This requires a careful choice of definitions for various parameters such as zs, xs and $k_\perp$s, as well as the momentum mappings for all terms.

8.3 Checking the regularized double real emissions

After constructing all the necessary counterterms I implemented the subtraction scheme on vector boson production in proton-proton collision which is the simplest process with partons in the initial state that allows us to test almost all subtraction terms. The subprocesses that contribute to the double real correction in case of W^+ production are

$$\begin{aligned}
u(p_1) + \bar{d}(p_2) &\to W^+(p_3) + q(p_4) + \bar{q}(p_5)\\
u(p_1) + \bar{d}(p_2) &\to W^+(p_3) + g(p_4) + g(p_5)\\
u(p_1) + g(p_2) &\to W^+(p_3) + d(p_4) + g(p_5)\\
\bar{d}(p_1) + g(p_2) &\to W^+(p_3) + \bar{u}(p_4) + g(p_5)\\
g(p_1) + g(p_2) &\to W^+(p_3) + \bar{u}(p_4) + d(p_5),
\end{aligned}$$

where q stands for a light quark of arbitrary flavor, u refers to a quark of flavor u or c and d denotes a quark of flavor d, s or b. The four-momentum of each particle is shown in parentheses. The NNLO correciton for this process has three types of single unresolved kinematical singularities:

- C_{rs}^{FF} single collinear with two final-state partons r and s becoming collinear,
- C_{ar}^{IF} single collinear with initial-state parton a and final-state parton s becoming collinear,
- S_r single soft with final-state gluon r becoming soft,

and four types of double unresolved kinematical singularities:

- C_{ars}^{IFF} triple collinear with initial-state parton a and final-state partons r and s becoming collinear,
- $C_{ar,bs}^{IF,IF}$ double collinear with two pairs of initial- and final-state partons (ar) and (bs) becoming collinear simultaneously,

- $CS^{IF}_{ar,s}$ collinear-soft with initial-state parton a and final-state parton r becoming collinear while final-state gluon s becomes soft,

- S_{rs} double soft with final-state partons r and s (either two gluons or a quark and antiquark of the same flavor) becoming soft simultaneously.

As a first test I checked if the subtraction successfully removes all non-integrable singularities pointwise in phase space. To do so I computed the ratio of the regulator and the unregularized squared matrix element,

$$\mathcal{R} = \frac{1}{|\mathcal{M}^{(0)}_{u\bar{d}\to W^+gg}|^2}\left[\mathcal{A}_1|\mathcal{M}^{(0)}_{u\bar{d}\to W^+gg}|^2 + \mathcal{A}_2|\mathcal{M}^{(0)}_{u\bar{d}\to W^+gg}|^2 - \mathcal{A}_{12}|\mathcal{M}^{(0)}_{u\bar{d}\to W^+gg}|^2\right] \quad (8.29)$$

in a series of phase space points, approaching each limit separately. The control parameter that measures the distance from an unresolved limit in phase space is determined by the dimensionless variables $y_{ij} = s_{ij}/s_{ab}$. Checks for the $u\bar{d} \to W^+gg$ subprocess are shown on Figs. 8.1-8.7. The left-hand side on every pair of figures shows the ratio of the subtraction term appropriate to each limit to the squared matrix element. On the right-hand side we can see $|1-\mathcal{R}|$, which goes to zero in each limit since the regularized quantity does not contain infrared singularities. The reason for this is simply that when the regulators match the singular structure of the squared matrix element, $\mathcal{R}$ goes to unity as we approach an unresolved limit.

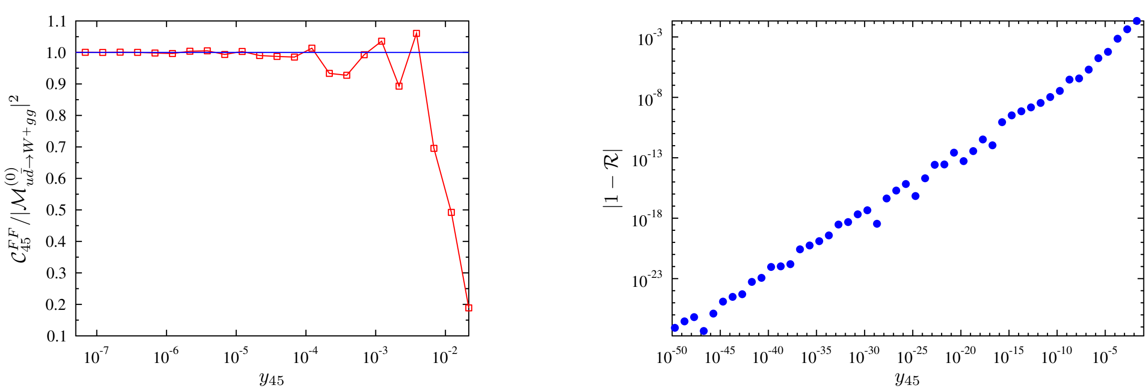

Figure 8.1: Ratio of the squared matrix element and the regulator of the double real for the $u\bar{d} \to W^+gg$ subprocess in the C^{FF}_{45} single collinear limit along with $|1-\mathcal{R}|$.

I have also plotted the ratio of subtractions to squared matrix elements in a series of randomly generated points of phase space at some fixed values of the control parameter. As we approach each limit by decreasing the value of the appropriate control parameter, we can observe on Figs. 8.8-8.14 that the generated samples agglomerate at unity. These results further ensure the correctness of the subtraction scheme,

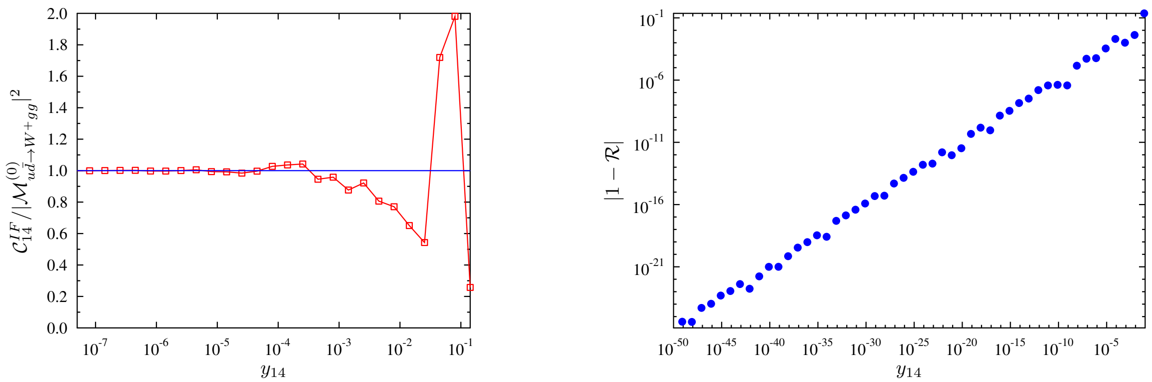

Figure 8.2: Ratio of the squared matrix element and the regulator of the double real for the $u\bar{d} \to W^+gg$ subprocess in the C_{14}^{IF} single collinear limit along with $|1-\mathcal{R}|$.

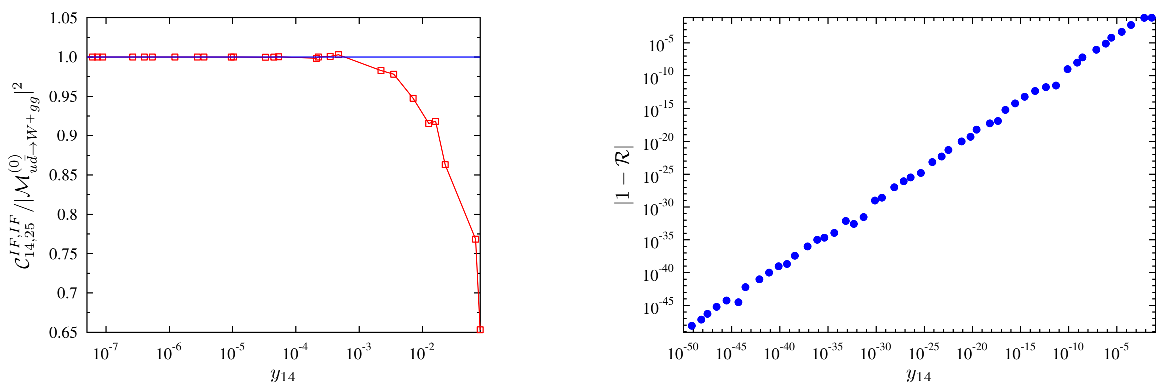

Figure 8.3: Ratio of the squared matrix element and the regulator of the double real for the $u\bar{d} \to W^+gg$ subprocess in the $C_{14,25}^{IF,IF}$ double collinear limit along with $|1-\mathcal{R}|$.

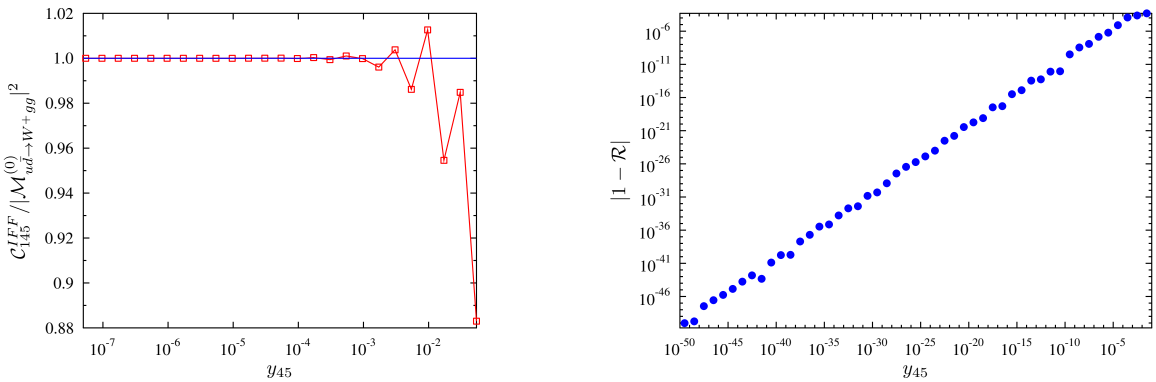

Figure 8.4: Ratio of the squared matrix element and the regulator of the double real for the $u\bar{d} \to W^+gg$ subprocess in the C_{145}^{IFF} triple collinear limit along with $|1-\mathcal{R}|$.

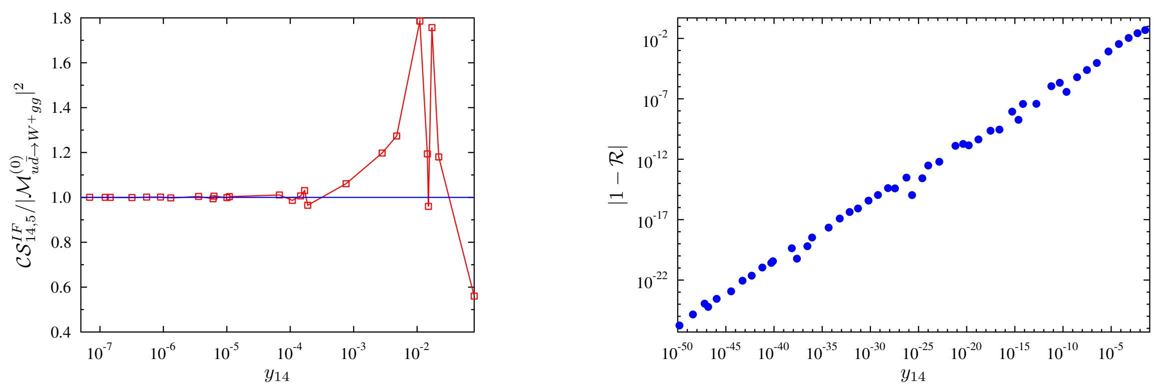

Figure 8.5: Ratio of the squared matrix element and the regulator of the double real for the $u\bar{d} \to W^+gg$ subprocess in the $CS_{14,5}^{IF}$ collinear-soft limit along with $|1-\mathcal{R}|$.

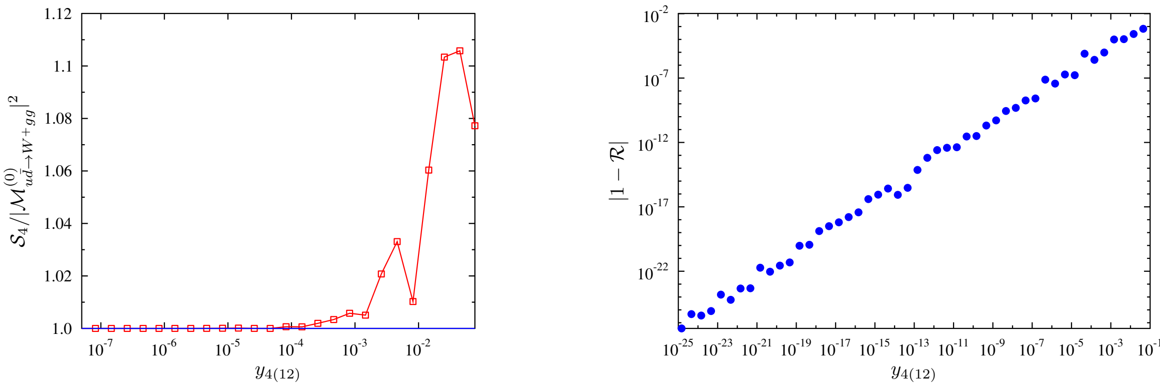

Figure 8.6: Ratio of the squared matrix element and the regulator of the double real for the $u\bar{d} \to W^+gg$ subprocess in the S_4 single soft limit along with $|1-\mathcal{R}|$.

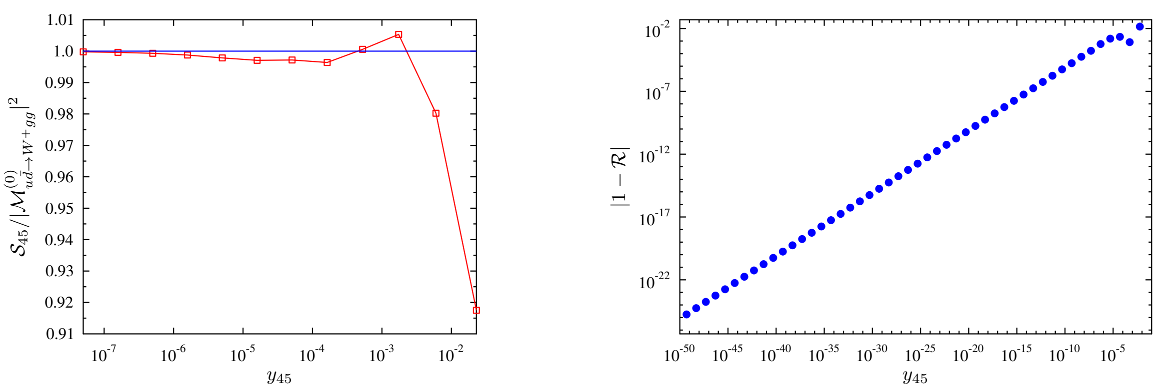

Figure 8.7: Ratio of the squared matrix element and the regulator of the double real for the $u\bar{d} \to W^+gg$ subprocess in the S_{45} double soft limit along with $|1-\mathcal{R}|$.

however, one last check must be performed to verify that the regularized double real contribution is indeed finite. Namely, the double real term must be integrated over the $n+2$ particle phase space. This step is necessary since some parametrizations of the counterterms give rise to spurious singularities in the bulk of the phase space and such errors must be ruled out.

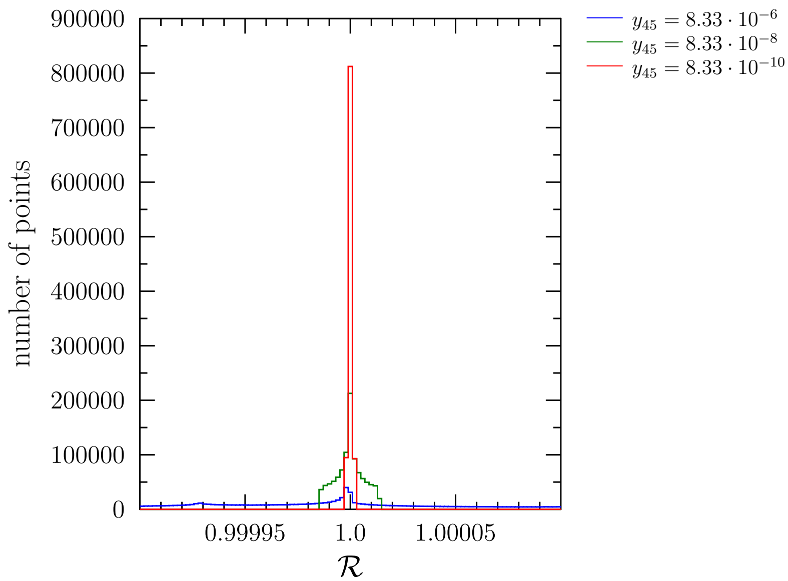

Figure 8.8: Ratio of the squared matrix element and the regulator of the double real for the $u\bar{d} \to W^+gg$ subprocess in the C_{45} single collinear limit.

In order to investigate the finiteness of the integrated double real term, we limit the domain of integration such that every $y_{ij} \geq y_{min}$ and perform he integration for different values of y_{min}. Without the presence of non-integrable singularities in the cross section, as the value of y_{min} decreases the integrated double real contribution goes to a fixed value, the true value of the integral. This saturation is shown on Fig. 8.15 for W^- production. I note that in any numerical computation there is a technical cut on the phase space due to the finite precision of numbers in computer arithmetics. This leads to the existence of a lower limit for every y_{ij}, hence this last step must be performed to show our results are numerically stable.

8.4 Outlook

At this point all possible subtraciton terms of the CoLoRFulNNLO scheme are defined and parametrized in a consistent way. Our checks show that the derived approximate squared matrix elements possess the necessary pole structure to cancel the

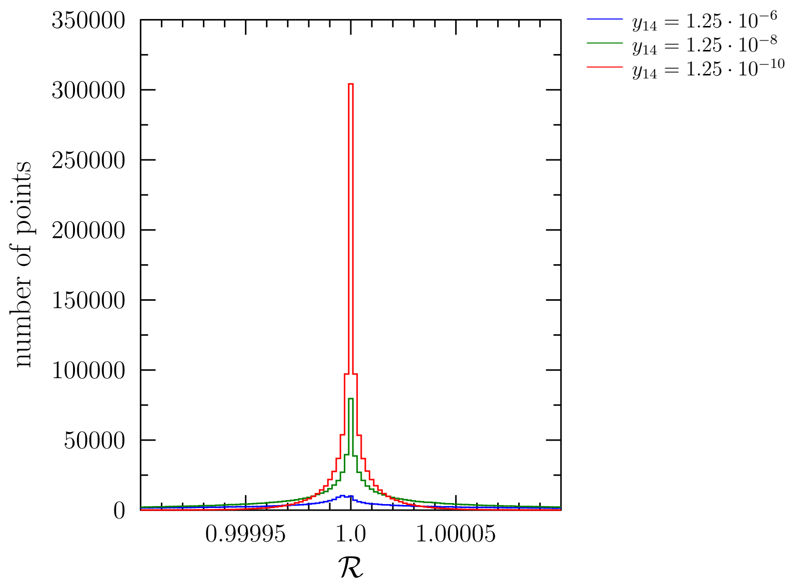

Figure 8.9: Ratio of the squared matrix element and the regulator of the double real for the $u\bar{d} \to W^+gg$ subprocess in the C_{14} single collinear limit.

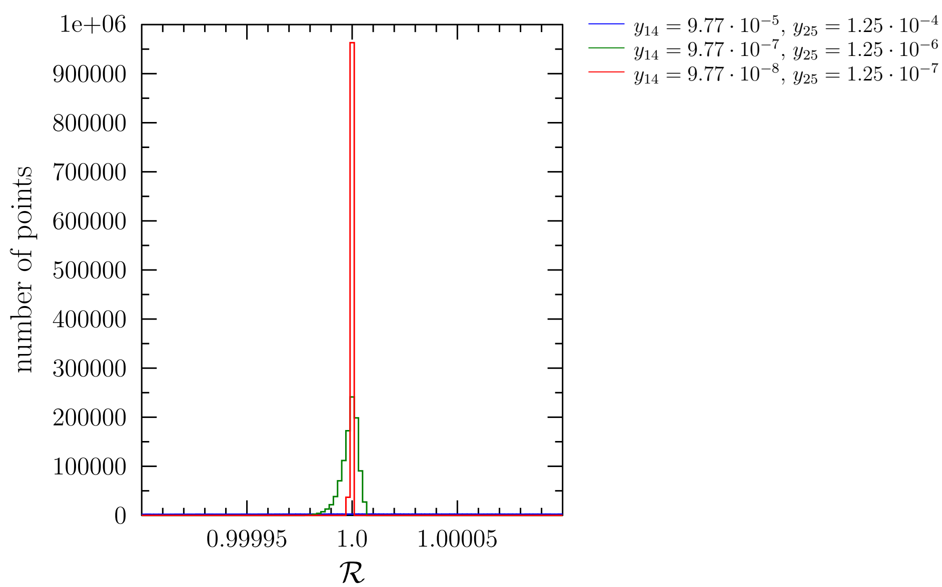

Figure 8.10: Ratio of the squared matrix element and the regulator of the double real for the $u\bar{d} \to W^+gg$ subprocess in the $C_{14,25}$ double collinear limit.

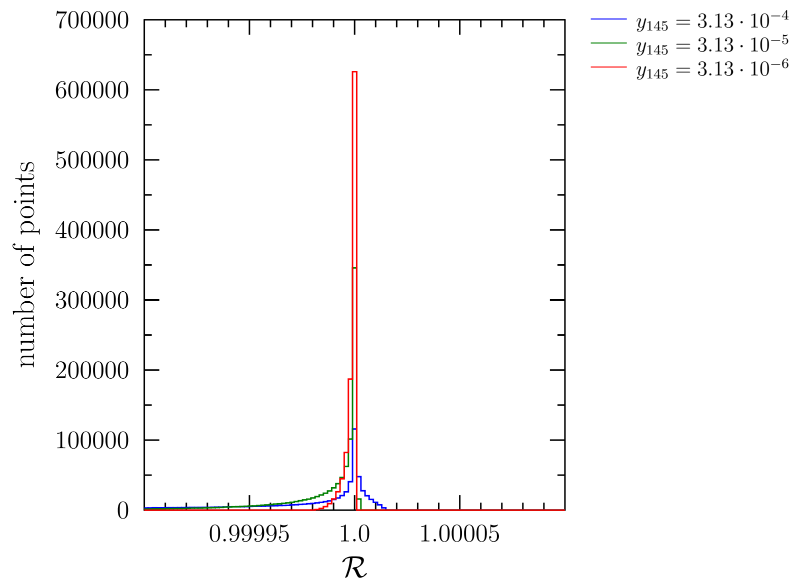

Figure 8.11: Ratio of the squared matrix element and the regulator of the double real for the $u\bar{d} \to W^+gg$ subprocess in the C_{145} triple collinear limit.

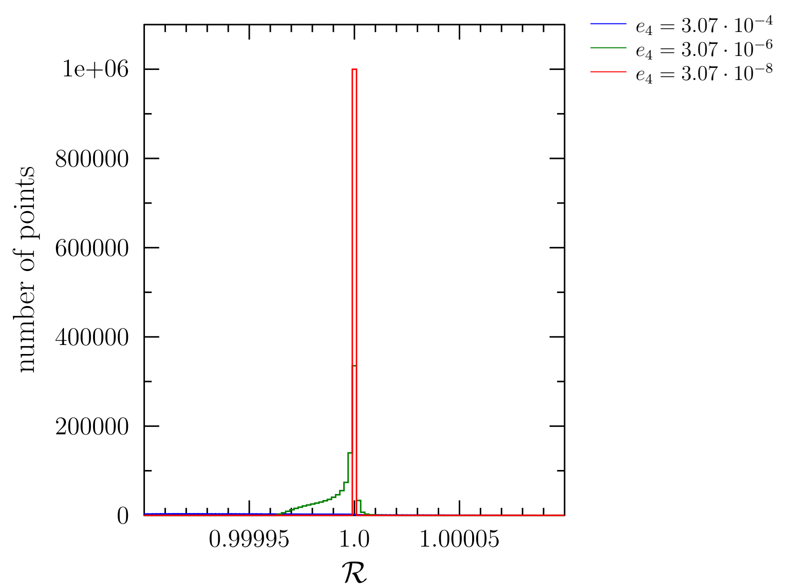

Figure 8.12: Ratio of the squared matrix element and the regulator of the double real for the $u\bar{d} \to W^+gg$ subprocess in the S_4 single soft limit.

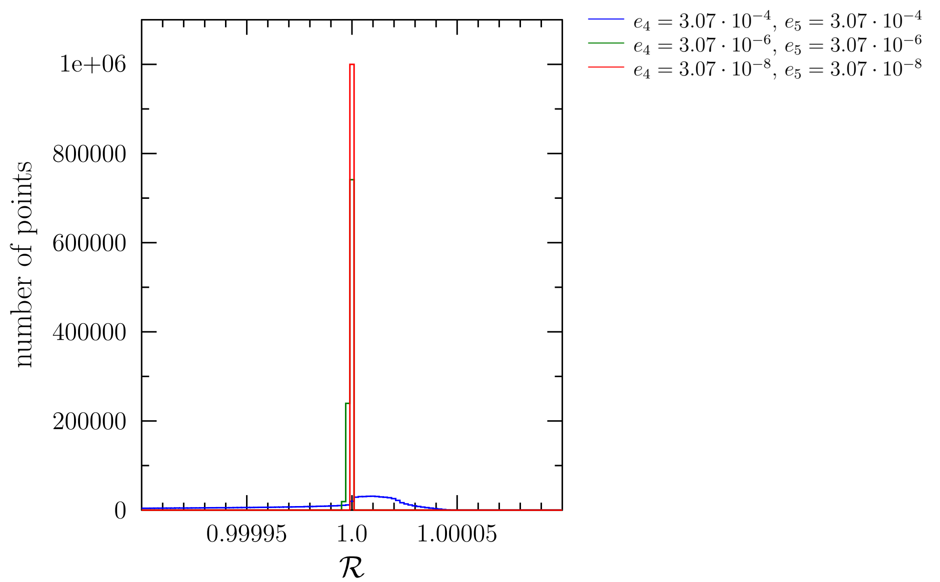

Figure 8.13: Ratio of the squared matrix element and the regulator of the double real for the $u\bar{d} \to W^+gg$ subprocess in the S_{45} double soft limit.

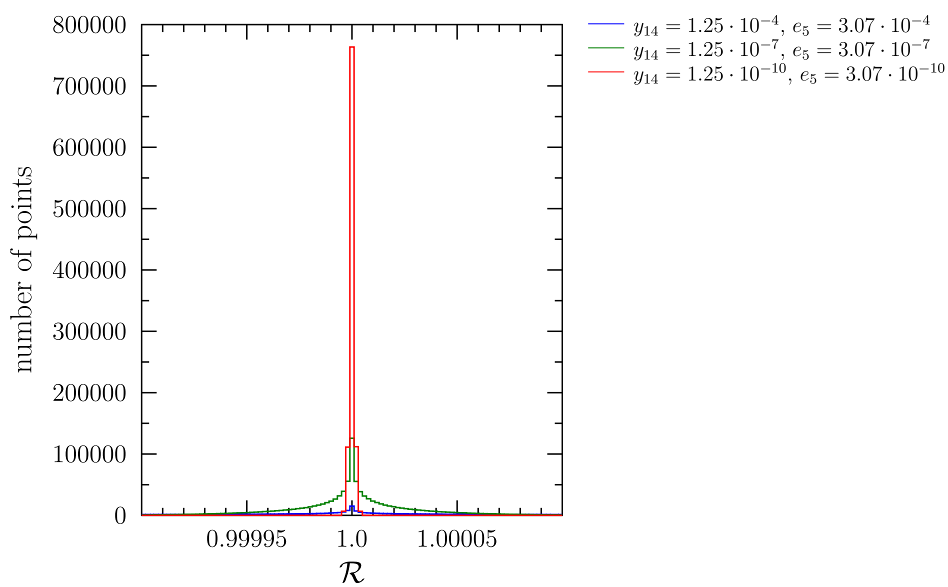

Figure 8.14: Ratio of the squared matrix element and the regulator of the double real for the $u\bar{d} \to W^+gg$ subprocess in the $CS_{14,5}$ collinear-soft limit.

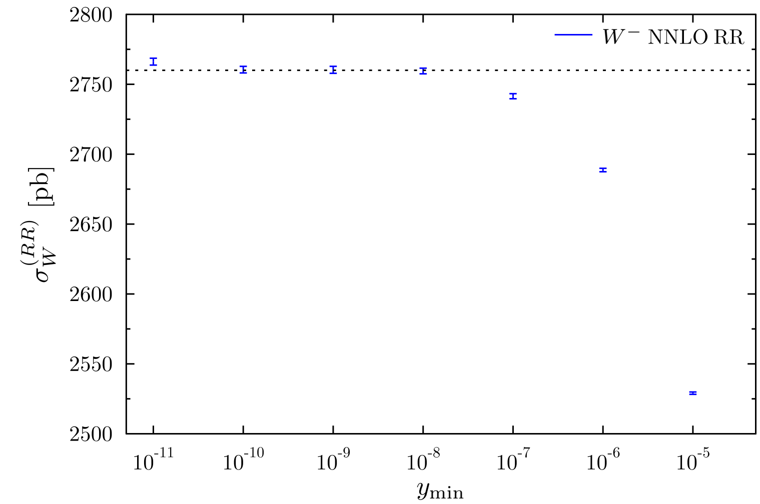

Figure 8.15: Integral of the regularized double real contribution for W^- production subprocess with different values of phase space cut y_{min}. [86]

non-integrable singularities of the $n+2$ parton contribution of the NNLO correction. The next step is computing the integrated counterterms which is a long and tedious procedure. The calculation of such integrals is an ongoing effort which requires the use of an extensive machinery.

I will illustrate the procedure on the example of the initial-final single collinear subtraction which is a part of $\int_1 \mathrm{d}\sigma_{n+2}^{RR,A_1}$. We need to evaluate the integral of Eq. (8.21) over the $n+1$ particle phase space,

$$\int \mathrm{d}\Phi_{n+2}(\{p\}_{n+2}; p_a + p_b)\, \mathcal{C}_{ar}^{(0),IF}(\{p\}_{n+2}). \tag{8.30}$$

In order to perform the integration of the counterterm, first we must factorize the original phase space measure into a convolution of the measures of phase spaces of resolved and unresolved particles. The $n+2$-particle phase space measure can be rewritten as

$$\mathrm{d}\Phi_{n+2}(\{p\}_{n+2}; p_a + p_b) = \int_{\xi_{min}}^{1} \mathrm{d}\xi\; \mathrm{d}\Phi_{n+1}(\{\hat{p}\}_{n+1}; \xi p_a + p_b) \frac{s}{2\pi} \mathrm{d}\Phi_2(Q, p_r; p_a + p_b), \tag{8.31}$$

where $s = (p_a + p_b)^2$. The lower limit of the integration is determined by the m_i masses of non-QCD particles in the final state (since gluons are massless and quark masses are omitted in this framework), such that

$$\xi_{min} = \frac{1}{s}\left(\sum_i m_i\right)^2 . \tag{8.32}$$

The two-particle phase space measure $\mathrm{d}\Phi_2(Q, p_r; p_a + p_b)$ depends on the convolution parameter ξ through the momentum Q which has a mass of $\sqrt{\xi s}$. Furthermore, this measure constrains the sum of the final-state momenta Q and p_r to be $p_r + Q = p_a + p_b$.

Using the phase space factorization, the integral we need to evaluate takes the form of

$$\begin{aligned}
\int \mathrm{d}\Phi_{n+2}(\{p\}_{n+2}; p_a + p_b)\mathcal{C}^{(0),IF}_{ar}(\{p\}_{n+2}) &= 8\pi\alpha_S \mu_R^{2\epsilon} \\
\times \frac{s}{2\pi}\left[\int \mathrm{d}\Phi_2(Q, p_r; p_a + p_b)\frac{1}{\xi}\frac{1}{s_{ar}}\hat{P}^{(0)}_{f_{ar}\,f_r}(\xi, k_{\perp,r})\right] \\
\otimes \int_{\xi_{min}}^1 \mathrm{d}\xi \left[\int \mathrm{d}\Phi_{n+1}(\{\hat{p}\}_{n+1}; \xi p_a + p_b)|\mathcal{M}^{(0)}_{n+1}(\{\hat{p}\}_{n+1})|^2\right],
\end{aligned} \tag{8.33}$$

where $\hat{P}^{(0)}_{f_{ar}\,f_r}(x, k_\perp)$ is an initial-state Altarelli-Parisi splitting function and the operation $\otimes$ denotes $\hat{P} \otimes |\mathcal{M}|^2 = \langle\mathcal{M}|\hat{P}|\mathcal{M}\rangle$. Since azimuthal correlations vanish when integrating the splitting function over the phase space of unresolved particles, we can simply use spin-averaged functions [17, 22]. Hence, the initial problem is reduced to the integration of spin-averaged kernel functions over the phase space of unresolved particles. These kernels are generally expressed as functions of the Lorentz-invariant quantities s_{ij}. In this example they depend only on $x_{a,r}$ which in our parametrization coincides with the convolution parameter ξ. The explicit forms of the spin-averaged initial-state splitting functions are

$$\begin{aligned}
P^{(0)}_{q\,g}(x;\epsilon) &= C_F\left[\frac{1+x^2}{1-x} - \epsilon(1-x)\right], \\
P^{(0)}_{g\,q}(x;\epsilon) &= T_R\left[x + 2\frac{1-x}{(1-\epsilon)x}\right], \\
P^{(0)}_{q\,\bar{q}}(x;\epsilon) &= C_F\left[1 - \epsilon - 2x(1-x)\right], \\
P^{(0)}_{g\,g}(x;\epsilon) &= 2C_A\left[x(1-x) + \frac{x}{1-x} + \frac{1-x}{x}\right].
\end{aligned} \tag{8.34}$$

The integrals of the splitting functions over the phase space of unresolved particles yield

$$-\frac{1}{\epsilon}\frac{\Gamma^2(1-\epsilon)}{\Gamma(1-2\epsilon)}(1-\xi)^{-2\epsilon}P^{(0)}_{f_{ar}\,,f_r}(\xi;\epsilon)\boldsymbol{T}^2_{ar}, \tag{8.35}$$

where $\boldsymbol{T}_{ar}^2$ denotes a color factor which is

$$\boldsymbol{T}_{q\,g}^2 = \boldsymbol{T}_{q\,\bar{q}}^2 = C_F, \qquad \boldsymbol{T}_{g\,q}^2 = T_R, \qquad \boldsymbol{T}_{g\,g}^2 = C_A. \tag{8.36}$$

The result obtained in this example is deceptively simple. In general, integrating the spin-averaged kernel functions is cumbersome and requires the use of advanced methods, like reverse unitarity [87], integration-by-parts reduction [88, 89], solution by differential equations [90, 91] with transformation to canonical basis [92] and the use of generalized polylogarithms [93–95]. This procedure is, however, outside the scope of this dissertation.

Part IV

Summary

Chapter 9

Discussion of results

Precise theoretical predictions for energetic particle collisions provide an essential tool for testing the limits of the currently prevalent model of particle physics, the so-called standard model. The main focus of this dissertation lies on quantum chromodynamics that describes the interaction between quarks and gluons. Since experiments at the LHC always involve colored particles in the initial state of collisions and the strength of the strong interaction at relevant energy scales is ten times greater than that of the electromagnetic interaction, QCD processes give a significant contribution to every event, making the calculation of precise QCD predictions mandatory.

The work that serves as the foundation of this dissertation was centered around the computation of QCD cross sections at next-to-next-to-leading order accuracy in perturbation theory, with the main goal of developing a general and mathematically well-defined method, called the CoLoRFulNNLO subtraction scheme, that enables such calculations. The subtraction scheme was initially completed for processes that involve colored partons only in the final state to which I contributed in a number of ways. I partook in the numerical integration of the counterterms and I have also implemented the two-loop contribution to three-jet production in electron-positron annihilation. Based on this work we were able to compute physical observables in electron-positron annihilation at NNLO accuracy. This, along with the necessary theoretical background is described in the first part.

In the second part of the dissertation, titled Measurement of the strong coupling, I have presented our analyses of two observables in electron-positron annihilation which allowed a precise determination of $\alpha_S(M_Z)$. As discussed in Chapter 5, we used the CoLoRFulNNLO method to obtain the energy-energy correlation between final-state partons of three-jet production in electron-positron annihilation at NNLO accuracy. This fixed-order prediction, however, has a limited range of validity and breaks down at angles near $0°$ and $180°$ due to large logarithmic contributions of infrared origin. I have implemented the resummation of these large logarithms at NNLL accuracy in the region around 180° and the matching of fixed-order and resummed results in a C++ code, thus producing the most accurate theoretical description of this observable to date. Using this NNLO+NNLL matched perturbative result, I performed fits to OPAL and SLD data with $\alpha_S(M_Z)$ as a fit parameter and showed that the impact of including NNLO fixed-order corrections is not negligible and it is necessary in a highly precise extraction of the coupling. I have also implemented the Dokshitzer-Marchesini-Weber analytic hadronization model and found that it cannot fully describe non-perturbative effects. However, the achieved small uncertainty of obtained results was promising [50].

We continued to work on this project with the goal of extracting the precise value of $\alpha_S(M_Z)$ from measurement data obtained by multiple experimental collaborations. Instead of the analytic hadronization model we have used modern Monte Carlo event generators for computing non-perturbative corrections and for the χ^2 analysis we upgraded my original C++ code. The obtained value of $\alpha_S(M_Z)$ was in agreement with the world average with a quality that is competitive with other state-of-the-art determinations of the coupling from electron-positron collisions [71]. Later we used our C++ framework in a wider collaboration aimed at extracting the strong coupling from jet rates with similarly good results [85]. The details of these works are presented in Chapters 6 and 7. Our results have been included in the updated $\alpha_S(M_Z)$ world average at the end of 2019, see entries "Verbytskyi (2j)" and "Kardos (EEC)" on Fig. 2.2. It is apparent that the obtained values are highly accurate in the category of measurements based on electron-positron annihilation. Since our results are the only new entries in this category, we can assess their effect by comparing the average $\alpha_S(M_Z)$ for this class of measurements. In 2017 it was 0.1169 ± 0.0034 [58] and with the 2019 update it became 0.1171 ± 0.0031 [1, 2].

Aside from extracting the value of $\alpha_S(M_Z)$ from observables, I have also worked on developing the CoLoRFulNNLO scheme. In the third part of this dissertation, titled Subtractions with hadronic initial states, I have presented work done towards extending this subtraction scheme to take initial state radiation into account. We have constructed all the necessary counterterms with a consistent parametrization and performed a number of checks to verify that the regularized double real contribution of the cross section is finite [86]. The analytic integration of counterterms is an ongoing effort which I have briefly illustrated at the end of the third part of this dissertation. Once this is done we will be able to produce highly accurate theoretical predictions for LHC observables.

Chapter 10

Magyar nyelvű összefoglaló

A nagyenergiás részecskeütközések pontos elméleti leírása lényeges eszköze a részecskefizikában jelenleg uralkodó elmélet, az úgynevezett standard modell ellenőrzésének. E disszertáció elsősorban a kvantum színdinamikára fókuszál, ami a kvarkok és gluonok közti kölcsönhatást írja le. Tekintve, hogy az LHC-nál folytatott kísérletek során megvalósuló részecskeütközések mindig tartalmaznak színes részecskéket a kezdeti állapotukban, továbbá az erős kölcsönhatás a releváns energiaskálákon tízszer erősebb az elektromágneses kölcsönhatásnál, a QCD folyamatok jelentős járulékot adnak minden eseményhez, ami a pontos QCD jóslatok számolását feltétlenül szükségessé teszi.

A disszertáció alapjául szolgáló munka a QCD hatáskeresztmetszeteknek a perturbációszámításban NNLO pontosságú számolására épül. Elsődleges célunk egy általános és matematikailag jól definiált, CoLoRFulNNLO levonási sémának nevezett módszer fejesztése, amely lehetővé teszi az említett számolásokat. Ez a séma kezdetben csak olyan folyamatokra lett kidolgozva, amelyek kizárólag a végállapotukban tartalmaznak színes partonokat. Ehhez a munkához több módon is hozzájárultam. Részt vettem az ellentagok numerikus integrálásában, valamint beprogramoztam az elektron-pozitron ütközésben történő három-jet keltés kéthurok járulékát. Erre a munkára építve elektron-pozitron ütközésben mérhető mennyiségeket NNLO pontossággal tudtunk meghatározni. Az erre vonatkozó eredményeket a szükséges elméleti háttérrel együtt az első részben tárgyaltam.

A disszertáció második, Az erős csatolás mérése című részében bemutattam két, elektron-pozitron ütközésben mérhető mennyiség vizsgálatát, amelyekkel meg tudtuk határozni az $\alpha_S(M_Z)$ pontos értékét. A CoLoRFulNNLO sémát, az 5. fejezetben leírtak szerint, a végállapoti partonok közötti energia-energia korreláció NNLO pontosságú meghatározására alkalmaztuk elektron-pozitron ütközésben történő három hadronzápor keletkezésének esetére. Ez a rögzített rendű jóslat érvényességi tartománya azonban korlátozott, hiszen 0° és 180° környezetében nagy, infravörös eredetű logaritmikus járulékok miatt elromlik. E nagy logaritmusok 180° közelében érvényes NNLL pontosságú felösszegzését, valamint a rögzített rendű és felösszegzett eredmények kombinálását beépítettem `C++` alapú programkódomba, ezzel megadva az eddigi legpontosabb elméleti jóslatot az említett mennyiségre. Az így kapott NNLO+NNLL pontosságú perturbatív eredménnyel függvényillesztést hajtottam végre OPAL és SLD adatokon, $\alpha_S(M_Z)$-t illesztési paraméterként használva. Megmutattam, hogy a rögzített rendű NNLO járulék hatása nem elhanyagolható, sőt, figyelembe vétele szükségszerű a csatolás rendkívül pontos meghatározásához. Ezen kívül beprogramoztam a Dokshitzer-Marchesini-Weber analitikus hadronizációs modellt és azt találtam, hogy a modell képtelen a nemperturbatív hatások teljes körű leírására, azonban a kapott eredmények kis bizonytalansága biztatónak bizonyult [50].

A továbbiakban folytattuk a munkát ezen a projekten azzal a céllal, hogy kinyerjük az $\alpha_S(M_Z)$ pontos értékét több kísérleti együttműködés által mért adatsorból. Az analitikus hadronizácós modell helyett modern Monte-Carlo eseménygenerátorokat használtunk a nemperturbatív korrekciók kiszámolására, valamint a χ^2 analízis elvégzéséhez továbbfejlesztettük a korábban használt `C++` kódomat. Az $\alpha_S(M_Z)$-re kapott eredmény jó egyezést mutatott a világátlaggal és minőségét tekintve versenyképesnek bizonyult a csatolás más, korszerű, elektron-pozitron ütközésre épülő meghatározásával [71]. Később a `C++` alapú keretrendszerünket egy szélesebb együttműködésben használtuk fel az erős csatolás jet rátákra épülő, hasonlóan jó eredményeket produkáló meghatározásához [85]. E munkák részleteit a 6. és 7. fejezetben mutattam be. Eredményeink 2019 végén bekerültek az új $\alpha_S(M_Z)$ világátlagba, lásd a "Verbytskyi (2j)" és "Kardos (EEC)" bejegyzéseket a 2.2. ábrán. Látható, hogy a kapott értékek rendkvül pontosak az elektron-pozitron ütközésre épülő mérések kategóriájában. Tekintve, hogy a mi eredményeink az egyedüli új bejegyzések ebben a csoportban, hatásukat az e mérésekre meghatározott átlagos $\alpha_S(M_Z)$-vel mérhetjük fel. 2017-ben ez az átlag 0.1169 ± 0.0034 [58] volt és a 2019-es aktualizálással 0.1171 ± 0.0031 [1,2] lett.

Az $\alpha_S(M_Z)$ mérhető mennyiségekből történő kinyerése mellett a CoLoRFulNNLO séma fejlesztésével foglalkoztam. A disszertáció harmadik, Levonások hadronos kezdeti állapotokkal című részében bemutattam a levonási séma kiterjesztése érdekében, a kezdeti állapoti sugárzás figyelembevételének céljával végzett munkát. Következetes paraméterezést alkalmazva felépítettünk minden szükséges ellentagot és számos ellenőrzést elvégezve igazoltuk, hogy a hatáskeresztmetszet regularizált, duplán valós járuléka véges [86]. Az ellentagok analitikus integrálása egy folyamatban lévő munka, amelyet röviden illusztráltam a disszertácó harmadik része végén. Amint ez a munka elkészül, képesek leszünk felettébb pontos elméleti jóslatokat produkálni az LHC-nál mérhető mennyiségekre.

Appendix A

The $\bar{\mathcal{A}}_{\text{res.}}$, $\bar{\mathcal{B}}_{\text{res.}}$ and $\bar{\mathcal{C}}_{\text{res.}}$ coefficients

The coefficients $\bar{\mathcal{A}}_{\text{res.}}$, $\bar{\mathcal{B}}_{\text{res.}}$ and $\bar{\mathcal{C}}_{\text{res.}}$ that are required in the log-R matching scheme are defined by Eq. (5.38) and they read (recall $y = \cos^2 \frac{\chi}{2}$)

$$\bar{\mathcal{A}}_{\text{res.}}(\chi,\mu) = \frac{1}{4}\Big\{ - A^{(1)} \ln^2(y) + 2(B^{(1)} + A^{(1)}y)\ln(y) - 2(A^{(1)} + B^{(1)})y \Big\}, \tag{A.1}$$

$$\begin{aligned}
\bar{\mathcal{B}}_{\text{res.}}(\chi,\mu) = \frac{1}{16}\Big\{ & \frac{(A^{(1)})^2}{2}\ln^4(y) + \Big[\frac{4A^{(1)}\beta_0}{3} - 2A^{(1)}B^{(1)} - 2(A^{(1)})^2 y\Big]\ln^3(y) \\
& + \Big[- 2A^{(2)} - 2\beta_0 B^{(1)} + 2(B^{(1)})^2 + \Big(6(A^{(1)})^2 - 4A^{(1)}\beta_0 + 6A^{(1)}B^{(1)}\Big)y \\
& - 2A^{(1)}\beta_0 \ln\xi_R^2\Big]\ln^2(y) + \Big[4B^{(2)} + 8(A^{(1)})^2\zeta_3 + 4\beta_0 B^{(1)}\ln\xi_R^2 \\
& + y\Big(- 12(A^{(1)})^2 + 4A^{(2)} + 8A^{(1)}\beta_0 - 12A^{(1)}B^{(1)} + 4\beta_0 B^{(1)} \\
& - 4(B^{(1)})^2 + 4A^{(1)}\beta_0\ln\xi_R^2\Big)\Big]\ln(y) + \Big[\frac{16A^{(1)}\beta_0\zeta_3}{3} - 8A^{(1)}B^{(1)}\zeta_3 \\
& + y\Big(12(A^{(1)})^2 - 4A^{(2)} - 8A^{(1)}\beta_0 + 12A^{(1)}B^{(1)} - 4\beta_0 B^{(1)} + 4(B^{(1)})^2 \\
& - 4B^{(2)} - 8(A^{(1)})^2\zeta_3 + (-4A^{(1)}\beta_0 - 4\beta_0 B^{(1)})\ln\xi_R^2\Big)\Big]\Big\},
\end{aligned} \tag{A.2}$$

$$\begin{aligned}
\bar{\mathcal{C}}_{\text{res.}}(\chi,\mu) = \frac{1}{64}\Big\{ & - \frac{(A^{(1)})^3}{6}\ln^6(y) + \Big[- \frac{4(A^{(1)})^2\beta_0}{3} + (A^{(1)})^2 B^{(1)} \\
& + (A^{(1)})^3 y\Big]\ln^5(y) + \Big[2A^{(1)}A^{(2)} - 2A^{(1)}\beta_0^2 + \frac{14A^{(1)}\beta_0 B^{(1)}}{3} \\
& - 2A^{(1)}(B^{(1)})^2 + \Big(- 5(A^{(1)})^3 + \frac{20(A^{(1)})^2\beta_0}{3} - 5(A^{(1)})^2 B^{(1)}\Big)y
\end{aligned} \tag{A.3}$$

$$
\begin{aligned}
&+ 2(A^{(1)})^2\beta_0 \ln\xi_R^2\Big] \ln^4(y) + \Big[\frac{16A^{(2)}\beta_0}{3} + \frac{8A^{(1)}\beta_1}{3} - 4A^{(2)}B^{(1)} \\
&+ \frac{8\beta_0^2 B^{(1)}}{3} - 4\beta_0(B^{(1)})^2 + \frac{4(B^{(1)})^3}{3} - 4A^{(1)}B^{(2)} - \frac{40(A^{(1)})^3\zeta_3}{3} \\
&+ \Big(\frac{16A^{(1)}\beta_0^2}{3} - 8A^{(1)}\beta_0 B^{(1)}\Big)\ln\xi_R^2 + y\Big(20(A^{(1)})^3 - 8A^{(1)}A^{(2)} \\
&- \frac{80(A^{(1)})^2\beta_0}{3} + 8A^{(1)}\beta_0^2 + 20(A^{(1)})^2B^{(1)} - \frac{56A^{(1)}\beta_0 B^{(1)}}{3} \\
&+ 8A^{(1)}(B^{(1)})^2 - 8(A^{(1)})^2\beta_0\ln\xi_R^2\Big)\Big] \ln^3(y) + \Big[- 4A^{(3)} - 4\beta_1 B^{(1)} - 8\beta_0 B^{(2)} \\
&+ 8B^{(1)}B^{(2)} - \frac{160}{3}(A^{(1)})^2\beta_0\zeta_3 + 40(A^{(1)})^2B^{(1)}\zeta_3 + \Big(- 8A^{(2)}\beta_0 - 4A^{(1)}\beta_1 \\
&- 8\beta_0^2B^{(1)} + 8\beta_0(B^{(1)})^2\Big)\ln\xi_R^2 - 4A^{(1)}\beta_0^2\ln^2\xi_R^2 + y\Big(- 60(A^{(1)})^3 \\
&+ 24A^{(1)}A^{(2)} + 80(A^{(1)})^2\beta_0 - 16A^{(2)}\beta_0 - 24A^{(1)}\beta_0^2 - 8A^{(1)}\beta_1 - 60(A^{(1)})^2B^{(1)} \\
&+ 12A^{(2)}B^{(1)} + 56A^{(1)}\beta_0B^{(1)} - 8\beta_0^2B^{(1)} - 24A^{(1)}(B^{(1)})^2 + 12\beta_0(B^{(1)})^2 \\
&- 4(B^{(1)})^3 + 12A^{(1)}B^{(2)} + 40(A^{(1)})^3\zeta_3 + \Big(24(A^{(1)})^2\beta_0 - 16A^{(1)}\beta_0^2 \\
&+ 24A^{(1)}\beta_0B^{(1)}\Big)\ln\xi_R^2\Big)\Big] \ln^2(y) + \Big[32A^{(1)}A^{(2)}\zeta_3 - 32A^{(1)}\beta_0^2\zeta_3 \\
&+ \frac{224}{3}A^{(1)}\beta_0B^{(1)}\zeta_3 - 32A^{(1)}(B^{(1)})^2\zeta_3 - 48(A^{(1)})^3\zeta_5 + 32(A^{(1)})^2\beta_0\zeta_3\ln\xi_R^2 \\
&+ y\Big(120(A^{(1)})^3 - 48A^{(1)}A^{(2)} + 8A^{(3)} - 160(A^{(1)})^2\beta_0 + 32A^{(2)}\beta_0 \\
&+ 48A^{(1)}\beta_0^2 + 16A^{(1)}\beta_1 + 120(A^{(1)})^2B^{(1)} - 24A^{(2)}B^{(1)} - 112A^{(1)}\beta_0B^{(1)} \\
&+ 16\beta_0^2B^{(1)} + 8\beta_1B^{(1)} + 48A^{(1)}(B^{(1)})^2 - 24\beta_0(B^{(1)})^2 + 8(B^{(1)})^3 \\
&- 24A^{(1)}B^{(2)} + 16\beta_0B^{(2)} - 16B^{(1)}B^{(2)} - 80(A^{(1)})^3\zeta_3 + \frac{320}{3}(A^{(1)})^2\beta_0\zeta_3 \\
&- 80(A^{(1)})^2B^{(1)}\zeta_3 + \Big(- 48(A^{(1)})^2\beta_0 + 16A^{(2)}\beta_0 + 32A^{(1)}\beta_0^2 + 8A^{(1)}\beta_1 \\
&- 48A^{(1)}\beta_0B^{(1)} + 16\beta_0^2B^{(1)} - 16\beta_0(B^{(1)})^2\Big)\ln\xi_R^2 + 8A^{(1)}\beta_0^2\ln^2\xi_R^2\Big)\Big] \ln(y) \\
&+ \Big[\frac{64A^{(2)}\beta_0\zeta_3}{3} + \frac{32A^{(1)}\beta_1\zeta_3}{3} - 16A^{(2)}B^{(1)}\zeta_3 + \frac{32}{3}\beta_0^2B^{(1)}\zeta_3 - 16\beta_0(B^{(1)})^2\zeta_3 \\
&+ \frac{16(B^{(1)})^3\zeta_3}{3} - 16A^{(1)}B^{(2)}\zeta_3 - \frac{80(A^{(1)})^3\zeta_3^2}{3} - 64(A^{(1)})^2\beta_0\zeta_5 + 48(A^{(1)})^2B^{(1)}\zeta_5 \\
&+ \Big(\frac{64}{3}A^{(1)}\beta_0^2\zeta_3 - 32A^{(1)}\beta_0B^{(1)}\zeta_3\Big)\ln\xi_R^2 + y\Big(- 120(A^{(1)})^3 + 48A^{(1)}A^{(2)} - 8A^{(3)}
\end{aligned}
$$

$$
\begin{aligned}
&+160(A^{(1)})^2\beta_0-32A^{(2)}\beta_0-48A^{(1)}\beta_0^2-16A^{(1)}\beta_1-120(A^{(1)})^2B^{(1)}\\
&+24A^{(2)}B^{(1)}+112A^{(1)}\beta_0B^{(1)}-16\beta_0^2B^{(1)}-8\beta_1B^{(1)}-48A^{(1)}(B^{(1)})^2\\
&+24\beta_0(B^{(1)})^2-8(B^{(1)})^3+24A^{(1)}B^{(2)}-16\beta_0B^{(2)}+16B^{(1)}B^{(2)}\\
&+80(A^{(1)})^3\zeta_3-32A^{(1)}A^{(2)}\zeta_3-\frac{320}{3}(A^{(1)})^2\beta_0\zeta_3+32A^{(1)}\beta_0^2\zeta_3\\
&+80(A^{(1)})^2B^{(1)}\zeta_3-\frac{224}{3}A^{(1)}\beta_0B^{(1)}\zeta_3+32A^{(1)}(B^{(1)})^2\zeta_3+48(A^{(1)})^3\zeta_5\\
&+\Bigg(48(A^{(1)})^2\beta_0-16A^{(2)}\beta_0-32A^{(1)}\beta_0^2-8A^{(1)}\beta_1+48A^{(1)}\beta_0B^{(1)}\\
&-16\beta_0^2B^{(1)}+16\beta_0(B^{(1)})^2-32(A^{(1)})^2\beta_0\zeta_3\Bigg)\ln\xi_R^2-8A^{(1)}\beta_0^2\ln^2\xi_R^2\Bigg)\Bigg]\Bigg\}\,.
\end{aligned}
$$

Appendix B

Hadronization corrections to jet rates

Fig. B.1 shows the $\delta\xi_1$ and $\delta\xi_2$ distributions which were used to produce hadronization corrections for jet rates according to Eqs. (7.8) and (7.10). The size of hadronization corrections are shown in Fig. 7.3.

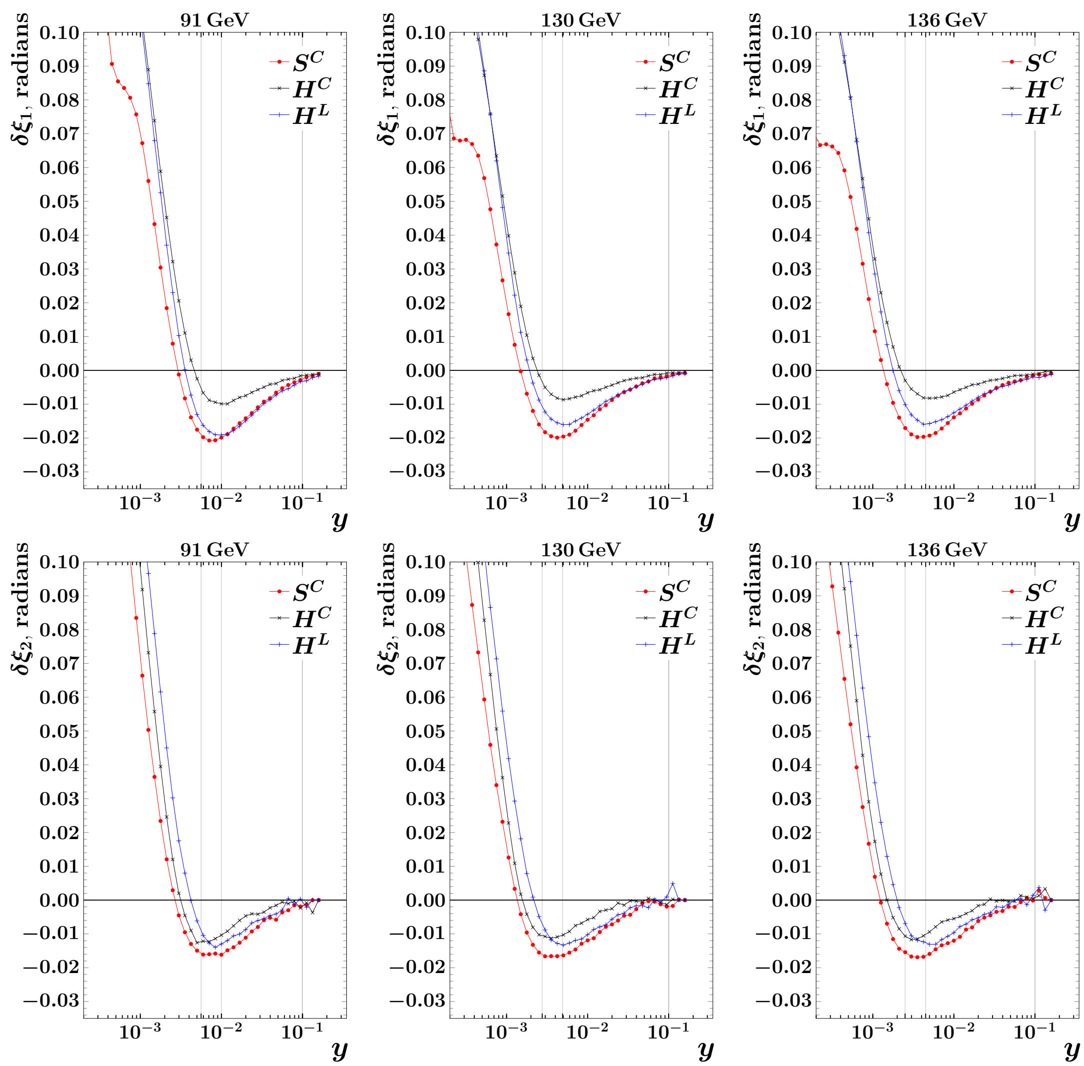

Figure B.1: Hadronization corrections $\delta\xi_1$ and $\delta\xi_2$ obtained with different Monte Carlo event simulations. The used fit range is indicated with vertical lines.

Bibliography

[1] M. Tanabashi et al., “Review of Particle Physics and 2019 update,” *Phys. Rev.*, vol. D98, no. 3, p. 030001, 2018.

[2] P.A. Zyla et al., “Review of Particle Physics,” *Prog. Theor. Exp. Phys.*, vol. 2020, p. 083C01, 2020.

[3] D. J. Gross and F. Wilczek, “Ultraviolet behavior of non-abelian gauge theories,” *Phys. Rev. Lett.*, vol. 30, pp. 1343–1346, Jun 1973.

[4] H. D. Politzer, “Reliable perturbative results for strong interactions?,” *Phys. Rev. Lett.*, vol. 30, pp. 1346–1349, Jun 1973.

[5] H. Fritzsch, M. Gell-Mann, and H. Leutwyler, “Advantages of the color octet gluon picture,” *Physics Letters B*, vol. 47, no. 4, pp. 365 – 368, 1973.

[6] S. Bethke, “α_s 2016,” *Nucl. Part. Phys. Proc.*, vol. 282-284, pp. 149–152, 2017.

[7] E. C. Poggio, H. R. Quinn, and S. Weinberg, “Smearing method in the quark model,” *Phys. Rev. D*, vol. 13, pp. 1958–1968, Apr 1976.

[8] J. C. Collins, D. E. Soper, and G. F. Sterman, *Factorization of Hard Processes in QCD*, vol. 5, pp. 1–91. 1989.

[9] S. Catani, “The Singular behavior of QCD amplitudes at two loop order,” *Phys. Lett.*, vol. B427, pp. 161–171, 1998.

[10] T. Kinoshita, “Mass singularities of feynman amplitudes,” *Journal of Mathematical Physics*, vol. 3, no. 4, pp. 650–677, 1962.

[11] T. D. Lee and M. Nauenberg, “Degenerate systems and mass singularities,” *Phys. Rev.*, vol. 133, pp. B1549–B1562, Mar 1964.

[12] G. Somogyi, Z. Trocsanyi, and V. Del Duca, “A Subtraction scheme for computing QCD jet cross sections at NNLO: Regularization of doubly-real emissions,” *JHEP*, vol. 01, p. 070, 2007.

[13] G. Somogyi and Z. Trocsanyi, “A Subtraction scheme for computing QCD jet cross sections at NNLO: Regularization of real-virtual emission,” *JHEP*, vol. 01, p. 052, 2007.

[14] V. Del Duca, C. Duhr, A. Kardos, G. Somogyi, Z. Szor, Z. Trocsanyi, and Z. Tulipant, “Jet production in the CoLoRFulNNLO method: event shapes in electron-positron collisions,” *Phys. Rev.*, vol. D94, no. 7, p. 074019, 2016.

[15] V. Del Duca, C. Duhr, G. Somogyi, F. Tramontano, and Z. Trocsanyi, “Higgs boson decay into b-quarks at NNLO accuracy,” *JHEP*, vol. 04, p. 036, 2015.

[16] V. Del Duca, C. Duhr, A. Kardos, G. Somogyi, and Z. Trocsanyi, “Three-jet production in electron-positron collisions at next-to-next-to-leading order accuracy,” *Phys. Rev. Lett.*, vol. 117, no. 15, p. 152004, 2016.

[17] S. Catani and M. H. Seymour, “A General algorithm for calculating jet cross-sections in NLO QCD,” *Nucl. Phys.*, vol. B485, pp. 291–419, 1997. [Erratum: Nucl. Phys.B510,503(1998)].

[18] S. Frixione, Z. Kunszt, and A. Signer, “Three jet cross-sections to next-to-leading order,” *Nucl. Phys.*, vol. B467, pp. 399–442, 1996.

[19] S. Frixione, “A General approach to jet cross-sections in QCD,” *Nucl. Phys.*, vol. B507, pp. 295–314, 1997.

[20] L. W. Garland, T. Gehrmann, E. W. N. Glover, A. Koukoutsakis, and E. Remiddi, “The Two loop QCD matrix element for $e^+e^- \to 3$ jets,” *Nucl. Phys.*, vol. B627, pp. 107–188, 2002.

[21] L. W. Garland, T. Gehrmann, E. W. N. Glover, A. Koukoutsakis, and E. Remiddi, “Two loop QCD helicity amplitudes for $e^+e^- \to$ three jets,” *Nucl. Phys.*, vol. B642, pp. 227–262, 2002.

[22] S. Weinzierl, “Event shapes and jet rates in electron-positron annihilation at NNLO,” *JHEP*, vol. 06, p. 041, 2009.

[23] A. Gehrmann-De Ridder, T. Gehrmann, E. W. N. Glover, and G. Heinrich, “EERAD3: Event shapes and jet rates in electron-positron annihilation at order α_s^3,” *Comput. Phys. Commun.*, vol. 185, p. 3331, 2014.

[24] S. Kluth, “Tests of quantum chromo dynamics at e^+e^- colliders,” *Rept. Prog. Phys.*, vol. 69, pp. 1771–1846, 2006.

[25] G. Dissertori, “The Determination of the strong coupling constant,” *Adv. Ser. Direct. High Energy Phys.*, vol. 26, pp. 113–128, 2016.

[26] A. Gehrmann-De Ridder et al., "NNLO corrections to event shapes in e^+e^- annihilation," *JHEP*, vol. 12, p. 094, 2007.

[27] S. Weinzierl, "Next-to-next-to-leading order corrections to three-jet observables in electron-positron annihilation," *Phys. Rev. Lett.*, vol. 101, p. 162001, Oct 2008.

[28] A. Gehrmann-De Ridder, T. Gehrmann, E. W. N. Glover, and G. Heinrich, "Jet rates in electron-positron annihilation at $o(\alpha_s^3)$ in qcd," *Phys. Rev. Lett.*, vol. 100, p. 172001, Apr 2008.

[29] S. Gorishny, A. Kataev, and S. Larin, "The $\mathrm{O}(\alpha_S^3)$ corrections to $\sigma_{tot}(e^+e^- \to$ hadrons) and $\Gamma(\tau^- \to \nu\tau +$ hadrons) in QCD," *Physics Letters B*, vol. 259, no. 1, pp. 144 – 150, 1991.

[30] D. de Florian and M. Grazzini, "The back-to-back region in e^+e^- energy-energy correlation," *Nucl. Phys.*, vol. B704, pp. 387–403, 2005.

[31] T. Becher and M. Schwartz, "A precise determination of α_s from LEP thrust data using effective field theory," *JHEP*, vol. 07, p. 034, 2008.

[32] Yang-Ting Chien and M.D. Schwartz, "Resummation of heavy jet mass and comparison to LEP data," *JHEP*, vol. 1008, p. 058, 2010.

[33] P.F. Monni, T. Gehrmann and G. Luisoni, "Two-loop soft corrections and resummation of the thrust distribution in the dijet region," *JHEP*, vol. 08, p. 010, 2011.

[34] S. Alioli et al., "Combining higher-order resummation with multiple NLO calculations and parton showers in GENEVA," *JHEP*, vol. 09, p. 120, 2013.

[35] T. Becher and G. Bell, "NNLL Resummation for jet broadening," *JHEP*, vol. 1211, p. 126, 2012.

[36] A. Banfi et al., "A general method for the resummation of event-shape distributions in e^+e^- annihilation," *JHEP*, vol. 1505, p. 102, 2015.

[37] R. Abbate et al., "Thrust at N^3LL with power corrections and a precision global fit for $\alpha_S(M_Z)$," *Phys.Rev.*, vol. D83, p. 074021, 2011.

[38] A. Hoang et al., "C-parameter distribution at $\mathrm{N}^3\mathrm{LL}'$ including power corrections," *Phys. Rev.*, vol. D91, no. 9, p. 094017, 2015.

[39] S. Catani, L. Trentadue, G. Turnock, and B. R. Webber, "Resummation of large logarithms in e+ e- event shape distributions," *Nucl. Phys.*, vol. B407, pp. 3–42, 1993.

[40] T. Gehrmann, G. Luisoni and H. Stenzel, "Matching NLLA + NNLO for event shape distributions," *Phys. Lett.*, vol. B664, pp. 265–273, 2008.

[41] C. Basham et al., "Energy correlations in electron-positron annihilation: testing QCD," *Phys.Rev.Lett.*, vol. 41, p. 1585, 1978.

[42] P.D. Acton et al., "A determination of $\alpha_S(M_Z)$ at LEP using resummed QCD calculations," *Z. Phys.*, vol. C59, pp. 1–20, 1993.

[43] E. Laenen, G. F. Sterman, and W. Vogelsang, "Higher order QCD corrections in prompt photon production," *Phys. Rev. Lett.*, vol. 84, pp. 4296–4299, 2000.

[44] A. Kulesza, G. F. Sterman, and W. Vogelsang, "Joint resummation in electroweak boson production," *Phys. Rev.*, vol. D66, p. 014011, 2002.

[45] G. Bozzi, S. Catani, D. de Florian, and M. Grazzini, "The q(T) spectrum of the Higgs boson at the LHC in QCD perturbation theory," *Phys. Lett.*, vol. B564, pp. 65–72, 2003.

[46] T. Becher and M. Neubert, "Drell-Yan Production at Small q_T, Transverse Parton Distributions and the Collinear Anomaly," *Eur. Phys. J.*, vol. C71, p. 1665, 2011.

[47] R.W.L. Jones et al., "Theoretical uncertainties on α_S from event shape variables in e^+e^- annihilations," *JHEP*, vol. 12, p. 007, 2003.

[48] Y.L. Dokshitzer, G. Marchesini and B.R.Webber, "Nonperturbative effects in the energy energy correlation," *JHEP*, vol. 07, p. 012, 1999.

[49] W. Bizon, P. F. Monni, E. Re, L. Rottoli, and P. Torrielli, "Momentum-space resummation for transverse observables and the Higgs $p_\perp$ at N^3LL+NNLO," *JHEP*, vol. 02, p. 108, 2018.

[50] Z. Tulipant, A. Kardos, and G. Somogyi, "Energy–energy correlation in electron–positron annihilation at NNLL + NNLO accuracy," *Eur. Phys. J.*, vol. C77, no. 11, p. 749, 2017.

[51] F. James and M. Roos, "Minuit: A system for function minimization and analysis of the parameter errors and correlations," *Comput.Phys.Commun.*, vol. 10, pp. 343–367, 1975.

[52] F. James and M. Winkler, "MINUIT User's Guide," 2004.

[53] K. Abe et al., "Measurement of $\alpha_S(M(Z))$ from hadronic event observables at the Z^0 resonance," *Phys. Rev.*, vol. D51, pp. 962–984, 1995.

[54] J. C. Collins and D. E. Soper, “Back-To-Back Jets in QCD,” *Nucl. Phys.*, vol. B193, p. 381, 1981. [Erratum: Nucl. Phys.B213,545(1983)].

[55] J. C. Collins and D. E. Soper, “Back-To-Back Jets: Fourier Transform from B to K-Transverse,” *Nucl. Phys.*, vol. B197, pp. 446–476, 1982.

[56] J. C. Collins and D. E. Soper, “The Two Particle Inclusive Cross-section in e^+e^- Annihilation at PETRA, PEP and LEP Energies,” *Nucl. Phys.*, vol. B284, pp. 253–270, 1987.

[57] R. Fiore, A. Quartarolo, and L. Trentadue, “Energy-energy correlation for Theta $\to$ 180-degrees at LEP,” *Phys. Lett.*, vol. B294, pp. 431–435, 1992.

[58] C. Patrignani et al., “Review of Particle Physics,” *Chin. Phys.*, vol. C40, no. 10, p. 100001, 2016.

[59] O. Adrian et al., “Determination of α_S from hadronic event shapes measured on the Z^0 resonance,” *Phys. Lett.*, vol. B284, pp. 471–481, 1992.

[60] P. Abreu et al., “Determination of α_S in second order QCD from hadronic Z decays,” *Z. Phys.*, vol. C54, pp. 55–74, 1992.

[61] P.D. Acton et al., “An Improved measurement of $\alpha_S(M_Z)$ using energy correlations with the OPAL detector at LEP,” *Phys. Lett.*, vol. B276, pp. 547–564, 1992.

[62] W. Bartel et al., “Measurements of energy correlations in $e^+e^- \to hadrons$,” *Z. Phys.*, vol. C25, p. 231, 1984.

[63] E. Fernandez et al., “A measurement of energy-energy correlations in $e^+e^- \to$ Hadrons at $\sqrt{s} = 29\,\mathrm{GeV}$,” *Phys. Rev.*, vol. D31, p. 2724, 1985.

[64] D.R. Wood et al., “Determination of α_S from energy-energy correlations in e^+e^- annihilation at 29 GeV,” *Phys. Rev.*, vol. D37, p. 3091, 1988.

[65] W. Braunschweig et al., “A study of energy-energy correlations between 12 GeV and 46.8 GeV CM energies,” *Z. Phys.*, vol. C36, pp. 349–361, 1987.

[66] H.J. Behrend et al., “Analysis of the energy weighted angular correlations in hadronic e^+e^- annihilations at 22 GeV and 34 GeV,” *Z. Phys.*, vol. C14, p. 95, 1982.

[67] C. Berger et al., “A study of energy-energy correlations in e^+e^- annihilations at $\sqrt{s} = 34.6\,\mathrm{GeV}$,” *Z. Phys.*, vol. C28, p. 365, 1985.

[68] I. Adachi et al., “Measurements of α_S in e^+e^- annihilation at $\sqrt{s} = 53.3\,\mathrm{GeV}$ and 59.5 GeV,” *Phys. Lett.*, vol. B227, pp. 495–500, 1989.

[69] T. Gleisberg et al., "Event generation with SHERPA 1.1," *JHEP*, vol. 02, p. 007, 2009.

[70] J. Bellm et al., "Herwig 7.0/Herwig++ 3.0 release note," *Eur. Phys. J.*, vol. C76, no. 4, p. 196, 2016.

[71] A. Kardos, S. Kluth, G. Somogyi, Z. Tulipant, and A. Verbytskyi, "Precise determination of $\alpha_S(M_Z)$ from a global fit of energy–energy correlation to NNLO+NNLL predictions," *Eur. Phys. J.*, vol. C78, no. 6, p. 498, 2018.

[72] S. M. T. Sjostrand and P. Skands, "PYTHIA 6.4 physics and manual," *JHEP*, vol. 05, p. 026, 2006.

[73] F. K. J.C. Winter and G. Soff, "A modified cluster hadronization model," *Eur. Phys. J.*, vol. C36, pp. 381–395, 2004.

[74] P. Nason and C. Oleari, "Next-to-leading order corrections to momentum correlations in $Z^0 \to b\bar{b}$," *Phys. Lett.*, vol. B407, pp. 57–60, 1997.

[75] K. G. Chetyrkin, R. V. Harlander, and J. H. Kuhn, "Quartic mass corrections to R_{had} at $\mathcal{O}(\alpha_s^3)$," *Nucl. Phys.*, vol. B586, pp. 56–72, 2000. [Erratum: Nucl. Phys.B634,413(2002)].

[76] Y. L. Dokshitzer, G. Marchesini, and B. R. Webber, "Dispersive approach to power behaved contributions in QCD hard processes," *Nucl. Phys.*, vol. B469, pp. 93–142, 1996.

[77] S. Catani, Y. L. Dokshitzer, M. Olsson, G. Turnock, and B. R. Webber, "New clustering algorithm for multi - jet cross-sections in e+ e- annihilation," *Phys. Lett.*, vol. B269, pp. 432–438, 1991.

[78] A. Heister et al., "Studies of QCD at e^+e^- centre-of-mass energies between 91 GeV and 209 GeV," *Eur. Phys. J.*, vol. C35, pp. 457–486, 2004.

[79] A. Banfi et al., "The two-jet rate in e^+e^- at next-to-next-to-leading-logarithmic order," *Phys. Rev. Lett.*, vol. 117, no. 17, p. 172001, 2016.

[80] S. Catani et al., "Resummation of large logarithms in e^+e^- event shape distributions," *Nucl. Phys.*, vol. B407, pp. 3–42, 1993.

[81] A. Banfi, B.K. El-Menoufi and P.F. Monni, "The Sudakov radiator for jet observables and the soft physical coupling," 2018.

[82] P. Pfeifenschneider et al., "QCD analyses and determinations of α_S in e^+e^- annihilation at energies between 35 GeV and 189 GeV," *Eur. Phys. J.*, vol. C17, pp. 19–51, 2000.

[83] P. Achard et al., "Studies of hadronic event structure in e^+e^- annihilation from 30 GeV to 209 GeV with the L3 detector," *Phys. Rept.*, vol. 399, pp. 71–174, 2004.

[84] G. Dissertori et al., "First determination of the strong coupling constant using NNLO predictions for hadronic event shapes in e^+e^- annihilations," *JHEP*, vol. 02, p. 040, 2008.

[85] A. Verbytskyi, A. Banfi, A. Kardos, P. F. Monni, S. Kluth, G. Somogyi, Z. Szor, Z. Trocsanyi, Z. Tulipant, and G. Zanderighi, "High precision determination of α_s from a global fit of jet rates," *JHEP*, vol. 08, p. 129, 2019.

[86] A. Kardos, G. Bevilacqua, G. Somogyi, Z. Trocsanyi, and Z. Tulipant, "CoLoRFulNNLO for LHC processes," *PoS*, vol. LL2018, p. 074, 2018.

[87] C. Anastasiou and K. Melnikov, "Higgs boson production at hadron colliders in NNLO QCD," *Nucl. Phys.*, vol. B646, pp. 220–256, 2002.

[88] K. G. Chetyrkin and F. V. Tkachov, "Integration by Parts: The Algorithm to Calculate beta Functions in 4 Loops," *Nucl. Phys.*, vol. B192, pp. 159–204, 1981.

[89] S. Laporta, "High precision calculation of multiloop Feynman integrals by difference equations," *Int. J. Mod. Phys.*, vol. A15, pp. 5087–5159, 2000.

[90] E. Remiddi, "Differential equations for Feynman graph amplitudes," *Nuovo Cim.*, vol. A110, pp. 1435–1452, 1997.

[91] T. Gehrmann and E. Remiddi, "Differential equations for two loop four point functions," *Nucl. Phys.*, vol. B580, pp. 485–518, 2000.

[92] J. M. Henn, "Multiloop integrals in dimensional regularization made simple," *Phys. Rev. Lett.*, vol. 110, p. 251601, 2013.

[93] A. B. Goncharov, "Multiple polylogarithms, cyclotomy and modular complexes," *Math. Res. Lett.*, vol. 5, pp. 497–516, 1998.

[94] A. B. Goncharov, "Multiple polylogarithms and mixed Tate motives," 2001.

[95] C. Duhr, "Hopf algebras, coproducts and symbols: an application to Higgs boson amplitudes," *JHEP*, vol. 08, p. 043, 2012.